UCSF

Department of Radiology and Biomedical Imaging

SEVENTH ANNUAL IMAGING RESEARCH SYMPOSIUM

September 1, 2010

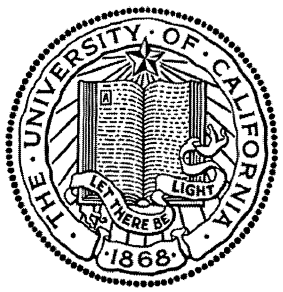

UCSF Department of Radiology and Biomedical Imaging

SEVENTH ANNUAL

IMAGING RESEARCH SYMPOSIUM

September 1, 2010

Organizers:
Galateia Kazakia, PhD; Esther Yuh, MD; Xiaojuan Li, PhD; David Saloner, PhD;
and Katie Murphy

Acknowledgements:
Valerie Cardenas-Nicholson, PhD; Belinda Chang, MD, PhD;
Brett Elicker, MD; Ella Jones, PhD; Tracy Luks, PhD; Z. Jane Wang, MD;
and Duan Xu, PhD

UCSF DEPARTMENT OF RADIOLOGY AND BIOMEDICAL IMAGING

7th Annual Radiology Imaging Research Symposium

http://www.radiology.ucsf.edu/research/imaging-research-symposium

September 1st, 2010

Research Interest and Special Resource Group Overview:
12:00 – 1:00pm, Nobel Wall, 513 Parnassus Ave

Speaker Presentations:
1:00 – 4:30pm, Cole Hall, 513 Parnassus Ave

Poster, Award and Reception:
4:30 – 6pm, Millberry Union, Golden Gate and City Lights rooms, 500 Parnassus Ave

12:00pm Research Interest and Special Resource Group Overview
Nobel Wall

12:30pm Registration
Cole Hall

1:00-1:05 Opening Remarks
Sharmila Majumdar, PhD, Professor and Vice Chair for Research, Department of Radiology and Biomedical Imaging

1:05-2:45 Oral Presentations (Session I)
Moderators: Galateia Kazakia, PhD and Esther Yuh, MD

1:05-1:15 Novel Antibody-Based Probes for the Detection and Study of Pre-Malignant Breast Cancer Cells
Drake CR, Miller D, Gascard P, Dumont N, Tlsty T, Jones EF

1:15-1:25 Bacteriophage-based nanoprobe targeting pancreatic cancer in transgenic mouse model
Feng J, Thomas SA, Allen E, Iyer AK, Jones EF, Hanahan D, Kelly K, He J, VanBrocklin HF

1:25-1:35 Assessing the Effects of Radiation Therapy on Normal Brain Tissue in Patients with Glioma using Susceptibility-Weighted Imaging at 7 Tesla
Lupo JM, Chuang C, Jimenez B, Chang SM, Barani IJ, Hess CP, Nelson SJ

1:35-1:45 Anatomic and Physiologic MR Imaging Characterizes Cellular and Genetic Expression Patterns of Angiogenesis in Glioblastoma Multiforme
Barajas R, Phillips J, Hodgson JG, Chang J, Vandenberg S, Parsa A, McDermott M, Berger M, Dillon W, Cha S

1:45-1:55 Multi-compound Hyperpolarization allows Simultaneous Assessment of Multiple Enzymatic Activities In Vivo
Wilson DM, Keshari KR, Larson PEZ, Chen AP, Hu S, Van Criekinge M, Bok R, Nelson SJ, Macdonald JM, Vigneron DB, Kurhanewicz J

1:55-2:05 Depth-of-interaction compensation using a focused-cut scintillator for a pinhole gamma camera
Alhassen F, Kudrolli H, Singh B, Kim S, Nagarkar V, Seo Y, Gould RG

2:05-2:15 A Rational Basis for Selection of Contrast Material Combinations for Dual Energy CT Imaging: Lessons from Three-Material Decomposition of Contrast Materials
Kumar R, Forsythe C, Yang ZA, Fu Y, Wang ZJ, Shepherd J, Jones EF, Yeh BM

2:15-2:25 A Trabecular Bone Analysis Framework for High-resolution MRI of the Proximal Femur
Folkesson J, Carballido-Gamio J, Karampinos DC, Baum T, Link TM, Majumdar S, Krug R

2:25-2:35 Knee cartilage T2 characteristics and evolution in relation to morphological abnormalities detected by 3T MRI: a longitudinal study of the normal control cohort from the Osteoarthritis Initiative
Pan J, Pialat JB, Joseph T, Link TM

2:35-3:00 Coffee Break

3:00-4:20 Oral Presentations (Session II)

Moderators: Galateia Kazakia, PhD and Esther Yuh, MD

3:00-3:10 Relationship Between Regional Brain Amyloid-β Deposition and Brain Atrophy Rates in Mild Cognitive Impairment
Tosun D, Schuff N, Jagust W, Weiner MW, Alzheimer's Disease NeuroImaging Initiative

3:10-3:20 Diagnostic Accuracy of Fetal MRI for Supratentorial Brain Abnormalities
Hashemi Z, Cuneo A, Barkovich J, Bartha A, Glenn O

3:20-3:30 HRMAS NMR Spectroscopy - An important tool in Understanding Joint Degradation in Osteo-Arthritis
Shet K, Siddiqui SM, Kurhanewicz J, Ries M, Yoshihara H, Li X

3:30-3:40 Detection of inflammatory arthritis using hyperpolarized [1-^{13}C]pyurvate with magnetic resonance imaging and spectroscopy
MacKenzie J, Yen YF, Mayer D, Tropp J, Hurd R, Spielman DM

3:40-3:50 Imaging metabolism of hyperpolarized [1-^{13}C]pyruvate using multi-band frequency encoding
von Morze C, Reed G, Bok R, Shin P, Larson PEZ, Hu S, Vigneron DB

3:50-4:00 Liver Fat and Water MR T2 Values at 3T and Dependence Upon Steatosis Level
Gilman A, Qayyum A, Nystrom M, Noworolski SM

4:00-4:10 Border Zone Delayed Contrast Enhancement in Hypertrophic Cardiomyopathy: Comparison to Occlusive Myocardial Infarctions
Naeger DM, Higgins C, De Marco T, Muzzarelli S, Ordovas K

4:10-4:20 Reducing Patient Radiation Exposure During CT-Guided Injections for Spinal Pain
Shepherd TM, Hess CP, Chin CT, Gould RG, Dillon WP

4:30-6:00 Poster Session, Award Presentations, and Catered Reception

4:45pm **Presentation of the Hasegawa Award**
Ronald L. Arenson, MD, Professor and Chair, Department of Radiology and Biomedical Imaging

5:45pm **Podium and Poster Presentation Awards and Closing Comments**
William P. Dillon, MD, Professor and Executive Vice Chair, Dept of Radiology and Biomedical Imaging

Research Interest Groups (RIGs) and Special Resource Groups (SRGs)

RIGs	Leadership
Brain Behavior	Srikantan Nagarajan, PhD Pratik Mukherjee, MD, PhD
Brain Cancer	Sarah J. Nelson, PhD Soonmee Cha, MD
Breast Cancer	Nola Hylton, PhD Bonnie N. Joe, MD, PhD
Musculoskeletal Quantitative Imaging	Sharmila Majumdar, PhD Thomas M. Link, MD
Neurodegenerative Diseases	Norbert Schuff, PhD Michael W. Weiner, MD
Neurovascular/Neurointerventional	David Saloner, PhD Steven Hetts, MD
Pediatrics/Fetal	A. James Berkovich, MD
Prostate Cancer	John Kurhanewicz, PhD Fergus V. Coakley, MD

SRGs	Leadership
Informatics and Image Processing/Display	David Avrin, MD, PhD
MRI/MRS	Dan Vigneron, PhD Michael F. Wendland, PhD
Nuclear-Optical Imaging	Carina Mari Aparici, MD Henry F. VanBrocklin, PhD

Poster Presentations

#	First Author	Abstract Title
1	Timothy Durazzo	N-Acetylaspartate Levels in the Brain Reward System Discriminate Smoking and Non-smoking Alcohol Dependent Individuals During Early Abstinence
2	Adam Elkhaled	Comparison of glioma sub-populations using in-vivo ADC values and ex-vivo 1H HR-MAS spectroscopy
3	Sara LaHue	Microstructural Correlations of White Matter Tracts in the Human Brain
4	Fan-pei Gloria Yang	Tract-Based Spatial Statistics Reveals Widespread Microstructural White Matter Disruption within Two Weeks of Mild Traumatic Brain Injury
5	Michael Ewers	Multivariate Patterns of Brain Perfusion and Deformation-Based Atrophic Changes in Normal Aging
6	Anderson Mon	Reduced glutamate in the anterior cingulate of recently de-toxified alcoholics: A magnetic resonance spectroscopy study
7	Linda Chao	Hippocampal atrophy in young veterans with PTSD and cognitive impairment: a potential link between PTSD and dementia
8	Ilwoo Park	Hyperpolarized 13C MR Spectroscopic Imaging for the Detection of Early Response to Treatment with Temozolomide in Brain Tumors
9	Llewellyn Jalbert	Metabolic Characterization of Recurrent Grade 2 Glioma using Proton HR-MAS Spectroscopy
10	Janine Lupo	Can Susceptibility-Weighted Imaging Determine Response to Combined Anti-Angiogenic, Cytotoxic, and Radiation Therapy in GBM Patients?
11	Laleh Jalilian	Assessment of Diffusion Parameters at Pre-, Mid- and Post-radiation in Glioblastoma Multiforme Patients receiving Bevacizumab therapy
12	Myriam Chaumeil	In vivo detection of PI3K pathway inhibition by hyperpolarized 13C MRSI at 14.1T in an orthotopic model of GBMS
13	Emma Essock-Burns	Comparison of DSC-derived Perfusion Parameters in Response to Conventional Therapy or Concurrent Anti-Angiogenic Therapy in Patients Newly Diagnosed with
14	Yan Li	Longitudinal MRSI study in newly diagnosed Glioblastoma Multiforme
15	Eugene Ozhinsky	Comparison of Automatic and Manual Prescription Protocols for Brain 3D MRSI
16	Vignesh Arasu	Can signal enhancement ratio (SER) reduce the number of recommended biopsies without affecting cancer yield in occult MRI-detected lesions?
17	Frederick Duewer	Compositional Signatures for 3-Component Mammography
18	Jason Bowen	SPECT Dual-Isotope Myocardial Perfusion Imaging with a 20-Pinhole Collimator: a Simulation Study
19	Sangtaek Kim	Phantom experiments on a PSAPD-based compact gamma camera with submillimeter spatial resolution for small animal SPECT
20	Joseph Blecha	Preparation of 12a-[18F]fluoromethyl-rotenone: A novel positron emitting cardiac blood flow tracer
21	Shorouk Danoon	Automated [18F]F2 gas production from [18F]fluoride ion
22	Mamak Eatesam	Comparison of breath-hold and free-breathing diffusion-weighted techniques for liver MR diffusivity in healthy volunteers and patients
23	Andrew Taylor	Imaging of Hepatic Steatosis and Hyperpolarized Carbon Metabolism at 14T: Applications to a Murine Model of Non-Alcoholic Fatty Liver Disease (NAFLD)
24	Yong Pang	7T human liver imaging using microstrip surface coil
25	Galateia Kazakia	Variations in distal radius morphological and biomechanical indices among subjects with identical BMD values

26	Miki Sode	Quantitative characterization of motion artifact in the HR-pQCT images of distal radius and tibia
27	Rahwa Iman	HR-MAS Spectroscopy of Human Intervertebral Disc Tissue Demonstrates the Lactate/N-Acetyl Ratio as a Potential Marker
28	Ahilan Arulanandan	Association of Physical Activity with Focal Knee Lesions in Individuals with Risk Factors for Knee Osteoarthritis and Normal Controls - Data from the Osteoarthritis
29	Bryan Haughom	Abnormal Tibiofemoral Kinematics Following ACL Reconstruction are Associated with Early Cartilage Matrix Degeneration Measured by MRI T1rho
30	Dana Carpenter	Effects of Age and Sex on the Strength and Cortical Thickness of the Femoral Neck
31	Dimitrios Karampinos	T1 correction in multipeak T2*-IDEAL gradient-echo imaging for the quantification of intermuscular adipose tissue
32	Joyce Pang	Composition of osteoarthritic and osteoporotic femoral bone: a comparative FTIR study
33	Charles Fang	Relationship between Biomechanics and the Composition of Articular Cartilage
34	David Miller	Imaging MMP expressions and proteoglycans in human osteoarthritic knee
35	Kimberly Loo	Linking Gene Expression and Biochemical Composition Changes Using HR-MAS Spectroscopy in Human Osteoarthritic Cartilage
36	Roy Harnish	Non-invasive Protein Synthesis Rate Determination in Skeletal Muscle following Unilateral Exercise via Dynamic PET/CT with L-[methyl-11C]methionine
37	Gabby Joseph	The Spatial Distribution of Cartilage MR T2 in a Subset of the Incidence and Control Cohorts of the Osteoarthritis Initiative
38	Jin Zuo	Perfusion abnormalities of bone marrow edema-like lesions in knees with anterior cruciate ligament injury using dynamic contrast-enhanced MRI
39	Andrew Burghardt	Quantitative in vivo HR-pQCT Imaging of 3D Radiocarpal and Metacarpophalangeal Joint Space Distances in Rheumatoid Arthritis
40	Bryan Hermannsson	Bone Structure Changes in Hypertensive Rats using MicroCT Imaging
41	Nayela Keen	Clinical Utility of Magnetic Resonance Neurography of the Ulnar Nerve at the Elbow
42	Valerie Cardenas	Co-Analysis of Structural Imaging and DTI in Alzheimer's Disease
43	Yu Zhang	Dissociated Gray Matter Atrophy and Hypoperfusion in Alzheimer's Disease and Parkinson's Disease
44	Marzieh Nezamzadeh	Combined T1- And DTI Weighted Contrast for High Resolution Human Brain Mapping Using 3D MPRAGE
45	Norbert Schuff	Nonlinear Time Course Of Brain Volume Loss In Normal Aging And Cognitive Impairment
46	Cathy Scanlon	The impact of template selection on deformation based morphometry in MR-negative temporal lobe epilepsy
47	Monica Bucci	Structural Plasticity in Stroke inferred by probabilistic fiber tracking and MEG
48	Yiou Li	A novel variational Bayesian method for spatiotemporal decomposition of resting-state fMRI
49	David Pham	PET-Optical Dual Modality Imaging of Pancreatic Cancer Using Targeted Dendritic Nanoparticles
50	Nan Tian	8 Channel 3T Neonatal MRI Volume Phased Array Reciever
51	Piotr Habas	Detection of early brain folding patterns in normal human fetuses from in utero MRI

52	Olga Tymofiyeva	Diffusion tensor imaging in newborns: rejection of images affected by motion
53	Peder Larson	Hyperpolarized 13C 3D Dynamic MRSI with Compressed Sensing
54	Galen Reed	Rapid 5-minute Echo-Planar Spectroscopic Imaging of Prostate Cancer Patients at 3T
55	Kayvan Keshari	Hyperpolarized MR imaging at 14T and corresponding histopathology for the non-invasive characterization of the TRAMP model
56	Robert Bok	Hyperpolarized 13C Biomarkers of Androgen Independent Prostate Cancer
57	Bellina Chea	Accuracy of DW-MRI for Detection of Prostate Cancer after Radiation Therapy
58	Alessia Lodi	Magnetic resonance spectroscopy metabolic profiling reveals different mechanisms of action of PI3K and MAPK inhibitors in prostate cancer
59	Peter Shin	Multiband-Excitation and Multi-Echo Pulse Sequence for Hyperpolarized 13C Metabolic Imaging
60	Marram Olson	SIVIC: An Extensible Open-Source DICOM MR Spectroscopy Software Framework and Application Suite
61	Simon Hu	Effect of the Monocarboxylate Transporter Inhibitor ±-cyano-4-hydroxy-cinnamate on In Vivo Hyperpolarized 13C Spectroscopic Imaging
62	Subramaniam Sukumar	Single shot chemical shift specific imaging methods for hyperpolarized 13C studies at 14T

Oral Presentations I

Novel Antibody-Based Probes for the Detection and Study of Pre-Malignant Breast Cancer Cells

Christopher R. Drake,[1] David Miller,[1] Philippe Gascard,[2] Nancy Dumont,[2] Thea Tlsty,[2] Ella Jones.[1]

1. Centre for Molecular and Functional Imaging, University of California San Francisco, 185 Berry Street, Suite 350, Box 0946 San Francisco, CA 94107 2. Department of Pathology, University of California San Francisco, 513 Parnassus Avenue, HSW-513, Box 0511, San Francisco, CA 94143.

Introduction: Breast cancer is the most prevalent cancer in women. Every year in the US over 192,000 new cases are diagnosed, with ~62,000 of these women presenting at clinics with stage 0 ductal carcinoma *in situ* (DCIS). 12-15% of these patients will develop an invasive tumor within 10 years. Currently there are no reliable methods of identifying them causing both high morbidity due to over-treatment and high mortalities from under-treatment. Recently, our team discovered a population of variant human mammary epithelial cells (vHMECs), which show the correct phenotype for progression to malignancy. Through gene profiling, we identified a specific cell surface antigen for targeting vHMECs, allowing the development of highly specific imaging probes able to provide information on the behaviour of these cells *in vivo* as well as forming the basis of a clinically useful probe for early detection and prevention of breast cancer. Herein, we describe the successful development of this probe and demonstrate its *in vivo* efficacy.

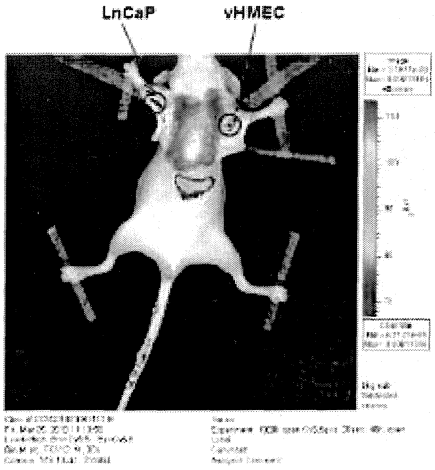

Figure 1: Fluorescence reflectance image showing specific labeling of vHMEC xenografts by anti-CDxx-AF680 probe.

Methods: We based our imaging probes on a proprietary antibody (anti-CDxx) specific to the cell surface epitope identified during our gene profiling studies. Using a combination of fluorescence microscopy and flow cytometry, we optimized the labeling of anti-CDxx with a near-IR fluorophore, Alexafluor-680 (AF-680), to produce an optical probe that retained its high affinity for vHMECs. Following successful *in vitro* evaluation of the probe it was tested *in vivo.* Nude mice were implanted in one mammary fat pad with luciferase-transfected vHMECs (2.5e5, 5e5 or 10e6) and in the contra-lateral pad with an equal number of a $CDxx^-$ cell line (LnCap, also transfected to express luciferase). Bioluminescence imaging was used to confirm successful implantation and 48 hours after cell implantation the probe (~1.5 nM based on AF680) was administered via tail vein injection. The mice were then imaged using both reflectance and tomographic techniques. To further assess the specificity of the probe xenograft models where mice were implanted with both basal (MDA-MB-231, SUM-159-PT, MDA-MV-468; all $CDxx^+$) and luminal (SKBR3, SUM-52-PE, MDA-MB-453; all $CDxx^-$) breast cancer cell lines in the contra-lateral fat pads were used to ascertain the probe's ability to discriminate between these two breast cancer sub-types.

Results: The probe effectively labeled vHMECs both *in vitro* and *in vivo*. As shown in figure 1 the presence of the vHMECs was clearly discerned upon surgical exposure of the mammary fat pad 24 hours after probe injection. In contrast the signal from the $CDxx^-$ implant was significantly (40%) lower. When tested in mice implanted with both basal and luminal breast cancer cell lines (figure 2), the fluorescence signal measured from the basal cells was significantly higher (student's t-test, one tailed, p=0.0029).

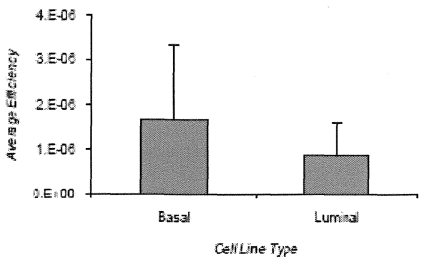

Figure 2: Average fluorescence efficiency measured by reflectance imaging of mammary fat pads implanted with either basal or luminel breast cancer cells Lines.

Conclusions: Our optical probe is able to selectively label $CDxx^+$ cells *in vivo*, fulfilling our initial goal of developing an imaging probe to facilitate the study of vHMECs. In addition our results indicate that it can be used to discriminate the more aggressive basal breast cancer sub-type from the luminal sub-type, pointing to its future clinical utility in personalized cancer treatment.

Bacteriophage-based nanoprobe targeting pancreatic cancer in transgenic mouse model

Feng, Jinjin[1]; Thomas, Stephanie A.[3]; Allen, Elizabeth[2]; Iyer, Arun K.[1]; Jones, Ella F.[1]; Hanahan, Douglas[2]; Kelly, Kimberly[3]; He, Jiang[1]; VanBrocklin, Henry F.[1];

1. Radiology and Biomedical Imaging, University of California San Francisco, San Francisco, CA.
2. Diabetes Center, University of California at San Francisco, San Francisco, CA.
3. Biomdeical Engineering, University of Virginia, Charlottesville, VA.

Abstract

Objectives: Imaging probes for incipient pancreatic ductal adenocarcinoma (PDAC) would enable earlier detection and guide therapeutic development. A bacteriophage (Pan27) has been identified that homes to pancreatic cancer by virtue of displaying a peptide that binds to Plectin 1, a cytoplasmic protein translocated to the cell surface. The targeted imaging properties of the phage with the expressed peptide were assessed.

Methods: The plectin-1 targeted bacteriophage (Pan27) and a non-specific control phage (HPC7) were coupled with Cy5.5 for optical imaging and with DTPA for indium-111 labeling. The phage were labeled with indium-111 for SPECT imaging. The biodistribution in both PDAC tumor mice and wild type mice, at 24 hours and 48 hours post-injection was determined.

Results: The two phage were successfully labeled with indium-111 with yields of 20-30% and 50-60% for the Pan27 and HPC7, respectively. Both probes were equally taken up in the tumor tissue at 24h. Tumor uptake for Pan27 remains constant (~2% ID/g) to 48h, while HPC7 washes out (0.86%ID/g) by 48h. Tumor to non-tumor ratios increased over time for Pan27 but are constant for HPC7. The two phage nanoprobes (Pan27 and HPC7) had nearly identical pharmacokinetic properties in wild type mice, weak binding to normal pancreas, with a loss of pancreas signal from 24h to 48h, indicating no specific binding.

Conclusions: A nanoprobe based on a bacteriophage (Pan27) demonstrated specific targeting to PDAC tumors in the genetically engineered mouse model. Further investigation for development of nuclear probes for early detection of pancreatic cancer is warranted.

Research Support: NIH R01CA119414, R01CA135358 and IRG-97-150-10 from the American Cancer Society.

References: Kelly KA, et al. Targeted nanoparticles for imaging incipient pancreatic ductal adenocarcinoma. Plos Medicine. 2008; 5(4): e85.

Assessing the Effects of Radiation Therapy on Normal Brain Tissue in Patients with Glioma using Susceptibility-Weighted Imaging at 7 Tesla

Janine M. Lupo[1], Cynthia Chuang[2], Bert Jimenez[1], Susan. M. Chang[3], Igor J. Barani[2], Christopher P. Hess[1], and Sarah J. Nelson[1,4]

[1]Department of Radiology and Biomedical Imaging, [2]Department of Radiation Oncology, [3]Department of Neurosurgery, and [4]Department of Bioengineering and Therapeutic Sciences, University of California, San Francisco

Introduction: Radiotherapy is an integral component in the management of patients with glioma, but its potential effect on neurocognitive ability and quality-of-life has recently become of great importance as new treatments extend survival. The histologic response to radiation includes vasculopathy, with the formation of cavernous angiomas that may slowly or acutely hemorrhage. The goal of this study was to use Susceptibility-Weighted imaging (SWI) at 7T to evaluate longer-term effects of radiation therapy on healthy brain tissue by assessing the number and location of the appearance of microbleeds as a function of time since treatment.

Methods: Twenty patients with stable gliomas were recruited for this study. Seventeen patients received prior external beam radiation therapy (x-RT), either with or without adjuvant chemotherapy, between 1 and 16 years prior to the time of imaging. Six patients treated with chemotherapy only from 1–6 years prior to imaging were scanned as controls. High resolution SWI was performed on a GE whole-body 7T scanner with 8-channel phased-array reception. To keep the scan time under 6 minutes, a GRAPPA-based parallel imaging acquisition was utilized with either a 2- or 3-fold reduction. Standard SWI post-processing was performed for each coil, and then combined, intensity corrected, and projected through 8 mm-thick slabs. Phase imaging was used to confirm the absence of calcification in these lesions. Clinical pre- and post-gad T1-weighted SPGR and T2-weighted FLAIR images were acquired at 3T immediately after the 7T exam and used to identify regions of contrast-enhancing lesion and T2-hyperintensity. Microbleeds were identified as discrete foci of susceptibility that did not correspond to vessels or hemosiderin staining of the surgical cavity on consecutive slices. The number of microbleeds was counted within the T2 hyperintense lesion excluding contrast-enhancing tumor (T2L), outside the T2L, and in the contralateral hemisphere of the original tumor. For two patients, radiation dosimetry maps were reconstructed on a Philips Pinnacle treatment planning system and fused with the 7T SWI data after alignment to the original treatment CT images using mutual information.

Results: 7T SWI scans revealed an increase in both the total number of microbleeds and the percent of which resided outside the T2 lesion with time from radiation therapy. Patients who received solely chemotherapy did not exhibit microbleeds as far as 6 years from onset of therapy. After 5 years post-RT, there was a larger variation in the number of lesions, which could be due to differences in the extent of radiation dose received to healthy brain tissue. In the two patients with dose-maps, the majority of these microbleeds resided within tissue that received 50% of the maximum dose.

Conclusions: High-field SWI has potential for visualizing the appearance of hemosiderin containing microbleeds associated with long-term effects of radiotherapy on brain tissue. The prevalence of these lesions increases over time since receiving radiation therapy. The ability to visualize these lesions in normal brain tissue may be important in further understanding the utility of this treatment in patients with grade 2 and grade 3 tumors with longer survival rates.

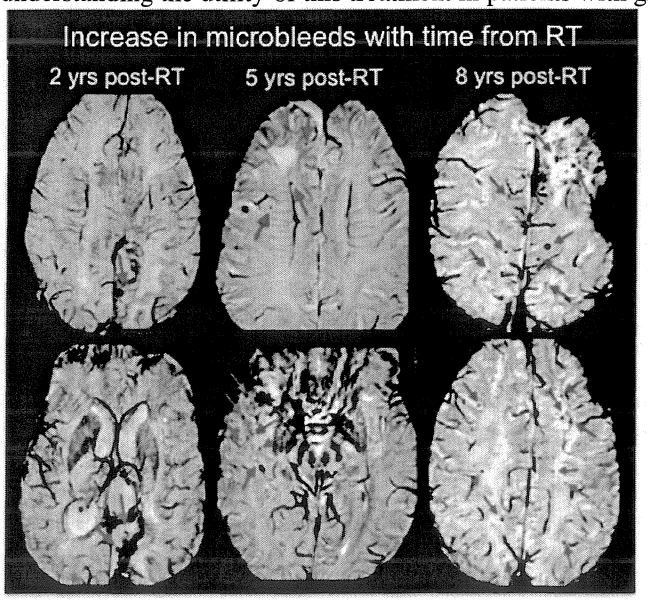

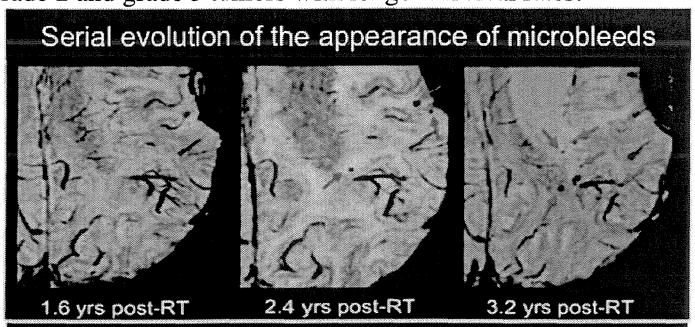

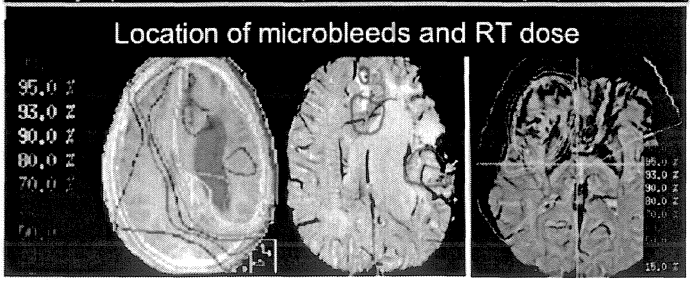

Anatomic and Physiologic MR Imaging Characterizes Cellular and Genetic Expression Patterns of Angiogenesis in Glioblastoma Multiforme

R. Barajas, J. Phillips, J. Graeme Hodgson , J. Chang, S. Vandenberg, A. Parsa, M. McDermott, M. Berger, W. Dillon, S. Cha

Purpose: Glioblastoma multiforme (GBM) clinically exhibits varying degrees of contrast enhancement resulting in heterogeneous appearance on MRI. The purpose of this study was to prospectively collect MR image guided biopsy specimens from multiple regions of GBM to investigate if quantitative anatomic and physiologic dynamic susceptibility (DSC) weighted MR imaging measurements are influenced by cellular and genetic expression patterns of tumor angiogenesis.

Materials & Methods: 25 biopsy specimens from 10 adult patients with treatment-naïve GBM were studied. Preoperatively, enhancing and peri-tumoral non-enhancing regions with highest tumor cerebral blood volume (rCBV) were selected for biopsy (Figure 1A&B). rCBV and percentage of signal intensity recovery measurements were obtained using clinically available GE functool software. Intraoperatively, pre-planned biopsy regions were localized and sampled using BrainLAB neuronavigational system. Biopsy specimens were histopathologically examined for quantification of tumor microvascular density and hypoxia. Regional angiogenic expression patterns were investigated using RNA microarrays. MR imaging and histopathologic variables were compared using Welch T tests and Pearson's correlations. Microarray analysis was performed using false discovery rate (FDR) statistics.

Results: Ten adult patients provided 13 contrast enhancing and 12 peri-tumoral non-contrast enhancing biopsy specimens which were infiltrated with malignant tumor cells. Contrast enhancing regions demonstrated significantly elevated DSC perfusion weighted MR imaging and histopathologic expression of angiogenesis when compared to peri-tumoral non-contrast enhancing regions. Four angiogenic pathways (VEGF-A, PDGF, HIF, FGF), 25 individual genes, were found to have statistically significant up-regulation within contrast-enhancing regions when compared to peri-tumoral non-contrast enhancing regions (Adj $P< 0.05$, $FDR< 0.05$, $B> 0$). A statistically significant correlation between VEGF-A-T1, HIF1α, and CA-IX probe intensity was observed ($P< 0.05$). VEGF-A-T1 expressed the greatest degree of intra and inter-tumoral expression heterogeneity. A significant correlation was observed between VEGF-A-T1 expression and histopathologic & MR imaging measurements ($P<0.05$; Figure 1C).

Conclusion: Our findings suggest that similar appearing contrast enhancing regions on MR imaging demonstrates a large variation in genetic expression patterns that can be further characterized utilizing physiologic MR imaging. Furthermore, these MR imaging variables may represent noninvasive biomarkers that may be used to quantify VEGF expression, BBB integrity, microvascular morphology, and other clinically important features of GBM angiogenesis.

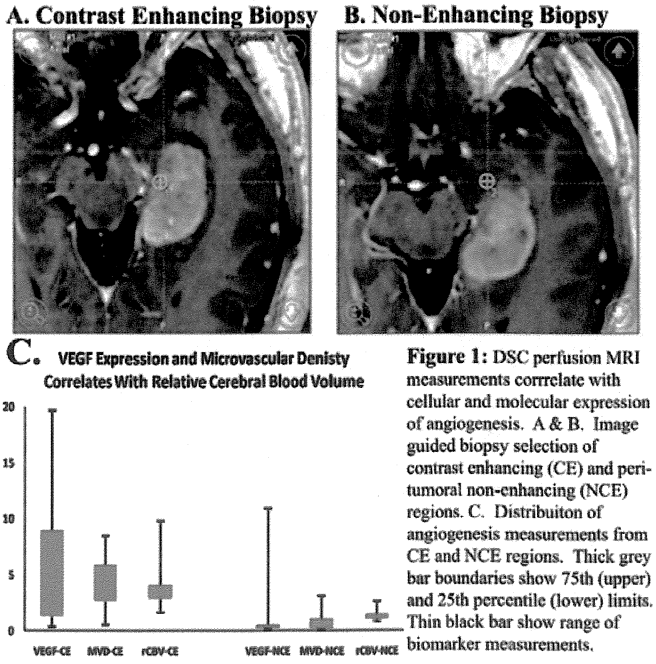

Figure 1: DSC perfusion MRI measurements corrrelate with cellular and molecular expression of angiogenesis. A & B. Image guided biopsy selection of contrast enhancing (CE) and peri-tumoral non-enhancing (NCE) regions. C. Distribuiton of angiogenesis measurements from CE and NCE regions. Thick grey bar boundaries show 75th (upper) and 25th percentile (lower) limits. Thin black bar show range of biomarker measurements.

Multi-compound Hyperpolarization allows Simultaneous Assessment of Multiple Enzymatic Activities *In Vivo*

David M. Wilson, Kayvan R. Keshari, Peder E. Z. Larson, Albert P. Chen, Simon Hu, Mark Van Criekinge, Robert Bok, Sarah J. Nelson, Jeffrey M. Macdonald, Daniel B. Vigneron, and John Kurhanewicz

INTRODUCTION: Hyperpolarized ^{13}C MR spectroscopy has emerged as a powerful new modality in molecular imaging, with a rapidly expanding arsenal of endogenous ^{13}C probes including pyruvate, bicarbonate, fumarate and fructose [1-4]. As the number of useful dynamic nuclear polarization (DNP) agents grows, the ability to probe multiple pathways simultaneously may provide valuable metabolic "signatures" associated with specific types of diseased tissue. ^{1}H MRS is an established modality to characterize diseased tissue *in vivo* [5,6] but hyperpolarized MR has the additional capacity to provide kinetic information. As a proof of concept, four ^{13}C labelled substrates were polarized simultaneously, namely [1-^{13}C] pyruvate, ^{13}C bicarbonate, [1,4-^{13}C] fumarate, and ^{13}C urea, potentially providing information on glycolysis, pH, necrosis and perfusion in a single imaging experiment lasting only seconds.

Compound	T_1 (s) multipol	T_1 (s) alone	%polarization multipol	% polarization alone
^{13}C bicarbonate	43.3±1.2	48.7±0.6	10.3±1.8	12.7±1.9
[1-^{13}C] pyruvate	48.3±1.5	48.3±0.6	17.5±3.4	17.4±1.5
[1,1-^{13}C] fumarate	29.0±1.0	29.3±0.6	15.6±1.9	12.0±0.7
[1-^{13}C] urea	43.0±1.0	44.0±0.3	11.6±2.5	12.4±0.4

METHODS: ***Agent polarization:*** ^{13}C agents were purchased from Isotec (Miamisburg, OH) and polarized on the Hypersense (Oxford Instruments) as published previously [7]. ***In vitro experiments:*** % polarizations were quantified by measuring the hyperpolarized signal compared to that at thermal equilibrium on a 11.7T Varian INOVA spectrometer. For T_1 calculations, magnitude decay curves were fit to a mono-exponential function. ***Imaging studies:*** *In vivo* data were obtained in a Transgenic Adenocarcinoma of Mouse Prostate (TRAMP) model using a 3T GE Signa™ scanner equipped with the MNS (multinuclear spectroscopy) hardware package. ^{13}C spectroscopic imaging was acquired using a modified double spin-echo sequence [8].

RESULTS: Calculated T_1's and enhancements in the multi-metabolite case were similar to those recorded for ^{13}C probes polarized individually (Table). Resolution of all four metabolites *in vivo* was demonstrated at high SNR (Figure).

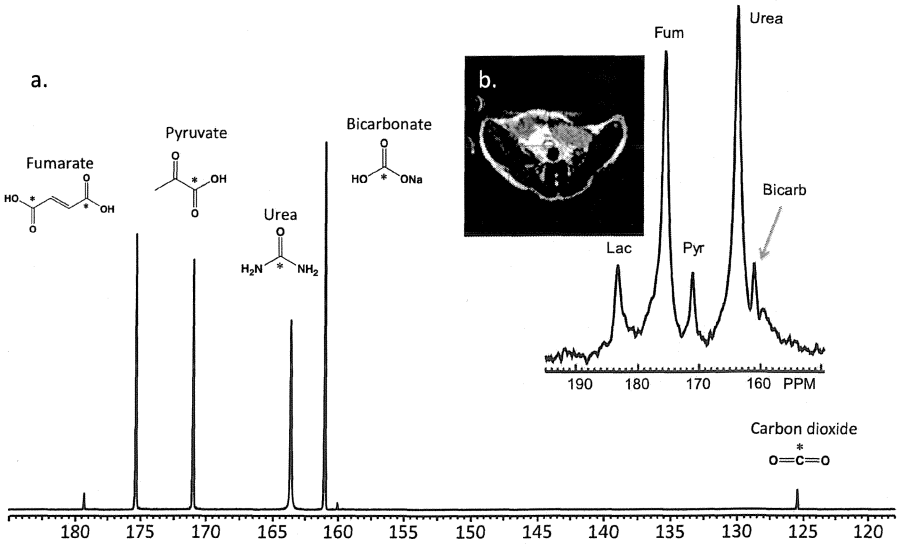

DISCUSSION: Multi-metabolite polarization is intended to circumvent one of the main drawbacks of DNP, namely its long polarization times, by polarizing several precursors at the same time, and then developing a biological scenario whereby the inevitably very complex metabolic data *in vivo* can be analyzed. This approach will be increasingly useful as ^{13}C probes continue to proliferate.

REFERENCES:

[1] Golman K et al. Cancer Res 2003; 100(18): 10435-10439. **[2]** Gallagher F et al. Nature 2008; 453(7197): 940-943. **[3]** Gallagher F et al. PNAS 2009; 106(47): 19801-19806. **[4]** Keshari K et al. J Am Chem Soc 2009; 131(48): 17591-17596. **[5]** Dillon W et al. AJNR 1999; 20(1): 2-3. **[6]** Kurhanewicz J et al. J Magn Reson Imaging 2002; 16(4): 451-463. **[7]** Ardenkjaer-Larsen J et al. PNAS 2003; 100(18): 10158-10163. **[8]** Cunningham C et al. J Magn Reson 2007; 187(2): 357-362.

Depth-of-interaction compensation using a focused-cut scintillator for a pinhole gamma camera

Fares Alhassen[1], Haris Kudrolli[2], Bipin Singh[2], Sangtaek Kim[1], Vivek Nagarkar[2], Youngho Seo[1], Robert G. Gould[1]

Preclinical single photon emission computed tomography (SPECT) offers a powerful means by which to understand the molecular pathways of drug interactions in small animal models of human diseases and thus evaluate new therapeutics for potential clinical applications. A combination of high spatial resolution and sensitivity are both required in order to map radiopharmaceutical uptake within small animals. We have been investigating the use of multiple pinhole collimators, as they offer high resolution by means of image magnification and high sensitivity by means of multiple apertures. One of the limitations of pinhole geometries is that increased magnification causes rays to travel through the detection scintillator at steeper angle, introducing parallax errors due to variable depth-of-interaction in scintillator material, especially towards the edges of the detector field of view. These parallax errors ultimately limit the resolution of pinhole SPECT systems, especially for higher energy isotopes that can easily penetrate through millimeters of scintillator material. A pixellated, focused-cut (FC) scintillator, with its pixels laser-cut so that they are collinear with incoming rays, can compensate for these parallax errors and thus open up a new regime of sub-mm preclinical pinhole SPECT. Fig. 1 illustrates parallax errors in continuous and straight-cut (SC) pixellated scintillators and shows how the FC scintillator design eliminates such errors.

We perform the first experimental evaluation of a newly developed FC Cs:I(Tl) scintillator, shown in Fig. 2(a) and (b). We scan a disk-like Co-57 source across the field of view of pinhole gamma camera with a continuous scintillator, an SC scintillator, and the FC scintillator, each coupled to a highly sensitive electron-multiplying charge-coupled device (EMCCD) by a fiber-optic taper, and compare the measured full-width half-maximum (FWHM) values. We show that the FWHMs of the FC scintillator projections are comparable to the FWHMs of the thinner SC scintillator (Fig. 2(c)) and thus demonstrate the effectiveness of the FC scintillator in compensating parallax errors.

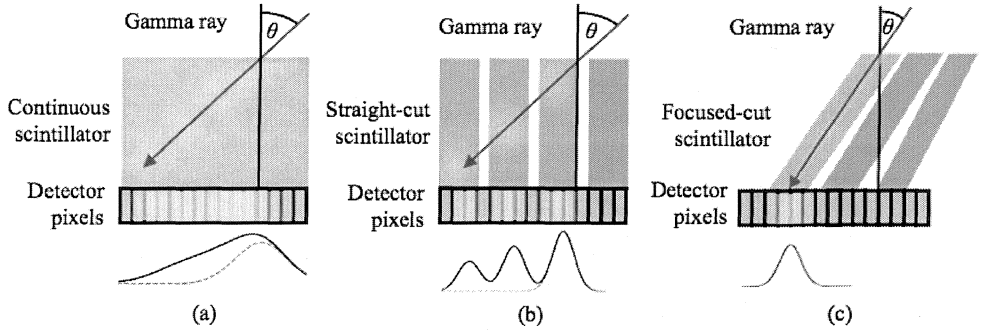

Fig. 1. Illustration of parallax errors in (a) a continuous scintillator and (b) a SC scintillator. The FC scintillator design (c) eliminates such parallax errors. The dashed red line profiles indicate the image line profile without the effect of parallax errors while the solid black line profiles indicate the actual detected line profile. The ray entry angle is θ.

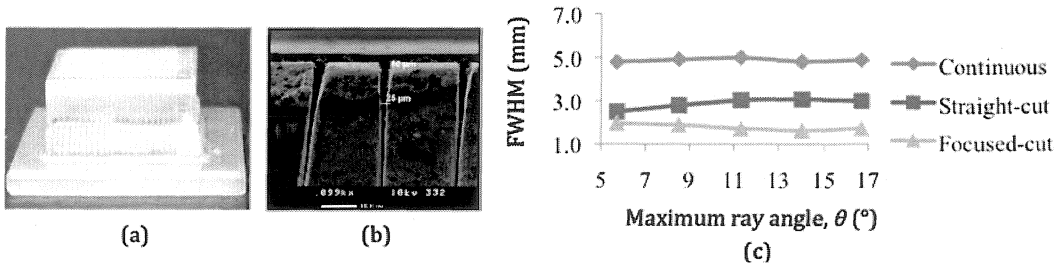

Fig. 2. (a) A photograph and (b) SEM micrograph of the 3 mm thick Cs:I (Tl) FC scintillator. (c) Plot of the FWHM vs. maximum ray angle, θ, for a set of projection data obtained using three different scintillator cuts.

[1]UCSF Physics Research Laboratory, Department of Radiology and Biomedical Imaging, University of California, San Francisco, 185 Berry St. Suite 350, San Francisco, CA 94017 USA.
[2]Radiation Monitoring Devices, Inc., 44 Hunt Street, Watertown, MA 02472 USA.

A Rational Basis for Selection of Contrast Material Combinations for Dual Energy CT Imaging: Lessons from Three-Material Decomposition of Contrast Materials

Rahi Kumar, BS, Carlos Forsythe, BS, Zhang A. Yang, MD, Yanjun Fu, PhD, Zhen J. Wang, MD, John Shepherd, PhD, Ella F. Jones, MD, Benjamin M. Yeh, MD

Purpose: To delineate the ability of dual energy CT to quantify contrast material concentrations in mixed solutions.

Material and Methods: We scanned a total of 149 CT phantoms with known dilutions of one or two contrast materials at 80 and 140 kVp. Contrast materials containing iodine, gadolinium, barium, calcium or tungsten were used. The 80:140 kVp CT number ratios for each contrast material were measured. We calculated contrast material concentrations for all phantoms using three-material basis decomposition.

Results: The 80:140 kVp CT number ratios for single contrast material iodine, gadolinium, barium, calcium, and tungsten-containing phantoms were 1.67, 1.33, 1.67, 1.56, and 1.08, respectively. For phantoms containing two contrast materials, the CT quantification error for a given material was inversely related to 1) the proportional contribution of that contrast material to the overall CT number and 2) the difference between the 80:140 kVp CT number ratio with that of the other material. When a given contrast material contributed <25%, 26-50%, 51-75%, and 76-100% of the overall CT number of a phantom, the mean quantification error was 70%, 31%, 21%, and 18%, respectively ($p < 0.001$). The least overall quantification error (mean, 4.5%) was observed for contrast material pairs with maximal differences in their 80:140 kVp CT number ratios.

Conclusion: Contrast material combinations can be chosen rationally to either maximize or minimize quantification errors at dual energy CT. Understanding this potential opens the way to develop contrast material combinations for specific clinical dual energy CT applications.

Clinical Relevance: For dual energy CT, contrast material combinations can be chosen rationally and tailored to clinical needs based on their 80: 140 kVp CT number ratios.

A Trabecular Bone Analysis Framework for High-resolution MRI of the Proximal Femur

Jenny Folkesson[1], Julio Carballido-Gamio[2], Dimitrios C. Karampinos[1], Thomas Baum[1], Thomas M. Link[1], Sharmila Majumdar[1], and Roland Krug[1]
[1]Department of Radiology and Biomedical Imaging, University of California, San Francisco, CA, United States
[2]Grupo Tecnológico Santa Fe, S.A. de C.V., Mexico City, Mexico

Introduction

Osteoporotic fractures of the proximal femur are very common and often result in high rates of morbidity and mortality. However, *in vivo* imaging of deep sited regions like the proximal femur is challenging[1]. Thus, images of the proximal femur with high spatial resolution and SNR have previously not been feasible clinically. Furthermore, the presence of red and yellow bone marrow (Fig. 1b) complicates the analysis. The purpose of this work was to demonstrate the feasibility of an *in vivo* proximal femur analysis framework, including high resolution image acquisition, automatic volume of interest (VOI) placement, and fuzzy trabecular bone segmentation.

Materials and Methods

High-resolution (HR) images of 12 proximal femurs were acquired on a 3T GE MR750 system using an 8 channel phased array coil and a fully balanced steady state free precession pulse sequence (TR/TE 8.6ms/3.09ms, flip angle 60º, bandwidth ±62.5 kHz, voxel size 0.23×0.23×0.5mm)[1]. IDEAL (Iterative Decomposition of water and fat with Echo Asymmetry and Least-squares estimation) water-only images were acquired with half the spatial resolution.

An IDEAL atlas was created by automatically by 3D multiresolution affine registration of 9 scans to a reference, followed by 3D free-form deformations[2]. Transformations were applied to create an HR atlas where a spherical VOI was prescribed. Using affine registrations and FFDs, the IDEAL atlas was automatically registered to the 2 scans which were not used to build the atlas.

Trabecular bone was segmented using dual thresholding, and a novel fuzzy clustering based technique, BE-FCM[3], which generates a partial membership segmentation based on multi-scale local structural information.

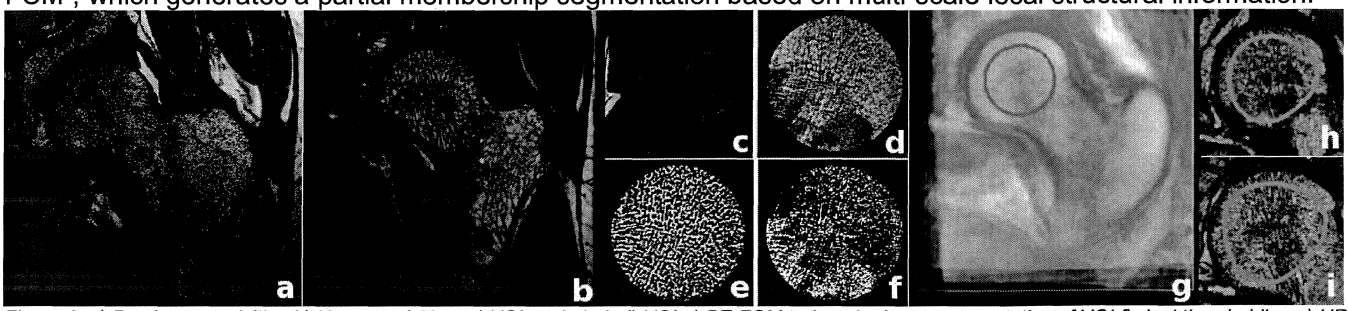

Figure 1. a) Previous acquisition b) New acquisition. c) VOI encircled. d) VOI e) BE-FCM trabecular bone segmentation of VOI f) dual thresholding g) HR atlas. h) and i) Automatic VOI placement using atlas in 2 scans.

Results and Discussion

The new high-resolution images using new hardware technology demonstrate superior image quality compared to previous acquisitions (Fig. 1a-b), with a substantial gain in SNR (1.7-trochanter, 3.0-head).

Edges are clearly visible in the HR atlas, indicating that the anatomical variability was well accommodated (Fig 1g). Anatomical correspondence of the VOI in two subjects can be easily appreciated (Fig. 1h-i). The feasibility of constructing an atlas of the proximal femur to prescribe VOIs and automatically place them in other subjects has been demonstrated.

The local structure information gain in BE-FCM improved trabecular bone segmentation compared to dual thresholding in the presence of red and yellow marrow (Figure 1c-f). The mean apparent bone fraction was lower with BE-FCM than with thresholding (0.27 (±0.01) vs. 0.50 (±0.04), $p<10^{-10}$).

The demonstrated improvements in image quality and trabecular bone segmentation, with consistent VOI placement, allows for *in vivo* trabecular bone analysis of the entire proximal femur. This makes the framework potentially very interesting in fracture prediction analysis throughout the proximal femur[4].

This work was supported by NIH R01 AR057336 (RK) and AG017762 (SM)

References
[1]Krug R, Banerjee S, Han ET, Newitt DC, Link TM, Majumdar S. Osteoporos Int. 2005;16(11):1307-14.
[2]Rueckert et al. IEEE-TMI, 22(8)-2003.
[3]Folkesson J, Carballido-Gamio J, Link TM, Majumdar S. Med Phys. 2009.
[4]Li W, Kornak J, Harris T, Keyak J, Li C, Lu Y, Cheng X, Lang T. Bone 2009; 44; 596-602.

Knee cartilage T2 characteristics and evolution in relation to morphological abnormalities detected by 3T MRI: a longitudinal study of the normal control cohort from the Osteoarthritis Initiative

Judong Pan, M.D., Ph.D.[1], Jean-Baptist Pialat M.D., Ph.D. [2], Tom Joseph[3], and Thomas M. Link, M.D.[1]

Department of Radiology and Biomedical Imaging, University of California San Francisco[1]; Hopital Edouard Herriot, Lyon, France[2]; School of Medicine, University of California San Francisco[3]

Purpose: To study the prevalence of osteoarthritis (OA) related knee morphological abnormalities in healthy individuals using 3T MRI and investigate the characteristics and evolution of cartilage T2 values in relation to morphological abnormalities with a longitudinal study.

Methods: 100 subjects aged 45 to 78 and free of OA symptoms or risk factors were selected from the Osteoarthritis Initiative (OAI) normal control cohort. Both baseline and 2-year follow-up data were analyzed. Knee abnormalities were analyzed using the whole-organ MR imaging score (WORMS) by three radiologists. Cartilage T2 maps were created using the sagittal 2D multi-echo spin echo images of the right knee. Statistical significance was determined using Student's *t*-test, ANOVA, multivariate correlation tests, χ^2 tests, and multiple regression models.

Results: We identified a high prevalence of focal knee abnormalities in asymptomatic, OA risk factor free subjects, with 90% of study subjects having at least one lesion detected by 3T MRI at baseline and 91% at 2-year follow-up. Among all the knee structures analyzed, cartilage was found to have a particularly high prevalence of morphological abnormalities, with 85% of subjects having at least one cartilage lesion at baseline and 83% at follow-up. We found a significant longitudinal increase in cartilage T2 values (all compartments combined) over a two year period (43.0482 at follow-up versus 42.2076 at baseline, p = 0.0002) (Table 1). All cartilage compartments showed significant T2 elevation except for patella and trochlea. Subjects with greater longitudinal T2 elevation (ΔT2, all compartments combined) had significantly higher cartilage T2 values at 2-year follow-up (42.4130 ± 2.12 versus 43.6835 ± 2.58, p = 0.0043). Regression analysis of longitudinal changes in cartilage WORMS scores ($\Delta WORMS_{cartilage}$, all compartments combined) using ΔT2 as a predictor showed a significant linear relationship between these two variables (ΔWORMS = 0.1117401 + 0.0557426 x ΔT2, p = 0.043).

Conclusions: There is a high prevalence of preclinical OA in healthy individuals as evidenced by knee abnormalities detected by 3T MRI. A significant longitudinal cartilage T2 elevation over two years was detected. Greater T2 elevation was associated with increased progression of OA-related morphological abnormalities, suggesting that longitudinal cartilage T2 changes may be helpful in identifying people at risk for developing early OA, and that MR-based cartilage T2 quantification may be useful as a biomarker for detection of early cartilage changes in preclinical OA.

Compartments	Cartilage T2 Values		*P*
	Baseline	Follow-up	
All Combined	42.21	43.05	0.0002*
Patella	41.90	41.90	0.9982
Trochlea	49.35	48.45	0.9615
Medial Femoral Condyle	48.25	50.03	0.0001*
Lateral Femoral Condyle	44.04	45.45	0.0017*
Medial Tibia	34.11	36.00	0.0001*
Lateral Tibia	35.60	36.46	0.0188*

Table 1. Comparison of mean cartilage T2 values (individual compartments and all compartments combined) at baseline and 2-year follow-up using paired student t-test. A *P* value of less than 0.05 was considered to indicate a significant difference.

Oral Presentations II

Relationship Between Regional Brain Amyloid-β Deposition and Brain Atrophy Rates in Mild Cognitive Impairment

Duygu Tosun, Norbert Schuff, William Jagust, Michael W. Weiner, and Alzheimer's Disease NeuroImaging Initiative

Background: AD begins with amyloid-β accumulation in the brain, leading to synaptic dysfunction, neurodegeneration, and cognitive/functional decline. The earliest detectable changes seen with neuroimaging appear to be amyloid-β accumulation detected by PiB-PET. However, some individuals appear to tolerate high brain amyloid-β loads without developing symptoms, while others progressively decline, suggesting that localization and rate of atrophy and severity of clinical symptoms might be dependent on the spatial distribution of the amyloid-β accumulation. The relationship between amyloid-β and atrophy rates in human subjects has not been yet examined. Therefore, we examined the relationship between regional amyloid-β accumulation and brain atrophy rates in ADNI patients with mild cognitive impairment(MCI).

Methods: Brain atrophy rates in ADNI structural-MRI set of 61 MCI patients(baseline-age:75±8yrs) was measured by nonlinearly deforming 1-year follow-up images to their baseline images using a fluid-flow warp algorithm. Local Jacobian determinants, reflecting fractional volume contraction or expansion, were calculated to obtain a map of annual brain atrophy rates. PiB-SUVR images(standardized-uptake-value-ratio relative to the cerebellum) at baseline were rigidly co-registered to the corresponding structural MRI. Resampled PiB-SUVR and Jacobian maps were further spatially normalized to an unbiased average structural brain image created from the entire study population and then smoothed to achieve a uniform isotropic resolution of 8mm-FWHM.We then performed a joint analysis of the PiB-PET and MRI data using parallel independent component analysis (pICA), to determine patterns of common modulations between atrophy rates and amyloid-β accumulation levels in the same or distal brain regions.

Results: pICA identified significant relationships between two patterns of amyloid-β accumulation and atrophy rates:(1) Increased PiB-SUVR in the *left* precuneus/cuneus and medial-temporal regions was associated with increased atrophy rates in the *left* medial-temporal and parietal regions($r=0.739; p<0.0001$);(2) In contrast, increased PiB-SUVR in bilaterel precuneus/cuneus and parietal regions was associated with increased atrophy rates in the *right* medial temporal regions($r=0.612; p=0.03$).

Discussion: Our major finding links the greater amyloid-β deposition in the precuneus, a region generally known for accumulation of amyloid plaques during the early course of the disease, to a unique within hemisphere patterns of accelerated atrophy, resembling the pattern seen also in AD. These results may begin to shed light on the mechanisms by which amyloid-β deposition leads to neurodegeneration and cognitive decline and the development of a more specific AD-specific imaging signature for diagnosis.

1st component (r=0.739; p<0.0001)

Annual rate of atrophy

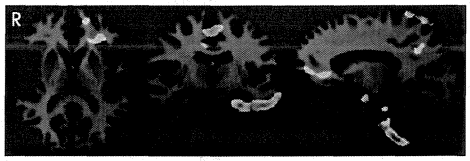

PiB SUVR

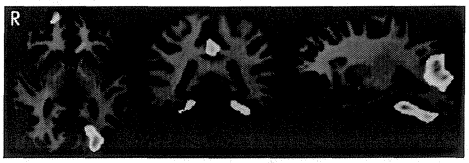

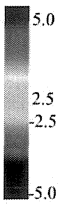

Larger annual rates of atrophy in the left entorhinal, fusiform, hippocampus, parahippocampal, posterior cingulate, inferior-middle-superior temporal, amygdala, precuneus, superior parietal, and superior frontal regions are associated with larger amyloid β accumulation in the left inferior parietal, pre-cuneus, superior parietal, posterior cingulate, fusiform, lingual, entorhinal areas as well as in the right lateral fronto-orbital and inferior frontal regions.

2nd component (r=0.612; p=0.03)

Annual rate of atrophy

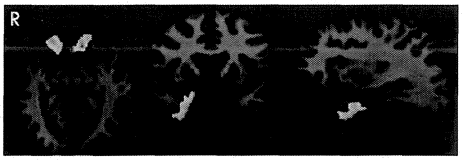

PiB SUVR

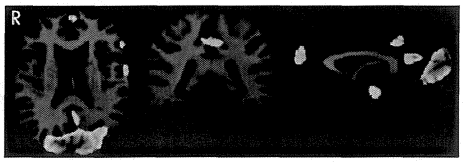

Larger annaul rates of atrophy in the right inferior-superior temporal, entorhinal, fusiform gyrus, parahippocampal, hippocampus, amygdala, subcallosal, middle fronto-orbital, and gyrus rectus are associated with larger amyloid β accumulation in bilateral inferior parietal lobule, posterior cingulate, pre-cuneus, cuneus, supramarginal, superior parietal, and left superor frontal regions.

Diagnostic Accuracy of Fetal MRI for Supratentorial Brain Abnormalities

Zary Hashemi, Addison Cuneo, Jim Barkovich, Agnes Bartha, Orit Glenn

Purpose
To determine the sensitivity and specificity of fetal MRI for supratentorial brain abnormalities using postnatal MRI as gold standard.

Materials & Methods
We identified all patients imaged by fetal MRI who had postnatal brain MRI brain. Fetal MRIs included single shot fast spin echo T2 weighted imaging with 3-4mm thick slices obtained in axial, sagittal, and coronal planes. Postnatal MRI technique varied as they were performed at different sites. Fetal MRIs and postnatal MRIs were reviewed in a blinded manner by 2 pediatric neuroradiologists. Cases of periventricular nodular heterotopia, polymicrogyria, callosal abnormalities, and abnormal white matter T2 signal detected by fetal MRI and/or postnatal MRI were compared.

Results
A total of 77 patients were identified. Gestational age (GA) at time of fetal MRI by last menstrual period ranged from 19.71-38.14 weeks (median GA 24.29 weeks). Age at postnatal MRI ranged from 0 days – 4 years. 12 patients had periventricular nodular heterotopia on postnatal MRI, 10 patients had polymicrogyria on postnatal MRI, 18 patients had white matter abnormalities on postnatal MRI, and 34 patients had callosal abnormalities (18 agenesis/hypogenesis, 1 dysgenesis, 15 thin) on postnatal MRI. Sensitivity and specificity of fetal MRI for heterotopia was 58% and 100%, respectively. Median GA at fetal MRI for cases of heterotopia detected by both fetal MRI and postnatal MRI was 26.14 weeks, compared with median GA of 22.29 weeks for those cases detected by postnatal MRI but not fetal MRI.
Sensitivity and specificity of fetal MRI for polymicrogyria was 80% and 100%, respectively. Median GA at the time of fetal MRI for those cases of polymicrogyria detected by both fetal MRI and postnatal MRI was 31.14 weeks, compared with median GA of 24.22 weeks for those cases detected by postnatal MRI but not fetal MRI. Sensitivity and specificity of fetal MRI for white matter signal abnormalities were 28% and 93%, respectively. Parenchymal abnormalities not detected by fetal MRI included focal as well as diffuse white matter hyperintensity, perinatal infarcts, and subcortical tuber in a patient with tuberous sclerosis. Median GA at the time of fetal MRI for cases of white matter signal abnormalities detected by both fetal and postnatal MRI was 32.29 weeks, compared with median GA of 25 weeks for those cases detected only by postnatal MRI. Sensitivity and specificity of fetal MRI for callosal abnormalities overall was 68% and 100%, respectively. When cases of thin callosum were excluded, fetal MRI was 89% sensitive in detecting callosal abnormalities.

Conclusion
The sensitivity and specificity of fetal MRI varies for different abnormalities and gestational ages. It has highest diagnostic accuracy for polymicrogyria, followed by callosal abnormalities, and periventricular nodular heterotopia; and detection is improved at greater gestational ages. Fetal MRI is more limited in detection of white matter signal abnormalities. Knowledge of the diagnostic accuracy of fetal MRI for different brain abnormalities is important in accurate counseling of patients who undergo fetal MRI.

HRMAS NMR Spectroscopy - An important tool in Understanding Joint Degradation in Osteo-Arthritis

Shet K, Siddiqui SM, Kurhanewicz J, Ries Michael, Yoshihara H, Li X

Abstract

The N-Acetyl resonance observed in High Resolution Magic Angle Spinning (HRMAS) NMR spectra (2.04 ppm) arises from the proteoglycan content in cartilage. We aim to detect the changes in the mobility of the N-acetyl moiety due to the degradation process that occurs in osteo-arthritic (OA) cartilage as reflected in the relaxation parameters of the entity (T_2). An increase in T_2 relaxation time is observed in case of ex-vivo human OA cartilage samples. An increase in the T_2 relaxation time of the water protons has also been observed in OA. The water T1-rho dispersion characteristic of OA cartilage and synovial fluid (SF) is reported. An attempt has also been made to use HRMAS spectroscopy to investigate the role of reactive oxygen species (ROS) namely hypochlorous acid (HOCl) in joint tissue degradation in OA.

Materials and methods

OA cartilage samples were harvested from 6 patients who underwent Total Knee Arthroplasty (TKA) surgeries; and 4 healthy (control) samples were extracted from NDRI cadavers using 3.5 mm biopsy punches from the lateral inferior femoral condyle. The samples were flash frozen at -80°C for storage. The samples were scanned in a 500MHz Varian spectrometer in a zirconium rotor which was spun at a rate of 2.25 KHz. The T_2 relaxation time was measured using the Carr-Purcell-Meiboom-Gill (CPMG) sequence. A T_1-rho pulse sequence capable of spin-locking any metabolite of interest was developed in-house. Increase in T1-rho with increasing spin-lock frequencies was measured. The T_2 and T_1-rho curve fitting was performed using the curve fitting toolbox in MATLAB.

Results

	N-Acetyl T_2 (ms)
CONTROL	38.16±8.34
OA	65.16±7.18

Table 1. T_2 relaxation times of N-Acetyl in OA and healthy cartilage. Values provided are mean ± SD

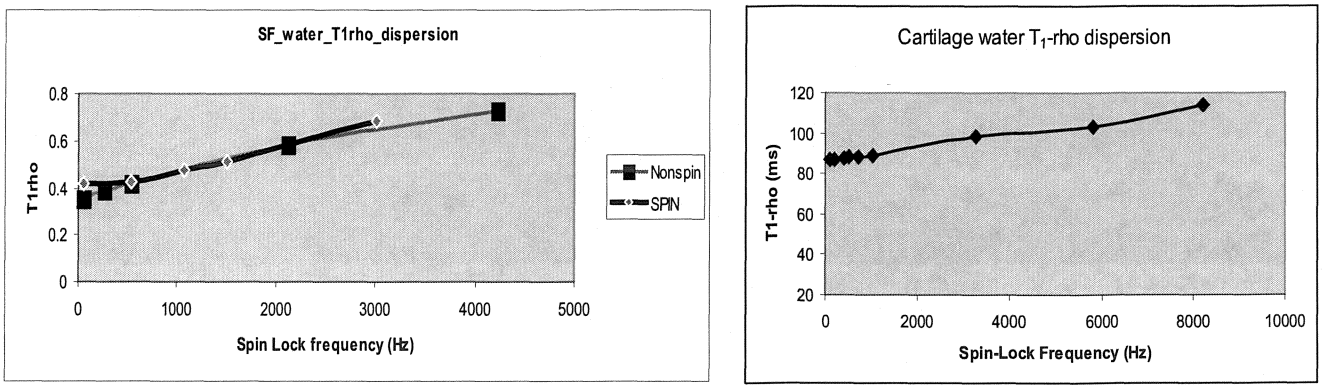

Figure 1 T_1-rho dispersion of water in (a) Synovial_fluid measured using non-spin NMR and HRMAS (b) Cartilage

Discussion

An increase in T_2 relaxation time of the N-acetyl resonance is observed in OA cartilage compared to controls. This can be attributed to the increase in mobility of the N-acetyl moiety of the GAG macromolecules in cartilage as a result of the degradation in OA. T_1-rho dispersion characteristics of specific metabolites in cartilage and synovial fluid is an important tool in gaining a better understanding of the biochemical changes involved in OA and helps to complement T_1-rho MR imaging which shows immense potential in early diagnosis of OA. The dispersion property may serve as a distinguishing tool between OA and healthy cartilage. HRMAS spectroscopy also provides the ability to analyze cartilage samples and detect the presence of metabolites that result from degradation specifically induced by OA. An increased concentration of acetate resulting from the degradation of the N-Acetyl side-chain of the GAG polymers induced by the ROS species namely hypochlorous acid (HOCl) has been detected in OA cartilage samples and may serve as an OA bio-marker. Our long-term goal following identification of the class of ROS responsible for joint tissue degradation is to study the pharmacological response to targeted anti-oxidant therapy in OA in animal models which can then be extended to humans.

Detection of inflammatory arthritis using hyperpolarized [1-^{13}C]pyurvate with magnetic resonance imaging and spectroscopy

John MacKenzie, Yi-Fen Yen, Dirk Mayer, James Tropp, Ralph Hurd, Daniel M. Spielman

This work examines the feasibility of MRI with hyperpolarized carbon-13 (^{13}C) labeled pyruvate for detecting inflammation. The lactate dehydrogenase-catalyzed conversion of pyruvate to lactate was measured in inflamed and control paws of arthritic rats using ^{13}C magnetic resonance spectroscopic imaging (^{13}C-MRSI). Arthritis was induced in the right hind paw of rats (n = 6) and the left hind paw served as an internal control. Clinical and histological data were obtained to confirm the presence and severity of arthritis. Hyperpolarized [1-^{13}C]pyruvate was intravenously injected into the arthritic rats prior to simultaneous imaging of both paws with ^{13}C-MRSI. Inspection of the spectroscopic profiles of [1-^{13}C]pyruvate and converted [1-^{13}C]lactate showed an increase in the amount of [1-^{13}C]lactate in inflamed paws (median, mean lactate-to-pyruvate ratio ±SD = 0.50, 0.52±0.16) versus control paws (0.27, 0.32±0.11, $p<0.03$). The ratio of [1-^{13}C]lactate-to-total carbon-13 was also significantly increased in the inflamed paw. These results suggest that hyperpolarized ^{13}C-labeled pyruvate and subsequent conversion to lactate may serve as an imaging biomarker for the presence of inflammatory arthritis. Eventually, this work may translate for application to autoimmune disorders such as rheumatoid arthritis.

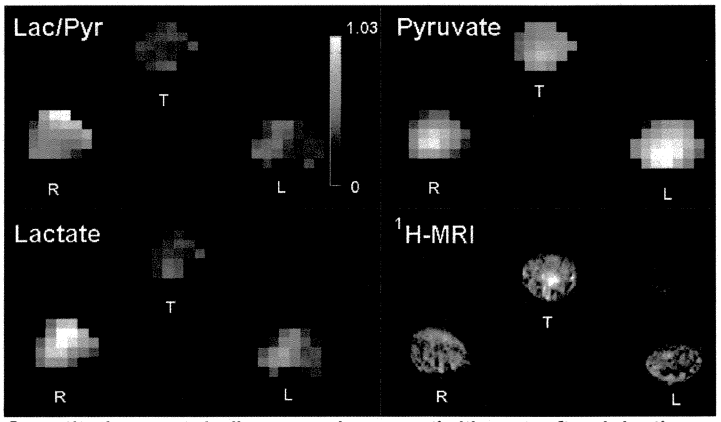

Quantitative metabolic maps in an arthritic rat after injection of hyperpolarized ^{13}C-pyruvate show increased lactate production in the arthritic right paw as measured by the lactate-to-pyruvate ratio (Lac/Pyr). The grayscale bar indicates relative levels of Lac/Pyr. White color is the maximum signal intensity for ^{13}C-pyruvate = 1485 au, ^{13}C-lactate = 674 au, and Lac/Pyr = 1.03. ^{1}H-MRI shows soft tissue swelling in the arthritic right (R) paw in comparison to the control left (L) paw. T=tail, au=arbitrary units.

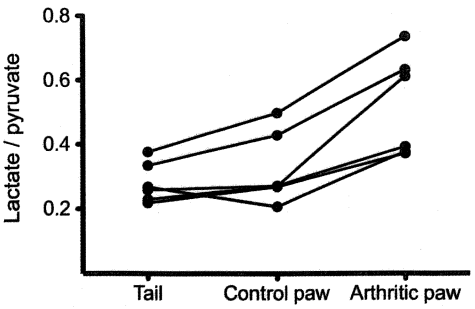

Measured lactate-to-pyruvate ratios in n = 6 arthritic rats. A 65% increase in the mean lactate-to-pyruvate ratio (SD = 33%, range = 38-126%) was observed in the arthritic hind paw compared to the control hind paw on the opposite side. Measurements performed 20 s post bolus injection of 0.5 ml of 80 mM hyperpolarized ^{13}C-pyruvate.

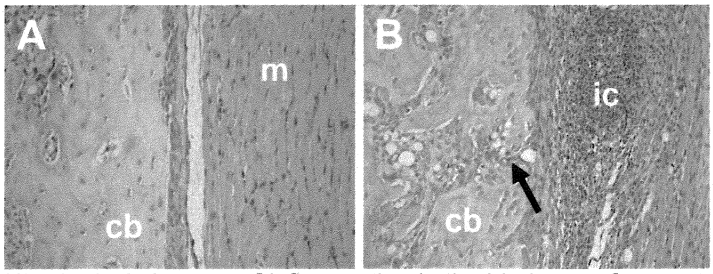

Histological changes of inflammation in the hind paw of one rat seven days after induction of arthritis. (A) Microscopic inspection at 20x magnification shows normal tissue architecture in the cortical bone (cb) and muscle (m) for the control left paw. (B) Arthritic changes in the right paw include accumulation of inflammatory cells (ic) in muscle and periostitis with bone erosion (arrow).

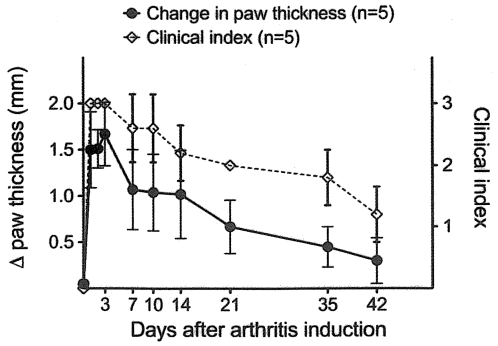

Clinical measures of paw inflammation. Data points show changes in paw thickness (thickness of arthritic right subtracted by control left paw) and clinical index scores (see methods for severity of scoring) in the complete Freund's adjuvant rat model of arthritis. Brackets depict SD.

Imaging metabolism of hyperpolarized [1-^{13}C]pyruvate using multi-band frequency encoding

Cornelius von Morze, Galen Reed, Robert Bok, Peter Shin, Peder EZ Larson, Simon Hu, Daniel B Vigneron

Introduction- Applications of hyperpolarized ^{13}C MR technology require pulse sequences capable of imaging multiple compounds at once (e.g. MRSI), in order to track the metabolism of hyperpolarized substrates *in vivo* (1-3). We describe a robust new approach using frequency encoding (FE) of a single echo for both localization and spectral resolution of hyperpolarized ^{13}C compounds that are widely separated by chemical shift.

Theory- In MRSI, spin frequency is modulated by gradients and chemical shift δ. If the min. separation $\Delta\delta_{min}$ among species exceeds the gradient bandwidth (BW), then unique modulation occurs for all species at all locations, allowing determination of all spectral-spatial components by FE. During reconstruction, metabolite images are shifted to their true locations. Larger $\Delta\delta_{min}$ in ^{13}C studies vs. ^{1}H (and narrow linewidth) allows higher spatial resolution, pixel BW, and imaging speed. For example, brain ^{1}H MRSI may require 0.2 ppm resolution (choline-creatine), while ^{13}C pyruvate-alanine requires only 5.7 ppm. Therefore, for eight voxels across 4 cm, misregistration due to 0.1 ppm inhomogeneity is 20 mm for ^{1}H vs. just 0.7 mm for ^{13}C, and scan time is also 7x as fast.

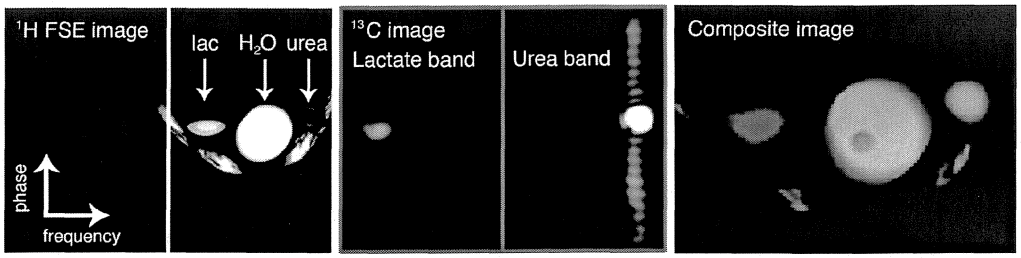

Fig 1. Separation of ^{13}C lactate and urea images by multi-band freq. encoding

Methods- Distribution and conversion of hyperpolarized pyruvate to lactate and alanine was imaged in two TRAMP mice at 3T, using a bSSFP GRE sequence (32-pt quad-band readout over 0.74 kHz). Mice were injected with 350 μL pyr (80 mM, pH ~ 7.5) over 12 sec. Eight axial slices were acquired over 3.6 sec at 35 sec. Other params: TE / TR = 26.5ms / 53ms, spatial resolution= 5mm isotropic. Data was post-processed to correct some small misregistration of the RF pulse profiles. A small pyr hydrate signal contaminating the ala and lac bands was removed using knowledge of the pyr signal to estimate a minimum pyr hydrate signal (.05 x pyr, based on previous studies).

Results- Applying constant shifts on the sub-images resulted in excellent co-registration of all image sets. In one TRAMP bearing a large tumor (d_{max}= 1.4cm), a region of high lac signal corresponded well to the tumor region. In the prostatic region of the other TRAMP, subtle imaging changes (d_{max}= 4mm) were accompanied by high pyr uptake and high lac. These hyperintensities were detected in the region surrounding and just superior to the urethra, the site of early tumor growth in TRAMP mice (4). In fact, imaging at nine days showed additional tumor growth around this region and engorgement of the seminal vesicles caused by tumor.

Discussion- We have demonstrated a robust new method for imaging of multiple ^{13}C compounds that are widely separated in chemical shift, and demonstrated its application for imaging hyperpolarized [1-^{13}C]pyruvate and its metabolic products in TRAMP mice.

References- 1. Golman. PNAS 2003. 2. Chen. MRM 2007. 3. Mayer. MRM 2006. 4. Degrassi. Prostate 2007.

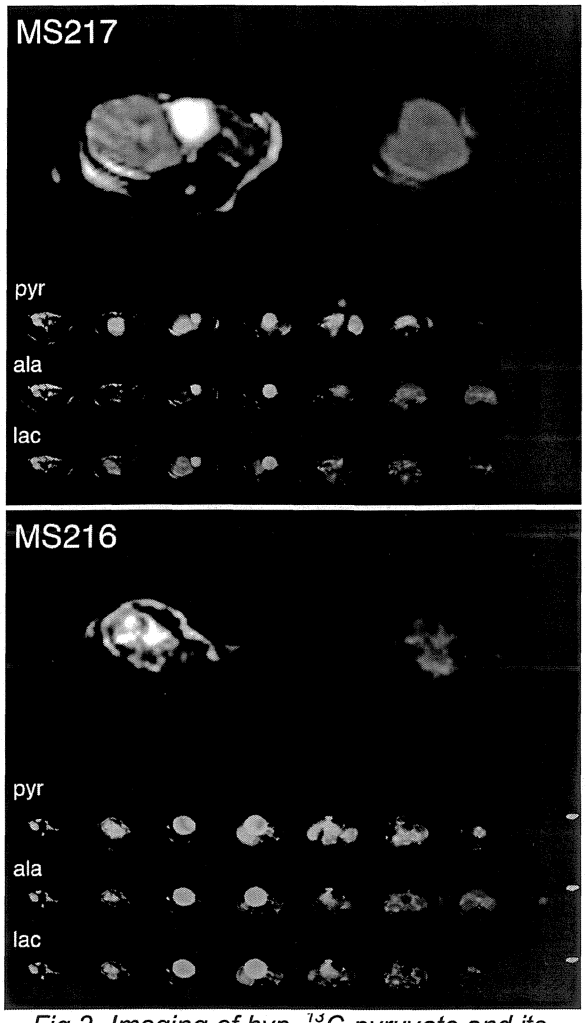

Fig 2. Imaging of hyp. ^{13}C-pyruvate and its metabolic products in 2 TRAMP mice.

Liver Fat and Water MR T2 Values at 3T and Dependence Upon Steatosis Level

Andrew Gilman, Aliya Qayyum, Michelle Nystrom, Susan M. Noworolski

Introduction

Magnetic resonance spectroscopy (MRS) has been shown to be an accurate method of measuring the fat fraction of the liver. Conventionally, when measuring liver fat with MRS, the T2 decay time is assumed to be constant across individuals. The purpose of this study was to measure the liver $T2_{fat}$ and $T2_{water}$ at 3T and to determine if there is a dependence of the T2 values on steatosis level in subjects with and without non-alcoholic fatty liver disease (NAFLD).

Methods

Twelve NAFLD patients and 2 healthy volunteers underwent 3T liver MRI/MRS exams including multiple-TE (3-5 TEs of: 20, 30, 38, 50, and 85 ms) MRS sequences using PRESS (n=4), STEAM (n=2), or both (n=8) methods. An 8cc voxel, placed to avoid vessels, was scanned with no water suppression, TR=2500ms, and 8 acquisitions. The $T2_{fat}$ and $T2_{water}$ were determined by fitting a mono-exponential decay curve. For subjects with both PRESS and STEAM sequences, the average of the two T2s for each technique was used to provide single data points per subject. The fat fraction (Fat/(Fat+Water)) was determined from the peak areas of the CH_2 peak at 1.3ppm and of the water peak in motion corrected MRS spectra either acquired at TE=30 ms or adjusted to a TE of 30ms. Descriptive statistics were obtained and the $T2_{fat}$ and $T2_{water}$ compared using t-tests. Linear regression was used to determine differences between PRESS and STEAM techniques and the dependence of T2 on MRS fat fraction.

Results

For the 8 subjects with both PRESS and STEAM sequences, linear regression showed no difference between PRESS and STEAM in their calculation of liver fat fraction with a slope of 1.00, an intercept of 0.00 and an R^2 of 0.99, confirming that these data are comparable. The $T2_{fat}$ and $T2_{water}$ are very different overall: $T2_{fat}$ = 64±8.8 ms > $T2_{water}$= 26±2.9 ms, $p<10^{-9}$. A linear regression demonstrated that $T2_{fat}$ increased ($p<0.05$) and $T2_{water}$ decreased ($p<0.02$) with an increasing fat fraction across the subjects (Figure 1).

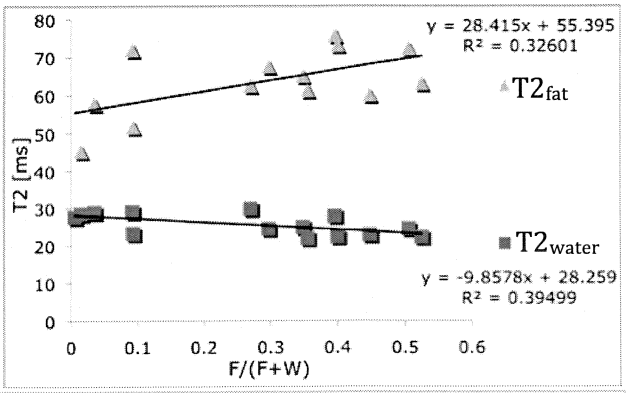

Figure 1 - T2 vs. Liver Fat Fraction [F/(F+W)] at TE=30ms.

Discussion

The presence of significant differences between liver $T2_{fat}$ and $T2_{water}$ and among individuals with varying fat fractions suggests that measured fat fraction is very dependent upon both measurement technique and disease state. T2 dependence on fat fraction may be attributed to the increase in intracellular fat droplets (which may potentially increase the $T2_{fat}$) and this increase in fat droplets causing the cells to swell, shrinking the intracellular and extracellular spaces, thus potentially shortening the $T2_{water}$. Limitations of this study include the small number of subjects, the incomplete range of fat fractions in this study, the lower signal to noise of the fat measured in the healthy subjects (all S/N > 10:1), and the presence and impact of other liver disease beyond steatosis not being addressed in this small population. Future MRS measurements of the liver should measure the $T2_{fat}$ and $T2_{water}$ individually or account for the individual fat fraction when estimating $T2_{fat}$ or $T2_{water}$.

Authors: David M Naeger, Charles Higgins, Teresa De Marco, Stefano Muzzarelli, Karen Ordovas

Title: Border Zone Delayed Contrast Enhancement in Hypertrophic Cardiomyopathy: Comparison to Occlusive Myocardial Infarctions

Abstract:

Purpose: Delayed contrast enhancement (DCE) in occlusive myocardial infarction is a heterogeneous process, often demonstrating an intense central core and a less intense peripheral rim, termed the "border zone". Clinical studies have shown an independent association between the volume of border zone and arrhythmias. Hypertrophic cardiomyopathy (HCM) is a disease associated with fatal arrhythmias and that can present with DCE, yet no study has specifically measured the volume of border zone in DCE-positive HCM patients.

Materials and Methods: We retrospectively reviewed all HCM and occlusive myocardial infarction (MI) cases evaluated by cardiac MR in the last 10 years. Only studies with short-axis cine and double inversion recovery DCE sequences were included; clinical records were reviewed for inclusion criteria. Nineteen DCE-positive HCM subjects, 17 with asymmetric septal and 2 with symmetric HCM, and twenty three MI subjects were included. Infarcts were 61% transmural and 39% subendocardial. Segment image analysis software (Medviso AB, Sweden) was used to identify "border zone" and "central core" regions of DCE, defined as signal intensity 2-3 standard deviations (SD) and >3 SD above a remote unaffected region of myocardium, respectively. Comparisons were made using the Wilcoxon rank sum test.

Results: Total volume of DCE was not statistically significantly different between HCM (median 13 mL [Interquartile range 5-23 mL]) and MI (19 mL [6-36]) subjects, (p=0.22). The volume of border zone, however, was larger in HCM (8 ml [4-15]) versus MI (5 mL [3-7]) subjects, (p=0.036). Of the total DCE in each subject, the median percent that was border zone was 67% (IQR 50-80%) in HCM versus 26% (17-37.5%) in MI (p=<0.001). In the HCM subjects, there was a trend towards more border zone in those with more LV mass (p=0.055), an association not seen with the central core (p=0.16).

Conclusion: Significantly more border zone, arrhythmogenic regions of delayed contrast enhancement, is seen in HCM compared to MI subjects. The association between border zone and arrhythmias should be evaluated in a longitudinal study of HCM patients, given arrhythmias are a frequent cause of death in HCM.

Clinical relevance : Border zone delayed-enhancement is overrepresented in hypertrophic cardiomyopathy vs. myocardial infarctions, and may prove to be the arrythmogenic substrate causing fatal arrhythmias.

Reducing Patient Radiation Exposure During CT-Guided Injections for Spinal Pain

TM Shepherd MD/PhD, CP Hess MD/PhD, CT Chin MD, RG Gould ScD, WP Dillon MD

Purpose: Computed tomography (CT) guidance improves the accuracy and specificity of needle placement for steroid injections to treat spinal pain, a common medical problem with significant costs to society. However, there is increasing concern in the medical community and general public regarding the harmful effects of medical radiation exposure. The UCSF Neuroradiology section recently took steps to reduce patient radiation exposure during CT-guided spinal injections. Retrospective comparison of dose reports before and after these changes were made demonstrate a clinically significant reduction to patient radiation dose.

Methods: In March 2010, the mA settings for almost all image acquisitions during CT-guided spinal injections were broadly reduced. Data then were collected from PACS images, radiology and dose reports for 50 consecutive patients. Comparison data were obtained retrospectively from 50 consecutive patients in 2009 before these changes were implemented. Patient data included sex, age, presence of spinal hardware, number of sites & spinal levels injected, types of injections (e.g. selective nerve root block) and the performing physician. CT acquisition data included the image method (axial vs helical), number of imaging series obtained, mA settings, range and dose-length-product (DLP) for different phases of the procedure (scout, needle placement and contrast verification phases). Data from 2009 and 2010 were compared with paired t-tests or ANOVA with post hoc Tukey tests when appropriate.

Results: Image quality from reduced mA settings (below) did not affect technical success of the procedure or patient-reported immediate pain relief outcomes. Total DLP per procedure decreased 86% from 1458±1022 in 2009 to 199±101 mGy-cm in 2010 after the above changes were implemented ($P<0.05$). In 2010, the effective dose per cervical or lumbar spine injection was reduced to 1.05 and 3.27 mSv respectively ($P<0.05$). These changes appeared most dependent on 82% and 95% reductions to the mA settings and total DLP respectively for image guidance obtained as the injection needle was advanced ($P<0.05$); the radiation contribution from this phase of the procedure dropped from 57% to only 20% in 2010. The variability in dose per procedure for 5 individual operators also decreased from 46% in 2009 to 18% in 2010 when the range for mean total DLP was 165-259 mGy-cm.

Conclusion: Reducing the acquisition mA for different phases of the CT-guided spinal injection procedure reduced patient radiation by more than 85% without affecting the technical success of the procedure. Operator-specific variability in patient dose per procedure also was greatly reduced. This approach should be valid for reducing patient radiation in other CT-guided procedures. These data also identified several additional directions for further dose reduction.

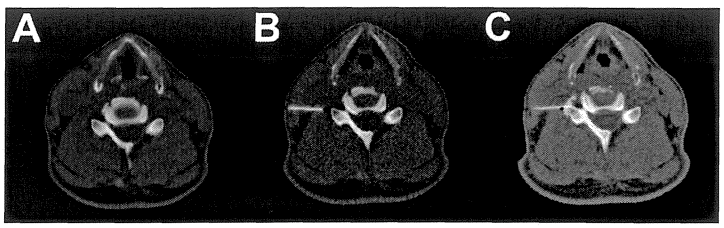

Sample images from the scout (A), needle advance (B) and contrast verification (C) phases of a recent CT-guided right C6 nerve root block. The mA settings were 29, 10 and 20 mA respectively. The total effective dose for this procedure was *only* 0.17 mSv.

Poster Presentations

N-Acetylaspartate Levels in the Brain Reward System Discriminate Smoking and Non-smoking Alcohol Dependent Individuals during Early Abstinence

T.C. Durazzo, S. Gazdzinski, A. Mon, J. Wang, D.J. Meyerhoff

Background: Neuroimaging studies have shown that chronic cigarette smoking in alcohol dependence is associated with increased regional abnormalities of metabolite markers of cerebral neuronal integrity[1,2]. Neurobiological abnormalities in the brain reward system (BRS) are implicated in the development and maintenance of all forms of addictive disorders. Components of the BRS include the dorsolateral prefrontal cortex (DLPFC), anterior cingulate cortex (ACC), insula, cerebellar vermis and corona radiata. Our previous ^{1}H spectroscopic imaging studies investigated the effects of chronic smoking on regional brain metabolites in alcohol dependence examined concentrations at the lobar level (e.g., total frontal gray matter, frontal white matter). Consequently, it is unknown if the observed greater regional metabolite abnormalities in alcohol-dependent smokers are apparent in the BRS. This study measured N-acetylaspartate concentrations (NAA; surrogate marker of neuronal integrity) in multiple components of the BRS in smoking and non-smoking alcohol dependent individuals (ALC). We predicted that smoking ALC individuals demonstrate lower levels of NAA in the BRS than both non-smoking ALC and controls.

Methods: Alcohol dependent participants (n = 45; 3 females) were recruited primarily from the San Francisco VA Medical Center substance abuse clinics. Light-drinking, non-smoking controls (n = 26) were locally recruited. After 35 ± 8 days of abstinence non-smoking ALC (nsALC: n = 21) and smoking ALC (sALC; n = 24) completed 1.5T ^{1}H magnetic resonance spectroscopic imaging studies (MRSI), yielding regional gray and white matter concentrations of NAA and other metabolites. MRSI spatial concentration maps were co-aligned with corresponding brain structural MRI. The following regions of interest were manually segmented: dorsolateral prefrontal cortex, anterior cingulate cortex, insula, cerebellar vermis, superior corona radiata. MRSI voxels were extracted from the above regions of interest and average NAA concentration was calculated for each region. NAA levels in the BRS were compared among groups with the generalized linear model and pairwise t-tests.

Results: Smoking ALC demonstrated lower NAA ($p < .05$; corrected for multiple comparisons) than controls and non-smoking ALC in the DLPFC, insula, cerebellar vermis, superior corona radiata (see Figures 1-3). sALC showed lower ACC NAA than nsALC. There were no differences between nsALC and controls in any region. The regional NAA differences between sALC and nsALC were not mediated alcohol consumption or psychiatric and medical comorbidities.

FIGURE 1

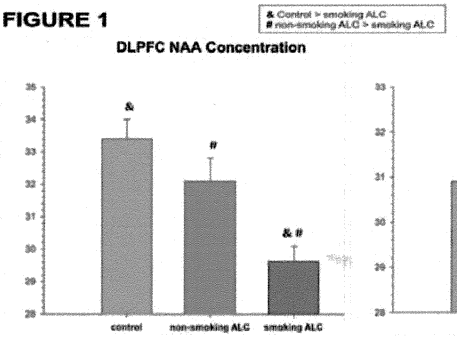

FIGURE 2

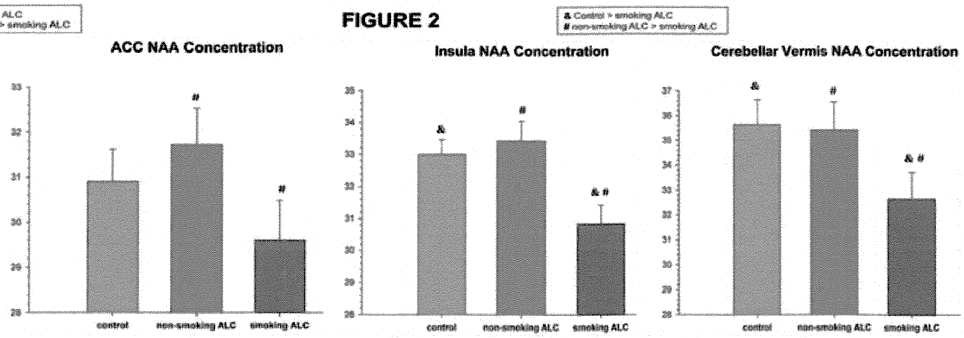

FIGURE 3

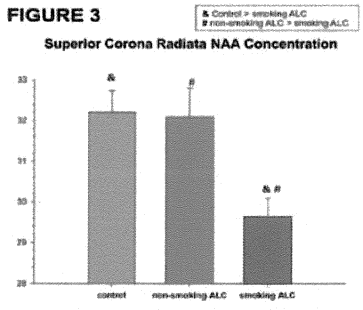

Conclusions: The significantly lower NAA concentration in sALC relative to both nsALC and controls suggest further compromise of neuronal integrity in multiple components of the BRS in sALC. This extends our previous spectroscopic imaging findings[1,2] by indentifying specific regions of the BRS where sALC demonstrated significantly lower levels of NAA than nsALC. Despite high levels of alcohol consumption and the presence of medical and psychiatric comorbidities, nsALC NAA levels were not significantly different from controls in any region. The findings in smoking ALC may reflect the influence of premorbid factors and/or additional direct or indirect insult to brain neurobiology secondary to the noxious compounds contained in cigarette smoke.

References

1) Durazzo et al. (2004), ACER, 28, 1849-1860; 2) Durazzo et al. (2006), ACER, 30, 539-551.

Comparison of glioma sub-populations using in-vivo ADC values and ex-vivo ^{1}H HR-MAS spectroscopy

A. Elkhaled[1], L. Jalbert[1], H. Yoshihara[1], G Bourne[1], C. Cloyd[1,2], J. Phillips[4], S. Cha[1], S.M. Chang[3], J. Kurhanewicz[1,5], R. Srinivasan[1]and S.J. Nelson[1,5]

[1]Department of Radiology and Biomedical Imaging [2]School of Pharmacy,
[3]Department of Neurological Surgery, [4]Department of Pathology
San Francisco [5]Department of Bioengineering and Therapeutic Sciences
University of California, San Francisco

This project compares ex vivo metabolic, pathologic and in vivo ADC parameters for tissue samples derived from patients with gliomas of varying grade and recurrence status. Patients diagnosed with new or recurrent WHO grade IV and recurrent WHO grade II glioma (N=43,29,54) received a pre-surgical MR examination, including ^{1}H spectroscopy (MRSI), diffusion-weighted imaging (DWI), and perfusion-weighted imaging. Automated algorithms generated maps of the choline-to-N-acetyl-aspartate index (CNI) and apparent diffusion coefficient (ADC), along with perfusion curves. Regions of suspected tumor were identified from elevated CNI values, low ADC values, or elevated perfusion peak height/reduced recovery and were designated as targets for tissue sampling using surgical navigation software. Frozen tissue samples were loaded into a 35µL Varian rotor with TSP and ^{1}H HR-MAS spectroscopy was performed at 11.7 Tesla, 1° C, 2250Hz spin rate in a 4mm gHZ nanoprobe using a 500MHz Varian INOVA spectrometer. A 1D Carr-Purcell-Meiboom-Gill sequence was acquired with TR/TE=4s/144ms. The Electronic Reference To access In-vivo Concentrations (ERETIC) method provided an external standard for quantification[1]. Post-processing of the ex vivo spectra utilized jMRUI and a customized HR-QUEST fitting algorithm to measure metabolite concentrations[2]. Metabolite concentrations with < 10% Cramer-Rao error bounds were analyzed using the Wilcoxon ranked-sum test and relevant correlations evaluated with the Spearman rank order test.

Results:

A comparison of the metabolite levels in samples from the patients with newly diagnosed (ND) and recurrent grade IV glioma revealed no significant differences. Preliminary analysis of the pathologic data for the ND and recurrent grade IV samples suggested that increased tumor cellularity was associated with higher MIB-1 indices .The ND samples with increased tumor cellularity had higher total[Cho]/[Cre]. Samples from patients with recurrent low-grade glioma were separated according to whether histological analysis indicated that they had upgraded at the time of recurrence to grade III (Upgraded, N=21) or remained grade II (Non-Upgraded, N=21). As is shown in Fig. 1, both non-upgraded and upgraded samples demonstrated a statistically significant elevation in *myo*-inositol (P<0.00001/0.0002) and creatine (P=0.0003/0.003), when compared with recurrent grade IV samples. Total choline [free choline + phosphocholine (PC) + glycerophosphocholine (GPC)] was higher in the upgraded samples compared to grade IV samples (P=0.005) and the in-vivo nADC increased with decreasing grade (rec. IV vs. III, P=0.02; rec. IV vs. II, P=0.002). The [*myo*-I]/total[Cho] ratio was highly significant in distinguishing non-upgraded glioma from all other sub-classifications of glioma(II vs. rec./ND/upgraded, P=0.001/4x10^{-7}/3x10^{-4})

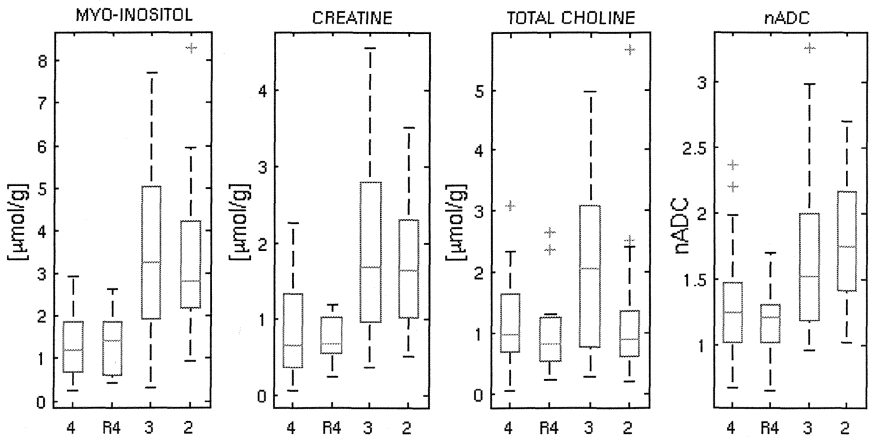

Figure 1: Comparison of parameters according to tumor grade and recurrence status:

Discussion: Newly diagnosed grade IV gliomas were metabolically indistinguishable from their recurrent counterparts despite the disparity in treatment. The observed differences in myo-inositol and total choline suggest that these parameters may also have clinical utility. One possible application for the use of the ratio of [*myo*-I]/total[Cho] [3] is in the detection of characteristically high-grade regions within low-grade glioma. The in-vivo data confirmed previous reports concerning the relationship between ADC values and tumor grade[4].

References: [1] Albers et al. (2009). Magn Reson Med 61(3): 525-32. [2] Swanson et al. (2008). Srinivasan (ISMRM 2009) [3] K. Kono et. al.(2001), [4] AJNR Am J(22)981-8

This study was supported by the NIH Brain Tumor SPORE P50 CA097257 and NIH PO1 CA118816 Grants

Microstructural Correlations of White Matter Tracts in the Human Brain

Sara LaHue[1], Michael Wahl[1], Yi-Ou Li[1], Joshua Ng[1], Shelly Cooper[1], Elliott Sherr[2], Pratik Mukherjee[1]
[1]Department of Radiology & Biomedical Imaging, University of California, San Francisco [2]Department of Neurology, University of California, San Francisco, CA

The purpose of this study is to examine whether specific patterns of correlation exist between DTI parameters across white matter tracts in the normal adult human brain, and to see whether the strength of these correlations might reflect phylogenetic and functional relationships between tracts. We performed quantitative DTI fiber tracking on 44 healthy young adults (24 men, mean age 30.8 ± 7.8). We obtained tract-based measurements of mean FA, mean diffusivity (MD), axial diffusivity (AD), and radial diffusivity (RD) from six homologous (left-right) tract pairs: four neocortical association pathways (arcuate fasciculi, inferior fronto-occipital fasciculi, inferior longitudinal fasciculi, and uncinate fasciculi), one limbic association pathway (dorsal cingulum bundles) and one cortical-subcortical projection pathway (corticospinal tracts). A correlation matrix was generated for each of the four DTI parameters, which shows that there are significant correlations of DTI parameters between tracts, as well as significant variations in correlation strengths. Many of the strongest correlations are between homologous tracts, though the degree of coupling varies. However, some non-homologous tracts are more strongly correlated. Tracts with the greatest known hemispheric asymmetry, such as the arcuate fasciculi and dorsal cingulum bundles, had the weakest left-right correlation. Finally, we generate a data-driven agglomerative hierarchical clustering with multiscale bootstrapping to asses the statistical significance of the tract groupings based on pairwise FA correlations (Figure 1). This demonstrates that neocortical association pathways tend to group separately from the limbic pathways, and the projection pathways of the left and right corticospinal tracts comprise the most distant cluster with high confidence ($p<0.01$). As a result, the statistical clustering of tracts appears to reflect known distinctions between white matter pathways. These groupings may be best measured by FA, which manifests the greatest variation in correlation strengths. Better understanding of microstructural associations between pathways may aid in the investigation of neurological disorders, such as neurodegeneration and brain injury.

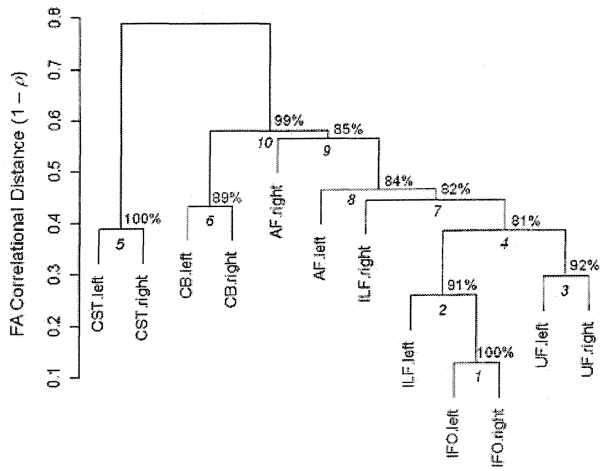

Figure 1. Dendrogram representing hierarchical clustering of FA correlational distances, where distance is measured as 1-ρ and ρ is the Spearman rank correlation coefficient. The number above the linkage signifies the statistical confidence level for that cluster. The italicized edge number is below each branch point and indicates the order in which the tracts were linked by the hierarchical clustering algorithm.

Tract-Based Spatial Statistics Reveals Widespread Microstructural White Matter Disruption within Two Weeks of Mild Traumatic Brain Injury

Authors: Fan-pei Gloria Yang, Ph.D., Christopher Nguyen, B.S., Hana A. Lee, M.P.H., Sara C. LaHue, B.A., Shelly R. Cooper, B.A., Jamshid Ghajar, M.D., Ph.D., Geoffrey T. Manley, M.D., Ph.D., Pratik Mukherjee, M.D., Ph.D.

Introduction

Two recent diffusion tensor imaging (DTI) studies have found conflicting results with regard to early white matter microstructural changes after mild traumatic brain injury (TBI). Lipton et al. (2009) found 15 clusters of voxels with significantly *reduced* fractional anisotropy (FA) in the patients versus the controls. In contradistinction, Mayer et al. (2010) found significantly *increased* FA in patients versus controls. In the present study, we examine microstructural white matter changes within the first two weeks after mild TBI with loss of consciousness and post-traumatic amnesia using 3T DTI with tract-based spatial statistics (TBSS), a widely-used voxel-based method which is specifically designed for atlas-based diffusion tensor analysis.

Methods

Thirty-one adult patients (ages 22-58) with a single episode of mild TBI (Glasgow Coma Scale 13-15), including loss of consciousness (not > 30 minutes) and post-traumatic amnesia (not > 24 hours), were scanned within14 days of trauma on a 3T scanner with 8-channel head coil. Eighteen matched healthy controls were also scanned. The DTI data were collected using a spin echo single-shot EPI sequence with 55 diffusion-encoding directions isotropically distributed over the surface of a sphere with electrostatic repulsion. Following data preprocessing, the voxel-wise statistic analysis of DTI data was conducted with TBSS. Voxel-wise cross-subject statistical analysis was conducted with group comparison.

Results

Clusters of voxels where FA of mild TBI patients was significantly reduced ($p < 0.05$) compared to controls were observed throughout the white matter of both cerebral hemispheres and both cerebellar hemispheres. Conversely, there were no statistically significant clusters where FA values in patients exceeded those of controls. Lower FAs in patients versus controls were more extensive in the left hemisphere than the right hemisphere. White matter in the parietal lobes exhibited the greatest differences across groups, and white matter structures in the temporal and frontal lobes also showed widespread FA differences.

Conclusion

Tract-based spatial statistics reveal widespread cerebral and cerebellar white matter microstructural disruption, as manifested by *reduced* FA values, during the early phase of mild traumatic brain injury with loss of consciousness and post-traumatic amnesia. This agrees with the findings of Lipton et al. (2009); however, we find much more extensive regions of reduced FA throughout the brain than the former study. Given our findings, diffusion tensor imaging with tract-based spatial statistics may prove useful in classifying mild TBI at an early stage, and future longitudinal studies will determine whether DTI may serve as a prognostic biomarker of persistently impaired neurocognitive function at later stages of injury.

Multivariate Patterns of Brain Perfusion and Deformation-Based Atrophic Changes in Normal Aging.

[1]Michael Ewers, [1]Duygu Tosun, [1]Vince Calhoun, [1]Norbert Schuff, [1]Michael Weiner

[1]Department of Radiology, University of California, San Francisco, CA, USA

[1]VA Medical Center, San Francisco, CA, USA

[2]Department of ECE, University of New Mexico, Albuquerque, NM, USA; The Mind Research Network, Albuquerque, NM, USA

Background: Brain aging is associated with regional tissue loss as well as with diminished brain perfusion. However, to what extent tissue loss and hypoperfusion vary in aging independent of each other or together remains unclear. In particular, a joint decline of both could be associated with strong insults on the brain, potentially indicating increased vulnerability toward AD. In this MRI study, we aimed to determine the pattern of joined regional alterations of brain structure and perfusion in normal aging.

Method: A total of 77 cognitively normal subjects within the age range of 21 to 85 years (mean = 56 yrs, SD = 17.2 yrs) were assessed on a 4T scanner. Continuous arterial spinal labeling (cASL) scans were used to assess brain perfusion and deformation based morphometry (DBM) was applied to T1-weighted scans to assess tissue loss. The linear and quadratic association between age and either DBM or globally normalized brain perfusion was computed by partial least squares analysis (PLS).To directly test the multimodal association between DBM and perfusion changes, parallel independent component analysis (pICA) was applied to those brain regions that showed an association with age in the prior PLS analysis.

Results: One significant latent variable of the bootstrapped PLS showed a linear and quadratic association between age and reduced volume in frontal, parietal and temporal brain regions but increased ventricular volume ($p < 0.005$). For perfusion, higher age was associated with lower temporo-parietal, but higher medial temporal perfusion of the grey matter ($p < 0.005$). Results of the multimodal pICA showed several correlated components between DBM and perfusion. Most significantly, ventricular expansion and reduction in precuneus volume were associated with *increased* perfusion of the hippocampus region ($r = -0.55$, $p < 0.001$, figure 1), possibly as a compensatory response.

Conclusions: The finding of increased perfusion in the medial temporal lobe in association with regional tissue loss is intriguing, because such perfusion changes may indicate a compensatory response of the brain tissue loss in aging. Moreover, as these changes are atypical for AD, the finding might improve the differentiation between normal and pathological aging and ultimately provide a sensitive index to identify incipient AD.

REDUCED GLUTAMATE IN THE ANTERIOR CINGULATE OF RECENTLY DETOXIFIED ALCOHOLICS: A MAGNETIC RESONANCE SPECTROSCOPY STUDY

Anderson Mon, Timothy C. Durazzo, and Dieter J. Meyerhoff

CIND/VAMC and Departments of Radiology and Biomedical Imaging and Psychiatry, UCSF

Micro-dialysis studies reported alterations of the glutamatergic and GABAergic systems in animal models of alcoholism. However, only little is known about the effects of alcohol dependence on glutamate (Glu), GABA or the corresponding neurotransmitter systems in humans. The frontal lobes are particularly susceptible to the deleterious effects of alcohol, and several neuroimaging studies have reported reductions in other metabolite concentrations such as N-acetyl aspartate (NAA, a neuronal marker), creatine- (Cr) and choline-containing compounds (Cho). In this report, we compared between recently detoxified alcoholics and light-drinking controls the concentrations of Glu, GABA, and other metabolites in anterior cingulate cortex (ACC), dorsolateral prefrontal cortex (DLPFC) and posterior-occipital cortex (POC).

MRS data were obtained at 4 Tesla (Bruker/Siemens). Using a single-volume STEAM sequence with TR/TE/TM = 1800/15/12 ms and a modified J-editing MEGA PRESS sequence at TR/TE = 2000/68 ms, we acquired spectra in the ACC, POC and DLPFC of 12 light-drinking controls (LD) and 15 alcohol dependent individuals (ALC) at 9 ± 4 days of abstinence. The data were then processed together with co-aligned structural MR data of tissue and CSF to yield absolute metabolite concentrations (not ratios).

Cross-sectional statistical analyses of ACC metabolites showed a significant Glu decrease in ALC compared to LD (-15%). NAA, Cr and Cho were also reduced, consistent with previous 1.5 Tesla findings in frontal lobe gray matter. Glu reductions in the ACC were similar in smoking and non-smoking ALC. None of the metabolite group differences in the POC and the DLPFC of this sample were significant. In addition, GABA was not significantly different in any of the ROIs. While Glu and NAA concentrations in the ACC were highly positively correlated, the metabolite concentrations did not correlate with any alcohol dose measure. Accounting for differences in age and body mass index between the groups did not affect the results.

The reduced Glu content in the ACC of alcohol dependent individuals is an indication of an altered glutamatergic system, consistent with results of animal studies. The positive correlation between Glu and NAA in the ACC does not appear to support the excitotoxicity theory in alcoholism, but may rather signal reduced glutamatergic viability or irreversible neuronal death. Longitudinal studies are being performed to assess potential reversibility of the Glu reductions with sustained abstinence.

Hippocampal atrophy in young veterans with PTSD and cognitive impairment: a potential link between PTSD and dementia

Linda L. Chao, Kristine Yaffe, Thomas C. Neylan, Johannes C. Rothlind, Dieter J. Meyerhoff, Michael W. Weiner

Background:
We recently reported that older veterans with post-traumatic stress disorder (PTSD) are nearly twice as likely to develop dementia compared to veterans without PTSD (Yaffe et al., 2010). The goal of this study is to examine potential links between these two disorders in a group of younger veterans with and without PTSD. We examined the structural magnetic resonance imaging (MRI) and neuropsychological data of a group of Persian Gulf War veterans with PTSD (mean age: 42 years old).

Methods:
All veterans in the study had PTSD, operationalized as a Clinician Administered PTSD Scale (CAPS) score $\geq$ 40. Research has shown that this indicates a moderate threshold of PTSD symptoms (Weathers et al., 2001). Based on evidence of high sensitivity to early cognitive changes in dementia, specific neuropsychological test scores were selected to define 4 cognitive domains: verbal memory, executive function, language, and visuospatial abilities. Continuous raw scores were used to create dichotomous variables of high or low performance for each cognitive domain. Low cognitive performance in each cognitive domain was operationzlied as a score of at least 1.5 standard deviation below the mean of Persian Gulf veterans without PTSD. Thus defined, 25 veterans with PTSD exhibited cognitive impairments (CI) while 22 veterans with PTSD did not exhibit CI. T1-weighted MRI scans from a 1.5T Siemens Vision scanner, available for 22 of the 25 PTSD+ CI subjects and for 17 of the 22 PTSD+ without CI, were analyzed using automated and semi-automated image processing techniques that produced volumetric measurements of gray matter (GM) and white matter (WM) from the four lobes and the hippocampus.

Results: Veterans with and without CI were similar in age, education, CAPS score, % male, and depressive symptomatology ($p \geq 0.2$ for all). As expected, there were significant group differences in verbal memory ($p < 0.0001$), language ($p = 0.0001$), and visuospatial abilities ($p = 0.01$) domain scores; however there was no significant difference in the executive function domain ($p = 0.71$). There were also significant group differences in hippocampal ($p = 0.02$) and frontal white matter ($p = 0.02$) volumes and a marginal group difference in temporal white matter volume ($p = 0.05$).

Conclusions: Previous studies have reported reduced hippocampal volume in individuals with PTSD (e.g., Bremner et al., 1995). This study shows that hippocampal volume is further reduced in PTSD+ subjects with CI. Because hippocampal atrophy and memory impairment are both risk factors for Alzheimer's disease (AD), this may be a potential link between the two disorders.

Hyperpolarized ^{13}C MR Spectroscopic Imaging for the Detection of Early Response to Treatment with Temozolomide in Brain Tumors

Ilwoo Park[1], Robert Bok[1], Tomoko Ozawa[2], Daniel B. Vigneron[1], C. David James[2], Sabrina Ronen[1], Sarah J. Nelson[1]

[1]Surbeck Laboratory of Advanced Imaging, Department of Radiology and Biomedical Imaging, [2]Brain Tumor Research Center, Department of Neurological Surgery, University of California, San Francisco, CA, United States

Introduction: A recent study has shown that tumor metabolism in brain tumor model can be examined using hyperpolarized ^{13}C MR metabolic imaging [1]. The purpose of this study was to demonstrate the feasibility of using this technique in measuring early response to Temozolomide (TMZ) therapy in a human glioblastoma xenograft in rat brain.
Methods: 20 athymic rats with intracranial implantation of human glioblastoma cells were divided into two groups: one group received an oral administration of 100 mg/kg TMZ (n=10) and the other control group received the vehicle only (n=10). All animals underwent ^{13}C and ^{1}H imaging using a 3T scanner with a custom RF coil before the treatment (D0), at D1 (days from treatment) or D2 and at several subsequent time points. 4 treated and 4 control rats were sacrificed at D2 and the tumor tissue from their brains analyzed. ^{13}C 3D MRSI data [2] were acquired 20 sec after the injection of 2.5 ml (100 mM) hyperpolarized $^{13}C_1$-pyruvate through their tail vein. Lactate over pyruvate ratio (Lac/Pyr) was calculated for the assessment of change in tumor metabolism. Tumor volume was estimated from T1 post-Gd images. After the experiments, rats were sacrificed and their brains resected for immunohistochemical analysis.
Results: Tumor metabolism as measured by Lac/Pyr was altered at D1 for the group treated with TMZ (Fig 1a) but the tumor volume did not show a reduction until D5 to D7 (Fig1b). The percent change in Lac/Pyr from baseline was statistically different between the two groups at D1 and D2, while percent tumor volume was not (Fig1). Figure 2 shows an example of T1 post-Gd images, ^{13}C spectra and Lac/Pyr map from a rat treated with TMZ, indicating dramatic drop in Lac/Pyr at D1 and D2 compared to baseline. Results from immunohistochemical analysis revealed the appearance of rare apoptotic cells from the treated rat sacrificed at D2 (Fig3a), whereas the control rat sacrificed at D2 did not appear to have any apoptotic cells (Fig3b). Greater number of apoptotic cells was observed in the treated rat sacrificed at D7 (Fig3c), coinciding with the start of tumor shrinkage at approximately D7 (Fig1b).
Conclusions: We have demonstrated the feasibility of using hyperpolarized ^{13}C MR imaging to detect early response to treatment with TMZ in a pre-clinical brain tumor model system. Future studies will examine the application of this technology to monitor response to therapy for patients with brain tumors.
References: [1] Park et al. Neuro-Oncology, 2010. [2] Cunningham et al. J Magn Reson, 2007.
Grant support: ITLBIO04-10148, NIH RO1 EB007588.

Figure 1

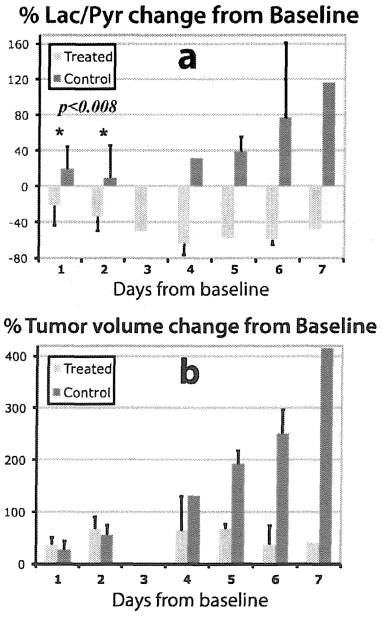

Figure 2

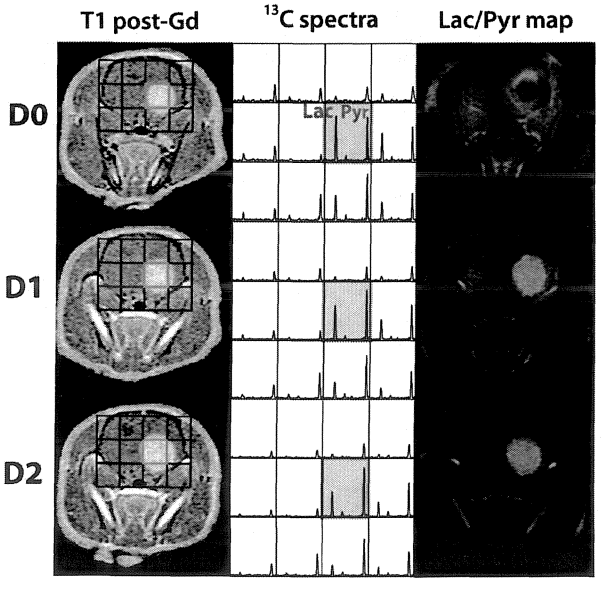

Figure 3

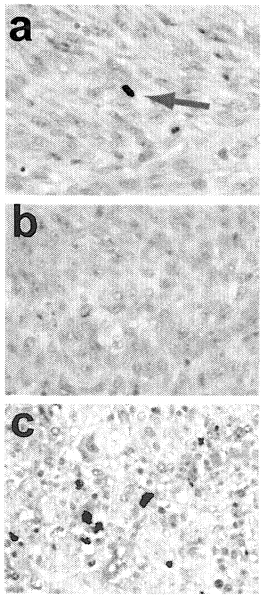

Figure 1 % Lac/Pyr (a) and tumor volume (b) change from baseline in two groups.
Figure 2 An example of radiographic and metabolic changes at D0, D1 and D2 from a TMZ treated rat.
Figure 3 Caspase 3 stained slices from a treated rat at D2 (a), a control rat at D2 (b) and a treated rat at D7 (c).

Metabolic characterization of Recurrent Grade 2 Glioma using Proton HR-MAS Spectroscopy

L. Jalbert[1], A. Elkhaled[1], R. Srinivasan[1], H. Yoshihara[1], G. Bourne[1], C. Cloyd[1,2], S.M. Chang[3], S. Cha[1], J. Kurhanewicz[1,4], and S.J. Nelson[1,4]

[1]Department of Radiology and Biomedical Imaging, UCSF, [2]School of Pharmacy, UCSF [3]Department of Neurological Surgery, UCSF [4]Department of Bioengineering and Therapeutic Sciences, UCSF

Introduction: Proton High Resolution Magic Angle Spectroscopy (^{1}H HR-MAS) is a technique that can predict cell physiology through accurate characterization of tissue metabolism[1]. This study aims to improve our understanding of the malignant transformation of glioma, and differentiate between astrocytoma and oligodendroglioma histological subtypes using ^{1}H HR-MAS. **Methods:** Fifty-four patients who had pathologically confirmed WHO Grade 2 recurrent glioma were included in our study. These patients had received prior treatment with surgical resection and/or radiation and chemotherapy and were enrolled at time of suspected recurrence. **In vivo MR Scans:** Preoperative MR studies were conducted at either 1.5 or 3 Tesla. The scans included 6 directional Diffusion Weighted Imaging (DWI); lactate-edited 3D MRSI localization; and dynamic Perfusion Weighted Imaging (PWI). **Data Analysis:** In house software was used to quantify DWI, MRSI, and PWI parameters. Tissue sample locations were selected based on surgically accessible areas with low ADC, elevated Choline/N-Acetylaspartate index (CNI), or elevated PWI peak height and low recovery. Image guided tissue acquisition was performed using BrainLAB surgical navigation software. Upon surgical excision, the tissue samples were immediately snap frozen in liquid nitrogen and stored at -80°C. 110 tissue samples were collected and 48 samples have been analyzed so far. **Ex vivo ^{1}H HR-MAS**: Tissue samples were placed in a zirconium rotor with 3-(Trimethylsilyl)propionic acid (TSP). Samples were scanned with a 500 MHz multi-nuclear spectrometer. A 1D Carr-Purcell-Meiboom-Gill (CPMG) Sequence was run with TR/TE=4s/144ms. The ERETIC method was utilized for quantification[3]. Post processing was performed using jMRUI and a customized HR-QUEST algorithm to extract metabolite concentrations[5]. Parameter fits with less than 13% Cramer-Rao error estimates were included for analysis with a Wilcoxon rank sum test to assess statistical significance ($p < 0.05$). **Results:** Approximately half of the patients had tumors that were assessed as upgrading to WHO Grade 3. 48 tissue samples were analyzed. Sample choline spectra is shown in Figure 1. Figure 2 shows differences for tumors that were assessed as upgrading at the time of recurrence versus those that did not. Metabolite concentrations that differentiated between oligodendroglioma and astrocytoma histological subtypes are shown in Figure 3. **Conclusions:** The ex vivo ^{1}HR-MAS results from our study suggest that higher PC, GPC, total choline, and glucose concentrations may contribute in identifying low-grade glioma patients whose tumors have become more aggressive. This is vitally important for treatment planning and selection. The results also suggest that ^{1}HR-MAS can reflect differences in the biological parameters associated with different histological subtypes of glial tumors. Future studies will compare the ex vivo data with corresponding in vivo parameters to identify noninvasive parameters that could also assess whether a lesion has upgraded.

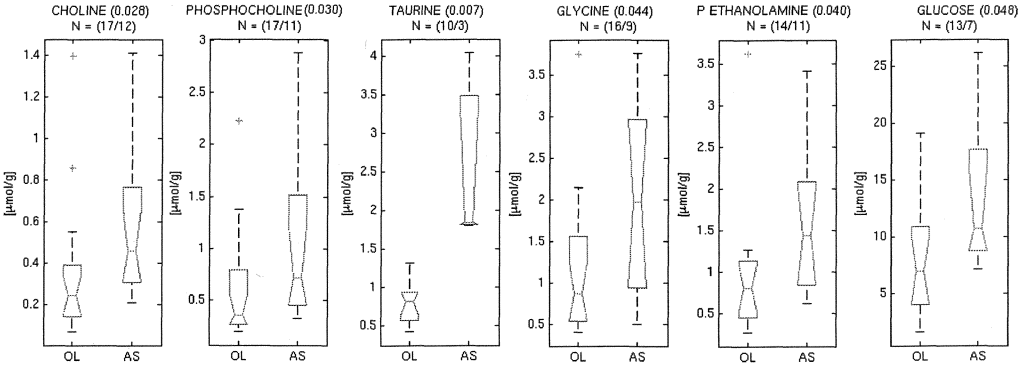

Figure 3. Differences between astrocytoma (AS) and oligodendroglioma (OL) histological subtypes

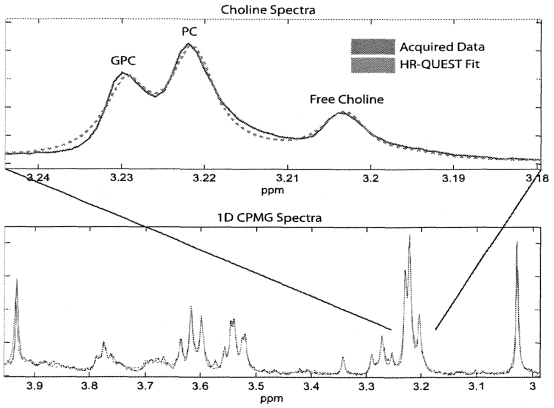

Figure 1. 1D ^{1}H HR-MAS CPMG Spectra of an upgraded astrocytoma

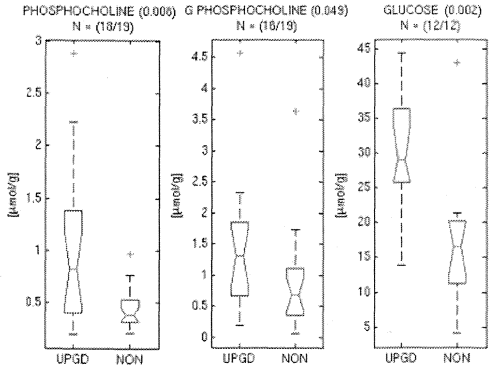

Figure 2. Patients who upgraded from WHO Grade 2 (UPGD) to Grade 3 showed elevated concentrations of phosphocholine, glycerophosphocholine, and glucose

[1] Sitter et al. (2009). PNMR 54(3): 239-254 [2] Righi et al. (2009). NMR Biomed 22(6): 629-37. [3] Albers et al. (2009). Mag Reson Med 61(3): 525-32. [4] Swanson et al. (2008). Magn Reson Med 60(1):33-40[5] Stefan et al. (2009). Meas. Sci. Technol 20(10)

This study was supported by the NIH Brain Tumor SPORE Grant P50CA097257

Can Susceptibility-Weighted Imaging Determine Response to Combined Anti-angiogenic, Cytotoxic, and Radiation Therapy in GBM Patients?

Janine M. Lupo, Emma Essock-Burns, Soonmee Cha, Susan M. Chang, Nicholas Butowski, Sarah J. Nelson
[1]Department of Radiology and Biomedical Imaging, [2]Department of Neurosurgery, and [3]Department of Bioengineering and Therapeutic Sciences, University of California, San Francisco

Introduction: Susceptibility-weighted imaging (SWI) is a powerful tool for high resolution imaging of the vasculature that has been shown to improve the diagnosis of brain neoplasms. Although SWI provides unique and potentially valuable contrast that is not always present on conventional anatomical or perfusion scans, the biological basis behind the hypointensity observed on SWI images within the contrast-enhancing lesion (CEL) that is not the result of hemorrhage, residual blood products, or calcification is still unclear. However, this contrast mechanism is expected to be advantageous both as a predictive biomarker in identifying likely responders to therapy, as well as in assessing treatment effect and response for anti-angiogenic and radiotherapy. The goal of this study is to investigate whether the amount of SWI hypointensity within the post-gadolinium contrast enhancing lesion on the post-surgery, pre-treatment scan can predict response in patients with glioblastoma multiforme (GBM) brain tumors receiving concomitant anti-angiogenic, cytotoxic, and radiation therapy.

Methods: Twenty-five patients were imaged prior to beginning therapy (post-surgical resection) and scanned serially every 2 months while on therapy until progression. In addition to standard clinical MR imaging, high-resolution T2*-weighted SWI was performed on a 3T GE scanner. The SWI images were thresholded within the contrast-enhancing lesion to calculate the volume of SWI-hypointensity (SWI-h) within the enhancement for each patient's pre-treatment scan. Any enhancement that was also present on the pre-contrast T1 images, indicative of acute blood products and therefore always hypointense on SWI, was excluded. Progression-free survival (PFS), from the baseline pre-therapy scan to radiologic progression, and overall survival (OS) were each used to characterize patients into 3 response groups: (1)non-responders (PFS≤6months, OS≤12months), (2)intermediate responders (PFS 6-12months, OS 12-18months), and (3)sustained responders (PFS≥12months, OS≥18months).

Results & Discussion: For both OS and PFS based response categories, the %SWI-h within the CEL was significantly higher in sustained responders than non-responders, suggesting that tumors with a larger extent of damaged vasculature initially are more likely to benefit from a treatment regimen containing an anti-angiogenic agent. Spearman rank correlation coefficients showed good association between %SWI-h with PFS and OS ($p<0.001$), with a greater amount of SWI-h indicating a more favorable prognosis. Adjusting for baseline KPS, age, and extent of resection, multivariate Cox regression analysis showed that %SWI-h was predictive of both PFS and OS (HR=0.961,0.935; $p<0.005$).

Conclusions: These early differences suggest that SWI could be especially advantageous for determining which patients would benefit most from a given therapy and provide clinicians with a tool for identifying the best candidates for diverse therapeutic strategies. Future studies will investigate the patterns of SWI-h immediately prior to progression and incorporate functional imaging changes such as parameters derived from perfusion and diffusion weighted imaging to determine which patients would benefit the most from a given therapy.

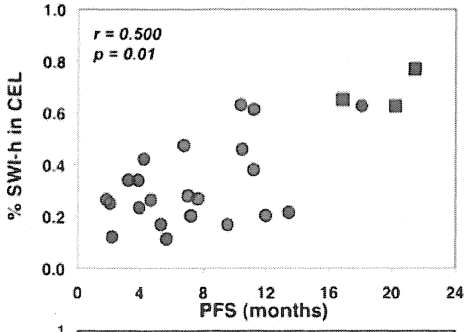

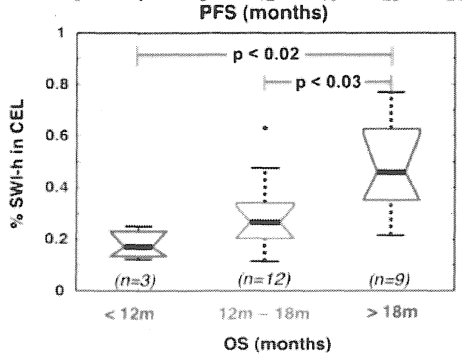

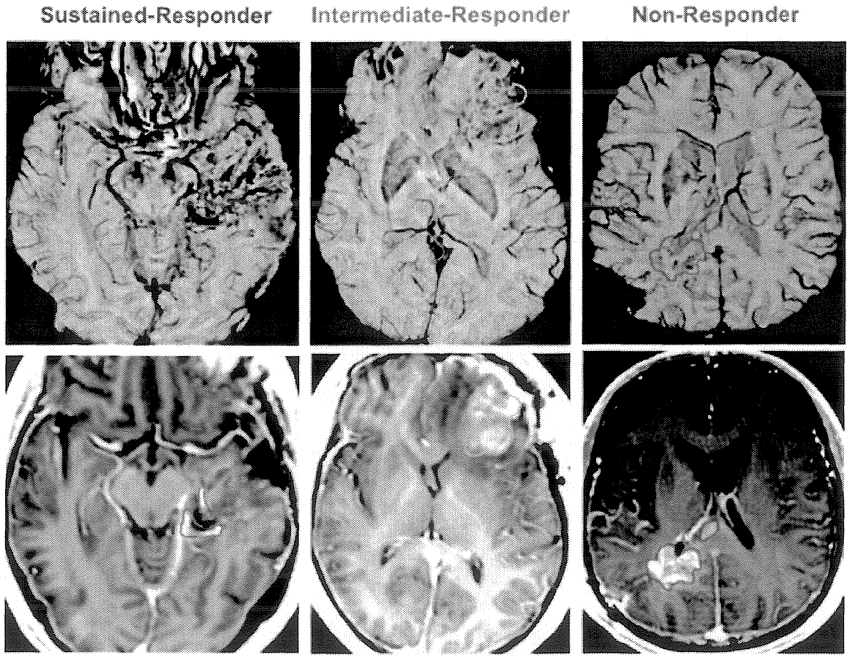

Title: Assessment of Diffusion Parameters at Pre-, Mid- and Post-radiation in Glioblastoma Multiforme Patients Receiving bevacizumab therapy

Authors: Laleh Jalilian, Soonmee Cha, Susan Chang, Nicolas Butowski, Sarah J. Nelson

Intro: Glioblastoma multiforme (GBM) is the most common and most malignant type of glioma. A new class of anti-angiogenic agents targeting vascular endothelial growth factor (VEGF) administered to GBM patients can affect the growth of neoplastic blood vessels and result in the elimination of the contrast-enhancing lesion (CEL) on standard anatomic MR exams. In many cases, it has been observed that although the original CEL volume decreases, new enhancing or non-enhancing regions of tumor appear. Diffusion-weighted Imaging (DWI) is a functional imaging technique that has the potential to become an important adjunct to standard anatomic imaging in the management of GBM patients receiving anti-angiogenic treatments in conjunction with radiation therapy and temozolomide(TMZ). The purpose of this study was to assess changes in DWI parameters at pre-, mid- and post-radiation therapy(RT) in CEL and non-enhancing lesions of postsurgical GBM patients treated with the standard of care RT concurrently with TMZ and bevacizumab.

Methods: 15 newly diagnosed GBM patients treated with surgical resection, radio-, chemo- and bevacizumab therapy were examined. Patients were imaged prior to the beginning of therapy (post surgical resection) and scanned serially at 1 month, 2 months, and every 2 months after therapy initiation on a 3T GE EXCITE scanner with 8- channel phased array receive coil. They were scanned with six directional diffusion tensor echo-planar imaging (EPI) sequence (TR = 7,000 ms, TE = 63 ms, matrix size = 256 x 256, slice thickness = 3 mm, b = 1000 s/mm2, FOV = 220 x 220 mm2, NEX=4). ADC values were obtained from DWI for the following parameters at one and two scans prior to progression: normal appearing white matter (NAWM), contrast-enhancing lesion (CEL), T2 hyperintense lesion (T2ALL), and areas of T2ALL that did not include enhancement (NEL). Ranksum tests compared ADC values of these parameters between scans.

Results: Median nADC values for CEL, T2ALL, and NEL at baseline, 1-month, and 2-month scans are shown in **Figure 1**. There is a significant difference between CEL and T2ALL at baseline ($p < 0.0341$) and at 1-month ($p < 0.0322$) but not between the baseline and 2-month scan ($p < 0.8375$). There was a significant decrease ($p<0.0013$ and $p<0.0019$) in volume of T2ALL and NEL at the 2-month scan from baseline as seen in **Figure 2**.

Conclusion: Bevacizumab therapy in GBM patients may exert a steroid-like effect affecting tumor edema, as demonstrated by decreases in T2ALL and NEL nADC values and volumes. Further investigation will examine whether these early diffusion parameters may serve as early biomarkers for disease progression by relating them to clinical outcome of 6-month progression-free survival.

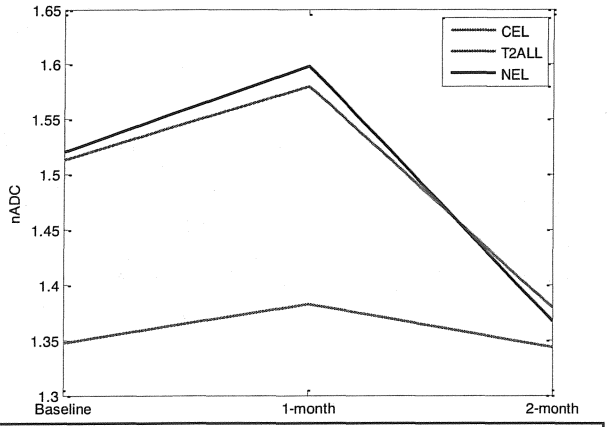

Figure 1. Median nADC at baseline, 1-month, and 2-months cans for CEL, T2ALL, and NEL ROIs.

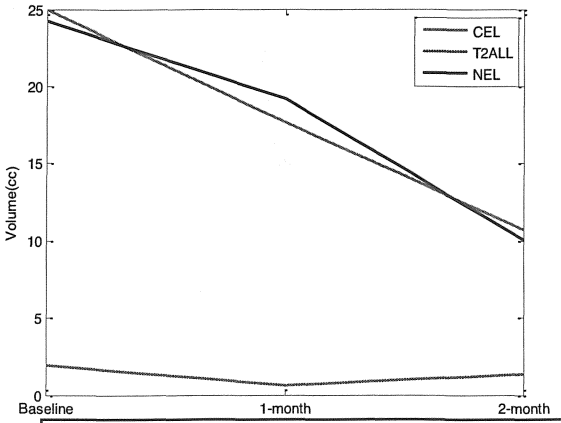

Figure 2. Median volumes at baseline, 1-month, and 2-month scans for CEL, T2ALL and NEL.

In vivo detection of PI3K pathway inhibition by hyperpolarized ^{13}C MRSI at 14.1T in an orthotopic model of GBMs

M. M. Chaumeil[1], I. Park[1], K. Scott[1], T. Ozawa[2], C. D. James[2], J. Kurhanewicz[1], D. B. Vigneron[1], S. J. Nelson[1], S. M. Ronen[1]
[1]Department of Radiology and Biomedical Imaging, [2]Department of Neurological Surgery, UCSF

INTRODUCTION

Glioblastoma (GBM) is the most common and lethal primary malignant brain tumor in humans [1, 2]. One new promising treatment approach aims at targeting the phosphatidylinositol-3-kinase (PI3K) signaling pathway, which is activated in >88% of GBMs [3]. In particular, Everolimus, an inhibitor of the PI3K downstream effector mTOR, is currently in clinical trials. However, the assessment of early response to PI3K/mTOR inhibitors remains a challenge. In this study, our goal was to detect PI3K/mTOR inhibition by Everolimus *in vivo* using hyperpolarized (HP) ^{13}C magnetic resonance spectroscopic imaging (MRSI) in an orthotopic model of GBMs.

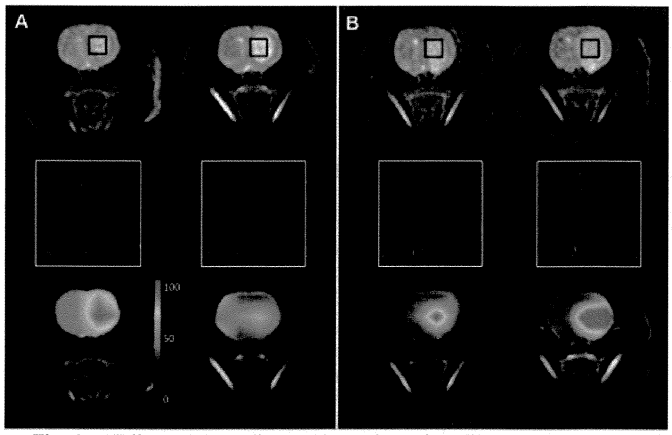

Fig 1 - Effect of Everolimus (A) and carrier (B) treatment on GS-2 orthotopic tumors *(top row) Axial SE image overlaid with tumors voxels (middle row) Corresponding 3D-MRSI lactate spectra and (bottom row) lactate-to-pyruvate ratio maps (normalized to contralateral brain).*

MATERIAL & METHODS

Tumor-bearing animals 5 weeks-old athymic rats (n=9, Harlan, Indianapolis, IN) were included in the study. Animals were anesthetized using ketamine/xylazine and GS-2 cells ($3x10^6$ in 10µL) were injected in the right caudate putamen Approx. 40 days post injection, treated animals received a daily ip injection of Everolimus (n=5, $10mg.kg^{-1}.day^{-1}$ in DMSO) while control animals received the same volume of DMSO (n=4).

MR system & Experimental set-up Experiments were performed on a 3T GE system equipped with a dual-tuned ^1H-^{13}C coil ($Ø_I$=80mm). Animals were anesthetized using isoflurane (1-2% in O_2, 1.5 $L.min^{-1}$) and a 24G catheter was secured in the tail vein of the animal.

MR acquisitions Each animal underwent three MR sessions (day 0 (D0), 2 (D2) and 7 (D7) post treatment initiation). T2-weighted anatomical images were acquired to assess the tumor size and location. [1-^{13}C]-pyruvic acid was hyperpolarized as described previously [4, 5]. After 1 hr, polarized pyruvic acid was rapidly dissolved to obtain a 100mM buffered solution. 3.3±0.3mL of the pyruvate solution was rapidly injected through the iv catheter and a double SE sequence was used to acquire the ^{13}C 3D MRSI data (4x4x5.4mm resolution). Anatomical and ^{13}C 2D-MRSI data were processed using an in-house-developed software.

RESULTS & DISCUSSION

Figure 1 presents data obtained from one treated (A) and one control (B) animal. The left column corresponds to D0 data, the right to D7 data. Axial images (top row) allow assessing the tumor location and size. Magnitude spectra from tumor voxels are displayed in the middle row, showing the decrease/increase in lactate after Everolimus/carrier treatment respectively. Corresponding lactate-to-pyruvate ratio maps normalized to contralateral brain are shown in the bottom row. Figure 2 summarizes results obtained from all animals. No difference in tumor growth was measured between controls and treated at D7. However, the lactate-to-pyruvate ratio was significantly decreased at D7 in treated animals relative to controls (44±22%, p=0.05). Note that the effect of treatment on tumor growth can be seen at latest time points, confirming the drug action.

The drop in lactate-to-pyruvate ratio following Everolimus reported in this study is in line with the findings in treated cells and subcutaneous tumors [6] and likely indicates a decrease in LDH activity in treated tumors, as LDH expression is controlled by the PI3K signaling pathway. Further immunohistochemistry studies are underway to assess the underlying mechanisms. This study demonstrates the value of hyperpolarized ^{13}C MRS for noninvasive monitoring of the effect of PI3K inhibitors.

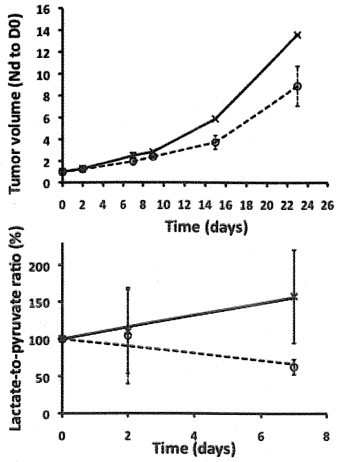

Fig 2 – (A) Tumor volume and (B) lactate-to-pyruvate ratio as calculated from MRSI data as functions of days of treatment. [x/solid lines] controls, [o/dashed lines] treated.

REFERENCES 1- Belda-Iniesta C et al. Clin Transl Oncol (2008) 2- Stupp R et al., Lancet Oncol (2009) 3-Workman P et al., Nat Biotechnol (2006) 4- Albers MJ et al, Cancer Res (2008) 5-Park I et al, Neuro Oncol (2009) 6-Ward C. et al, Cancer Res (2010)

ACKNOWLEDGMENTS This work was supported by NIH grants R21 CA120010-01A1, RO1 CA130819, NIH/NCRR UCSF-CTSI Grant UL1 RR024131-01, UC Discovery grant ITL-BIO04-10148 and UCSF Brain Tumor SPORE CA097257, in conjunction with GE Healthcare.

Comparison of DSC-derived Perfusion Parameters in Response to Conventional Therapy or Concurrent Anti-Angiogenic Therapy in Patients Newly-Diagnosed with GBM

E. Essock-Burns[1,2], Y. Li[1], J. M. Lupo[1], M-Y. Polley[3], N.Butowski[3], S.M. Chang[3], S. Cha[1,3], and S. J. Nelson[1,2,4]

[1]Department of Radiology and Biomedical Imaging, UC San Francisco, [2]Joint Graduate Group in Bioengineering, UC San Francisco/UC Berkeley, [3]Department of Neurological Surgery, UC San Francisco, [4]Department of Bioengineering and Therapeutic Sciences, UC San Francisco

Introduction: The therapy paradigm of glioblastoma multiforme (GBM), a highly malignant and vascularized brain tumor, is shifting from a purely cytotoxic approach to incorporating targeted, "cytostatic" therapy. The standard-of-care for patients with GBM includes combined radio- and cytotoxic (i.e. temozolomide) therapy. Cytostatic anti-angiogenic therapy, thought to normalize the tumor vasculature, has shown improved disease management in recurrent patients. Dynamic Susceptibility Contrast (DSC) Imaging can detect vascular changes following anti-angiogenic therapy. The purpose of this study was to (1) compare early perfusion parameters between patients receiving conventional therapy and patients receiving concurrent anti-angiogenic therapy and (2) assess whether these parameters relate to 6-month progression-free survival (PFS) status.

Methods: Seventy-one patients newly-diagnosed with GBM were imaged serially every two-months on a 3T scanner. Thirty-six patients received conventional therapy (RT + temozolomide) and thirty-five patients received conventional and concurrent anti-angiogenic therapy (RT + temozolomide + PKC inhibitor). Dynamic Susceptibility Contrast Imaging was acquired with a gradient-echo, echo-planar sequence (TE/TR=54/1500ms, flip angle=35°, 24x24cm^2 FOV, 128x128matrix) during the Gadolinium injection. Perfusion parameters, peak height (PH) and percent signal recovery (%REC), were calculated from the dynamic curves to assess blood volume and leakage, respectively. Putative tumor region was defined to include the union of the contrast-enhancing lesion, FLAIR-hyperintensity, and elevated Choline-to-NAA index (Figure 2: pink overlay). The extreme portion of abnormality within this region, defined as 90th-percentile for PH and 25th-percentile for %REC, was identified serially.

Results:

Comparison of Perfusion Changes: By two-months into therapy, patients receiving concurrent anti-angiogenic therapy decreased in PH (Wilcoxon sign-rank, p=.001) from baseline, while patients receiving conventional therapy did not change significantly (Figure 1).

Predicting PFS based on Perfusion: Within the concurrent anti-angiogenic therapy group, patients with PFS greater than 6-months showed a significant increase in %REC within the first two months of treatment (Wilcoxon signrank, p=.008), while patients receiving conventional therapy did not significantly change in percent recovery for either 6-month PFS status group. The %REC at two-months into therapy was further predictive of PFS for patients receiving concurrent anti-angiogenic therapy (Cox regression, p<.009) and was not predictive for patients receiving conventional therapy (p>.7).

Conclusion: This study highlights the utility of perfusion imaging in assessing response to anti-angiogenic therapy, since predictive changes in underlying vasculature were observed prior to evidence of clinical progression. Future validation studies aim to include other anti-angiogenic therapies.

Grant Support: NIH grants (RO1 CA127612-01A1, P01 CA11816) and UC Discovery grant (ITL-BIO04-10148)

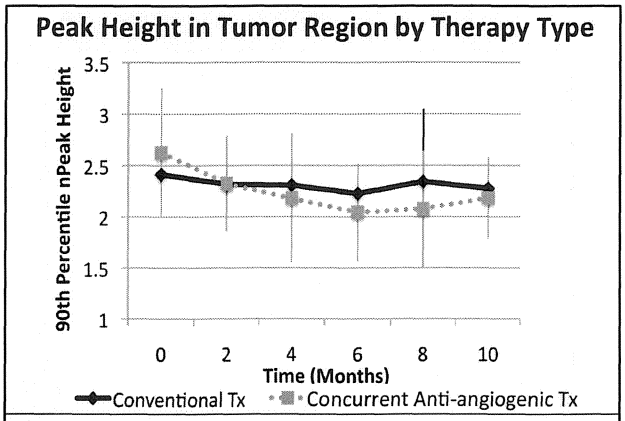

Figure 1. Patients receiving concurrent anti-angiogenic therapy show decrease in vascularization by 2-months, while patients receiving conventional therapy do not.

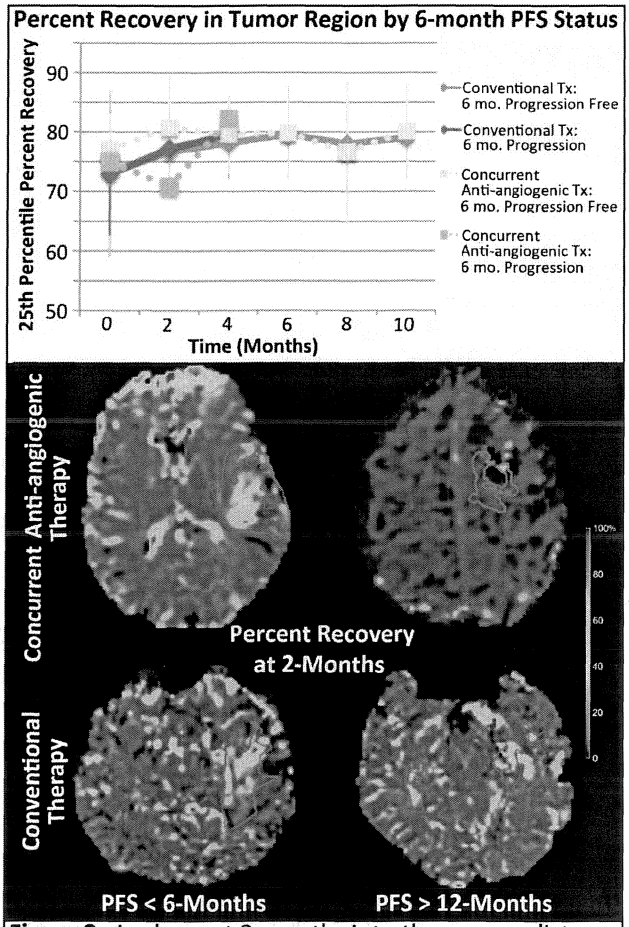

Figure 2. Leakage at 2-months into therapy predicts PFS for patients with concurrent anti-angiogenic therapy and does not for patients with conventional therapy.

Longitudinal MRSI study in newly diagnosed Glioblastoma Multiforme

Yan Li,[1] Janine Lupo,[1] Soonmee Cha,[1] Susan Chang,[2] and Sarah J. Nelson,[1]

[1]Department of Radiology, University of California, San Francisco, CA, United States
[2]Department of Neurological Surgery, University of California, San Francisco, CA, United States

Introduction

Glioblastoma Multiforme (GBM) is the most common and the most malignant type of glioma. The purpose of this study was to assess serial metabolic changes in patients with newly diagnosed GBM, to examine the predictive value of MRS parameters in relation to progression, and to evaluate the importance of such parameters in scans obtained prior to progression.

Methods

A total of eighteen patients with newly diagnosed GBM were studied after surgical resection but prior to RT and chemotherapy, immediately after RT (post-RT) and every 2 months thereafter until tumor progression. The MR data were acquired from either 1.5 T or 3 T GE scanners. The choline to NAA index (CNI) was calculated using an automated regression technique. To evaluate the predictive role of MRSI in progression, the images at the time of progression were aligned to those at the time of pre-progression (Pre-PG) to define the region of new contrast enhancement (CEL) lesion. Figure 1 is an example of New CEL shown in the red box. Volumes of CEL within PRESS box and CNI in CEL were evaluated from the baseline to PG. Wilcoxon rank tests were applied to evaluate the difference between a single time point and progression time point, with a P-value of <0.05 being regarded as significant.

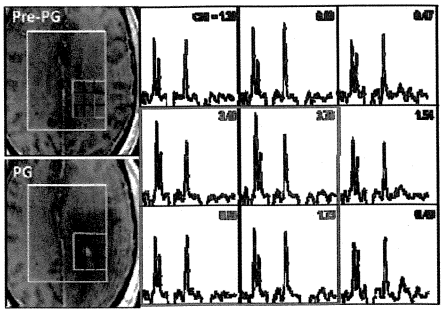

Figure 1. MRSI data from a patient with newly diagnosed GBM at the time of pre-progression that corresponded to new CEL two months later.

Results

The median time to progression was 115 days (range, 52-301 days). Figure 2 showed mean CEL volumes (cc) and CNI values in CEL during the treatment. The CEL volume significantly increased with time prior to PG. The difference in CEL volume between 2 months prior to progression and progression in 13 patients was statistically significant using a signed-rank test (P = 0.021). The CNI values increased with time up until 2 months prior to PG. No significance was found in the CNI within the CEL at Pre-PG and PG and the new CEL at Pre-PG. An example of high CNI values at the time of pre-progression that showed new CEL two months at the time of PG is illustrated in Figure 1.

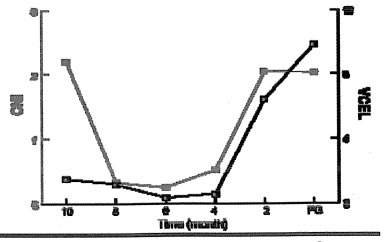

	8-mo	6-mo	4-mo	2-mo
VCEL	**0.009**	**0.001**	**0.001**	0.096
CNI	**0.006**	**0.003**	**0.009**	0.534

Figure 2. Mean CNI values in CEL and CEL volumes along with the P-values between each time point and PG using a ranksum test. There were n=2, 5, 6, 7 and 13 subjects at 10, 8, 6, 4, 2 months prior to progression, and n=18 total subjects at the time of progression.

Discussion

In this study, we assessed changes in metabolism based upon the CNI and demonstrated characteristics of these changes following response to treatment in patients with GBM using MRSI. We found that the CNI values in CEL are elevated at 2 months prior to progression while having less changes in CEL volume at that time. We also noticed that the regions with high CNI values outside the CEL region could subsequently become enhancing. This suggests that metabolic abnormalities more accurately reflect the underlying tumor burden and may provide useful information for following response to therapy in patients with GBM.

Acknowledgements

This research was supported by UC Discovery grant ITL-BIO04-10148, NIH grants R01 CA127612, P01 CA11816 and NIH P50 CA97257.

Comparison of Automatic and Manual Prescription Protocols for Brain 3D MRSI

E. Ozhinsky, D.B. Vigneron, S.M. Chang, S.J. Nelson

Introduction: Manual prescription of brain 3D MRSI is often difficult, since the selected volume (PRESS box) needs to cover the tumor as well as other potential areas of interest, while avoiding subcutaneous lipids and sinuses. The goal of this work was to evaluate the coverage and data quality of MRSI protocols with manual and automatic prescription in order to determine the most effective strategy for implementing automatically prescribed spectroscopy for routine scans of patients with brain tumors.

Methods: MRSI data were acquired using a commercially available 8 channel head coil (isotropic nominal voxel size: 10 mm, TE = 144 ms, TR = 1100-1500 ms) with an EPSI flyback sequence. The following acquisition protocols were tested:

1. Standard Lactate-edited MRSI: 6 fixed sat bands at the edges of the PRESS box, 6 manually placed sat bands. (16x16x16 field of view, acquisition time T_{acq} = 9 min)
2. Lactate-edited MRSI with octagonal selection: Octagonal selection with cosine-modulated saturation pulses was applied instead of fixed sat bands (1).
3. Automatic sat band placement: 6 fixed sat bands and 9 sat bands automatically prescribed from a T1 Fast SPGR image (2) were applied. (18x18x16, T_{acq} = 8 min)
4. Automatic sat band placement with octagonal selection
5. Same as protocol 4 with spectro-spatial RF excitation pulses to eliminate J-modulation of the lactate signal (3).
6. Automatically prescribed oblique lactate-edited MRSI: PRESS box size, position, oblique angle and sat band placement were optimized from a T1-weighted SPGR image to maximize coverage while approximating the shape of the skull (4). (T_{acq}=12 min.)

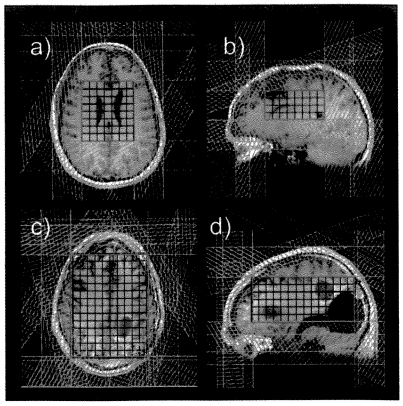

Fig. 1 MRSI prescription with (a,b) manually and (c,d) automatically placed sat bands

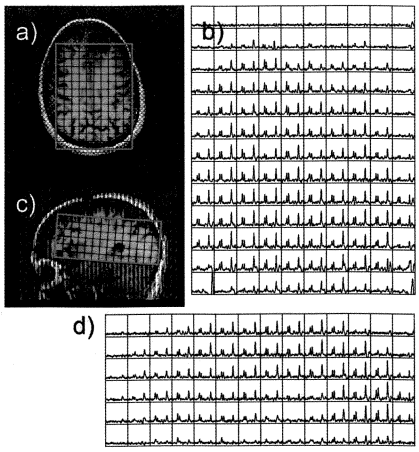

Fig. 2: Automatically prescribed 3D MRSI exam: (a,b) - axial-oblique slice, (c,d) - sagittal slice.

Results: We have collected MRSI data from 3 healthy volunteers and 37 patients with brain tumors. Fig. 1 and 2 show examples of prescriptions for protocols 1, 4, 6. Fig. 3 shows average coverage and SNR efficiency for lipid and NAA peaks (the protocol number is in parentheses). Automatic oblique prescription allowed approximately 3x increase in coverage volume. The NAA signal shows no decline in data quality in datasets with bigger coverage. We did not detect a significant increase in lipid contamination.

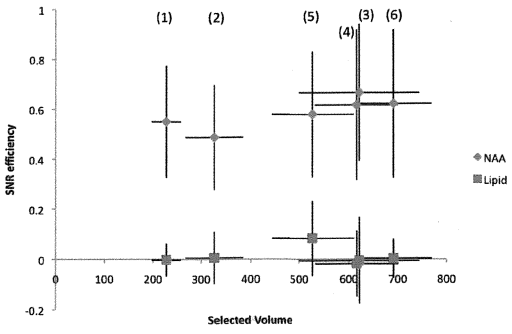

Fig. 3: NAA and lipid SNR efficiency vs. mean brain coverage volume (cm^3); error bars: ±1 std. dev.

Discussion: Our data showed that automatic placement of sat bands not only saved time during prescription, but also allowed to cover a larger volume in the brain. This is especially useful when imaging tumors located near the edge of the brain and multi-focal tumors. We found that it was hard to obtain data from the inferior portions of the brain when acquiring data axially due to the field inhomogeneities and lipid contamination caused by sinuses and orbits. Oblique acquisition helped solve this problem.

References and Acknowledgements: [1] Osorio JA et al. (2009). Magn Reson Med, 61(3), 533-. [2] Ozhinsky E, et al. Proc. 16th ISMRM, 2008: 2377. [3] Cunningham, CH et al. (2005). Magn Reson Med, 53(5), 1033-. [4] Ozhinsky E et al. Proc. 17th ISMRM, 2009: 1580.

This research was funded by UC Discovery grant ITL-BIO04-10148 in conjunction with GE Healthcare.

TITLE: Can signal enhancement ratio (SER) reduce the number of recommended biopsies without affecting cancer yield in occult MRI-detected lesions?

AUTHORS: Vignesh A. Arasu, Ryan C-Y. Chen, David C. Newitt, Belinda Chang, Hilda Tso, Nola M. Hylton, and Bonnie N. Joe

RATIONALE AND OBJECTIVES: We retrospectively determined if signal enhancement ratio (SER), a quantitative measure of contrast kinetics, could reduce the number of biopsy recommendations without decreasing cancer yield in suspicious lesions seen on breast MRI.

MATERIALS AND METHODS: A retrospective review was performed of all suspicious lesions (BIRADS 4 or 5) seen on breast MRI in 2008 that were clinically- and mammographically-occult. Images were processed with in-house software to generate SER parameters. Parameters used to predict benignity included SER washout tumor volume, SER functional tumor volume (volume with "washout" and "plateau" kinetics), SER total tumor volume (volume with "washout", "plateau", and "persistent" kinetics), peak SER, and peak percent enhancement. Thresholds were determined to retrospectively discriminate benign from malignant histopathology. Clinical impact was assessed through the reduction in the number of biopsies recommended (by eliminating benign lesions discriminated by SER), and the consequent cancer yield.

RESULTS: Based on the original radiologist interpretations, 73 occult lesions were called suspicious and biopsied with a cancer yield of 18/73 (25%). Low values of SER parameters were found to be significantly associated with benignity ($p < 0.05$). The adjunctive use of SER parameters reduced the number of recommended biopsies (functional tumor volume: 40 biopsies, total tumor volume: 45 biopsies, peak percent enhancement: 55 biopsies) without decreasing cancer yield (functional tumor volume: 18/40 or 45%, total tumor volume: 18/45 or 40%, peak percent enhancement: 18/55 or 33%).

CONCLUSION: The adjunctive use of SER parameters can reduce the number of recommended biopsies without decreasing cancer yield.

Compositional Signatures for 3-Component Mammography

Fred Duewer, Jennifer Sherman, Bo Fan, Song Ge, Mayrita Vitvitska, Jeff Wang, , Chris Flowers, Karla Kerlikowske, John Shepherd

Breast cancer is the second leading cause of cancer death in women[1]. X-ray mammography is the primary available technology used for early detection of breast cancer. Studies have demonstrated breast cancer mortality reductions of up to 25% following the introduction of X-ray mammography for screening[2]. However, mammography has only moderate accuracy. Improvements in the sensitivity and specificity of screening mammography may increase the potential benefits of screening and decrease the potential harms.

The fundamental information that a radiologist uses, the single-energy attenuation of low-energy X-rays, has remained the same since the inception of breast imaging in 1913[3]. Without additional information, mammography provides only relative radiopacity (i.e. tissue density relative to a background of fat) and lesion shape. Lesion classification is limited to detection of calcifications and the shape and symmetry of high density breast masses and therefore has limited reliability in predicting invasive breast cancer. The result is 25% of biopsies are breast cancer.

We have developed a novel dual-energy imaging technique, compositional 3-component breast imaging (3CB), to quantify the lipid, protein, and water thicknesses of invasive cancer relative to other types of tissue that trigger a biopsy. The protocol was designed to be dose conservative (10% higher than screening mammography) and was performed on a standard full-field digital mammography system with the addition of a 3-mm Al filter for the high-energy image[4]. A pilot study of nine women with abnormal breast findings on diagnostic mammography was performed using the 3CB protocol. Identifiable lesions were delineated and the median compositional thicknesses measured relative to their peripheral tissue.

We present distinct "signatures" for invasive cancer, DCIS, fibroadenoma, and benign tissue. Invasive cancers and fibroadenomas showed increased water relative to surrounding tissue and to DCIS and benign tissue. However, invasive cancer had increased protein content relative to fibroadenomas. Our preliminary data indicate that the technique provides diagnostically useful and biologically meaningful compositional "signatures" of the lesion type.

1. A. Jemal, R. Siegel, E. Ward, Y. Hao, J. Xu, T. Murray and M. J. Thun, CA Cancer J Clin **58** (2), 71-96 (2008).
2. H. D. Nelson, K. Tyne, A. Naik, C. Bougatsos, B. K. Chan and L. Humphrey, Ann Intern Med **151** (10), 727-737, W237-742 (2009).
3. A. Salomon, Arch Klin Chir **101**, 573-668 (1913).
4. A. D. Laidevant, S. Malkov, C. I. Flowers, K. Kerlikowske and J. A. Shepherd, Med Phys **37** (1), 164-174.

SPECT Dual-Isotope Myocardial Perfusion Imaging with a 20-Pinhole Collimator: a Simulation Study

Jason D. Bowen[1], Qiu Huang[2], Grant T. Gullberg[3], and Youngho Seo[1]

[1]*Department of Radiology, University of California, San Francisco, CA, United States*
[2]*Shanghai Jiao Tong University, Shanghai, China*
[3]*Lawrence Berkeley National Laboratory, Berkeley, CA, United States*

SPECT imaging systems have essentially remained an unchanged technology since the introduction of parallelhole collimation in 1964 and stand to gain significantly from sensitivity improvements. Benefits of improved sensitivity include shorter acquisition times and smaller dose requirements. An order-of-magnitude increase in sensitivity over conventional technology is possible with the use of multipinhole collimators. Here we present simulation results of a dual-isotope myocardial perfusion imaging study performed with a pair of 20-pinhole collimators with tungsten apertures demonstrating that a complete rest/stress study is possible in 10 minutes and with reduced dose. Monte Carlo (MC) simulations using GEANT3 [1] were performed to assess the effects of scatter and fluorescence on projection measurements and the image reconstruction process. Two radionuclides were simulated, ^{99m}Tc (500 μCi, rest) and ^{201}Tl (200 μCi, stress), with 20% and 30% window sizes, respectively. Full isotropic emission was simulated for one ^{99m}Tc and seven ^{201}Tl gamma-ray lines. The imaging protocol consisted of 4 views with 300 s per view. The activity distributions were derived from the MCAT phantom [2]. Attenuation was modeled using a water phantom. A ray-driven projector/backprojector pair [3] was used to generate the projections used for the image reconstructions. Poisson noise and the MC derived scatter components were added to the projections prior to reconstruction. Images were reconstructed using 75 iterations of pixel-based OSEM (4 subsets) [4] and post-filtered with a 10 mm (FWHM) 3D isotropic Gaussian filter. Scatter corrections were performed using the triple energy window method [5]. Scatter comprises 37% and 60% of the total counts in the ^{99m}Tc and ^{201}Tl energy windows, respectively. Downscatter from the ^{99m}Tc 140 keV line contributes 52% of the scatter component in the ^{201}Tl window, though tungsten fluorescence is negligible (0.2%). The distribution of the ratios of the known scatter components to the estimates in the ^{201}Tl window is approximately Gaussian with a mean of 0. 6 and standard deviation 0.1, suggesting a global correction factor dependent only on window size may be possible. Reconstructed images are qualitatively in good agreement with the input activity distributions (Figure 1).

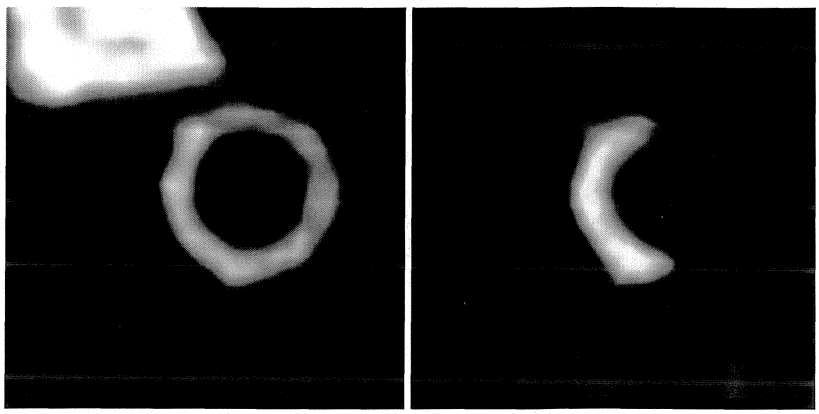

(a) (b)

FIGURE 1. Short axis views of reconstructed images for (a) rest (^{99m}Tc 140 keV window) and (b) stress (^{201}Tl 70 keV window) acquisitions. Note the defect in (b). Extra-cardiac activity is excluded in (b).

REFERENCES

[1] Sturner, S. J. et al, *Proc. Fifth Comp. Symp.*, ed. M. L. McConnel \& J. M. Ryan (AIP, New York) 824.
[2] Segars, W. P. et al, *IEEE Trans. Nucl. Sci.*, **48**, 1, (2001) 89-97.
[3] Hu, Jicun et al, *LBNL Report Number LBNL-60008*, 2008.
[4] Branderhorst, Woutjan et al, *Phys. Med. Biol.* **55**, (2010) 2023-2034.
[5] Ogawa, Koichi, *IEEE Trans. Med. Imaging.*, **10**, 3, (1991) 408-412.

Title: Phantom experiments on a PSAPD-based compact gamma camera with submillimeter spatial resolution for small animal SPECT

Authors: Sangtaek Kim, Mickel McClish, Fares Alhassen, Youngho Seo, Kanai S. Shah and Robert G. Gould

We demonstrate a position sensitive avalanche photodiode (PSAPD) based compact gamma camera for the application of small animal single photon emission computed tomography (SPECT). The silicon PSAPD with a two-dimensional resistive layer and four readout channels is implemented as a gamma ray detector to record the energy and position of radiation events from a radionuclide source. A 2 mm thick monolithic CsI:Tl scintillator is optically coupled to a PSAPD with a 8mm×8mm active area, providing submillimeter intrinsic spatial resolution, high energy resolution (16% full-width half maximum at 140 keV) and high gain. A mouse heart phantom filled with an aqueous solution of 370 MBq ^{99m}Tc-pertechnetate (140 keV) was imaged using the PSAPD detector module and a tungsten knife-edge pinhole collimator with a 0.5 mm diameter aperture. The PSAPD detector module was cooled with cold nitrogen gas to suppress dark current shot noise. For each projection image of the mouse heart phantom, a rotated diagonal readout algorithm was used to calculate the position of radiation events and correct for pincushion distortion. The reconstructed image of the mouse heart phantom demonstrated reproducible image quality with submillimeter spatial resolution (0.7 mm), showing the feasibility of using the compact PSAPD-based gamma camera for a small animal SPECT system.

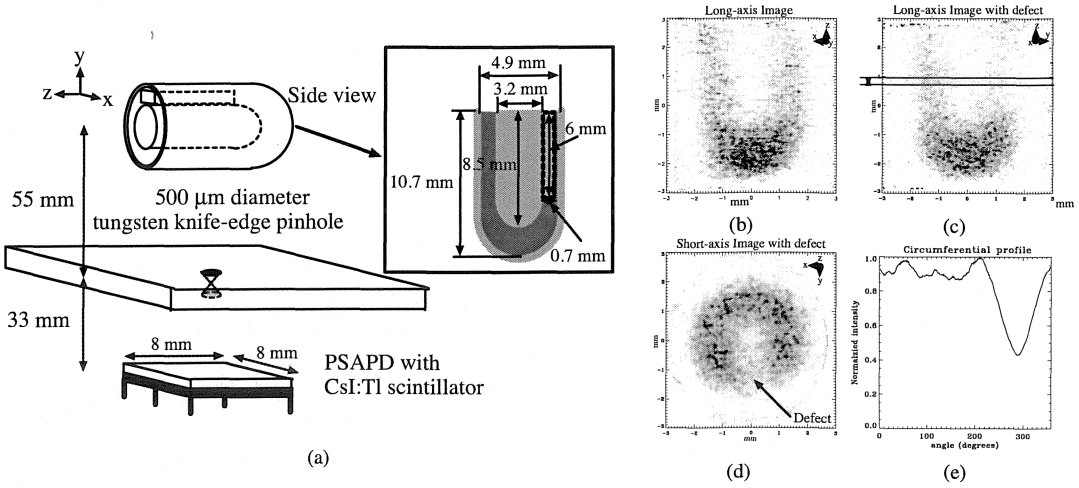

Fig. 1. (a) Schematic drawing of our CsI:Tl/PSAPD SPECT system setup with a single tungsten knife-edge pinhole used for the mouse heart phantom study. A mouse heart phantom filled with an aqueous solution of ^{99m}Tc-pertechnetate is projected through the pinhole with a 0.5 mm diameter aperture onto the CsI:Tl/PSAPD. The inset shows the dimensions of the mouse heart phantom with a defect lesion used for our experimental measurement. (b) Reconstructed image of mouse heart phantom with defect. A long-axis view of the mouse heart phantom. The center rod of the phantom is visible as a cold area within the U-shaped activity distribution. (c) The other long-axis view of the phantom showing the cold defect area. At the upper-right side of image, the defect is visible as less concentrated activity. (d) Summed short-axis image of the phantom with defect. The location is indicated in Fig. 1(d). The defect is observable at the bottom part, where it shows less concentrated activity compared with the rest of activity distribution. (e) Circumferential profile of the mouse heart phantom slices shown in Fig. 1(d).

Preparation of 12a-[^{18}F]fluoromethyl-rotenone: A novel positron emitting cardiac blood flow tracer

Joseph E. Blecha; Leila A. Ranis; Bin Zang; Michael Pun; Henry F. VanBrocklin

Department of Radiology and Biomedical Imaging UCSF

Objectives: Radiolabeled rotenone analogs **1**, a natural product found in the roots of the tropical Derris plant, have been shown to be sensitive perfusion tracers with high extraction and retention. These analogs demonstrated better linearity with flow than the current clinical tracers.

Methods: The synthesis of a new fluorine-18 labeled rotenone analog is shown in scheme 1. Readily available rotenone **1** is converted to 12a-hydroxymethylrotenone **2** by reaction with paraformaldehyde. The tosylate leaving group is introduced by reacting **2** with tosyl chloride. Reaction of the tosylate precursor **3** with tetrabutylammonium [^{18}F]fluoride in acetonitrile and t-butanol for 10 minutes by microwave yields the desired [^{18}F]fluoromethylrotenone **4**. MicroPET imaging of **4a** and **4b** were performed in Sprague-Dawley rats.

Results: The conversion of rotenone to hydroxymethyl rotenone epimers was 80%. The formation of the corresponding toluenesulfonyloxymethyl rotenones proceeded in 50% yield. The radiochemical yield of **4**, employing the polar aprotic solvent tBuOH was 65%. MicroPET images below showed localization of [^{18}F]fluoromethylrotenones in the heart with minimal tracer uptake to the lungs.

Conclusions: The synthesis of these analogs possesses several advantages over the previously synthesized [^{18}F]fluorodihydrorotenone analogs. The precursor was prepared in two steps from rotenone; the [^{18}F]fluoride ion was introduced in high yield into the desired product in a single step reaction; and the strategically placed fluoromethyl group prevents oxidation of the rotenone. Small animal imaging demonstrated the cardiac accumulation of this new tracer. These new rotenone analogs show promise as potential PET cardiac perfusion tracers.

Scheme 1

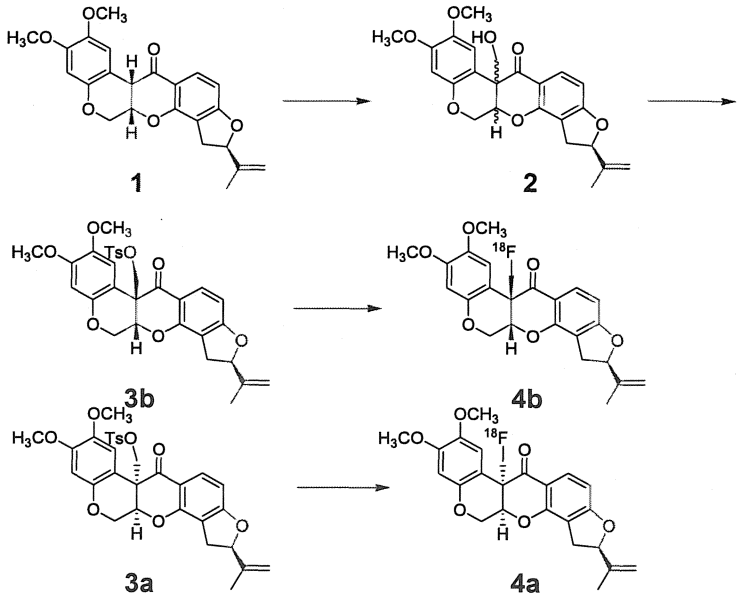

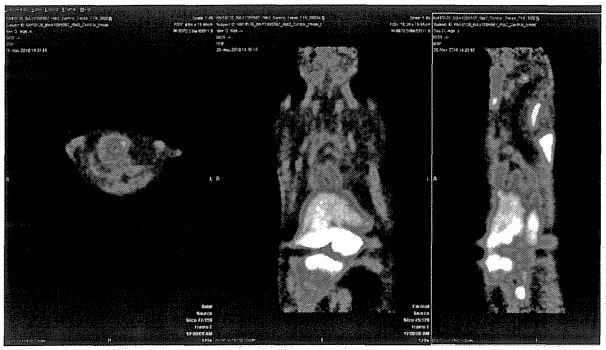

uPET scan of rat injected with **4b**

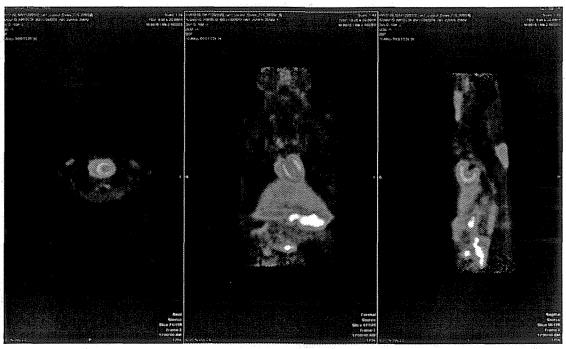

uPET scan of rat injected with **4a**

Automated $[^{18}F]F_2$ gas production from $[^{18}F]$fluoride ion

Shorouk Dannoon[1], James Powell[1], Michael Pun[1], Shane Joseph[1], Joseph E. Blecha[1], Thomas Ruth[2], Henry F. VanBrocklin[1]

[1]Department of Radiology and Biomedical Imaging, University of California San Francisco, USA
[2]University of British Columbia & TRIUMF, Vancouver BC, Canada

Objectives : The objective of this work is to increase the availability of high specific activity $[^{18}F]F_2$ gas for radiotracer preparation through the development of an automated production system. The two step process entails the production of $[^{18}F]$fluoromethane ($CH_3{}^{18}F$) from aqueous $[^{18}F]$fluoride ion (^{18}F) with subsequent conversion to $[^{18}F]F_2$ gas by the Bergman and Solin (1997) electric discharge method.

Methods : A device was built for automated preparation of $CH_3{}^{18}F$ including concentration of the fluoride ion from the cyclotron ($[^{18}F^-]$, elution with aqueous DMSO and reaction with aryl trimethylammonium salts at 170° C (Figure 1). A second device was built to receive the $CH_3{}^{18}F$ for electric discharge conversion to $[^{18}F]F_2$ gas (Figure 2). The percentage of $[^{18}F]F_2$ gas produced was determined by trapping in solid potassium iodie (KI). The reactivity of the $[^{18}F]F_2$ was determined by reaction with FDOPA precursor in Freon-11 and EF5 precursor in trifluoroacetic acid (TFA). Products were characterized by HPLC comparison with standards. Different variables (amount of nonradioactive $[^{18}F]F_2$ gas, spark time (10 sec vs. 3 min), current voltage applied (up to 0.4mA), and size of spark chamber) were evaluated to determine the ideal conditions for $[^{18}F]F_2$ gas production.

Results : Reaction of aryl trimethylammonium salts with aqueous $[^{18}F^-]$ gave consistently quantitative yields of $CH_3{}^{18}F$. The percentage yield of $[^{18}F]F_2$ gas produced ranges up to 40% based on $CH_3{}^{18}F$ activity. $[^{18}F]$FDOPA and $[^{18}F]$EF5 labeling was confirmed on RP-HPLC.

Conclusions : An automated $[^{18}F]F_2$ production system has been developed. This system can be used multiple times in one day to produce $[^{18}F]F_2$ on demand without intervention. Further optimization is warranted to obtain an improved $[^{18}F]F_2$ yield.

Research Support : This research was supported in part by the Office of Biological and Environmental Research, US DOE under grant no DE-FG02-08ER64699 and a grant from Varian Byosynergy.

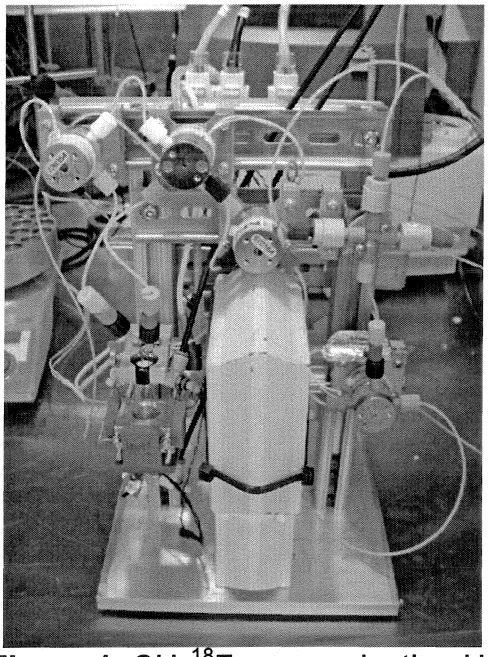

Figure 1: $CH_3{}^{18}F$ gas production Unit

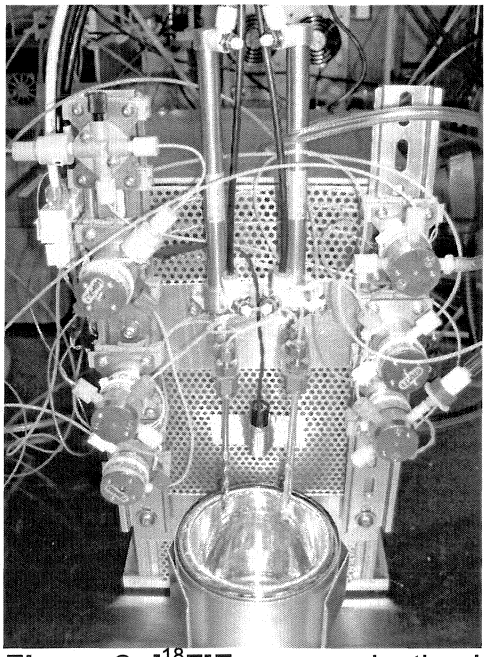

Figure 2: $[^{18}F]F_2$ gas production Unit

Comparison of breath-hold and free-breathing diffusion-weighted techniques for liver MR diffusivity in healthy volunteers and patients

Mamak Eatesam, MD, Susan M Noworolski, PhD, Phyllis Tien, MD, Michelle Nystrom, BS,
Jennifer Dodge, MPH, Raphael Merriman, MD, Aliya Qayyum, MBBS
Department of Radiology and Biomedical Imaging (ME, SMN, MN, AQ, JD)
Department of Medicine (PT, RBM)

Purpose: To compare liver apparent diffusion coefficient (ADC) values obtained with breath-hold and free-breathing diffusion weighted imaging (DWI) in healthy volunteers and patients with chronic liver disease.

Materials and Methods: Twenty eight subjects, including 12 healthy volunteers and 16 patients (9 NAFLD, 7 chronic active HCV), underwent breath-hold (BH) (24 sec) and free-breathing (FB) (5 min) diffusion-weighted imaging of the liver. ADC measurements were obtained at 3 axial liver levels. Correlations and variability between BH and FB ADC values across groups were determined with Pearson's correlation coefficient and Bland-Altman plots. Group means were compared with t-tests.

Results: Liver ADC was higher in healthy volunteers compared to patients with NAFLD and compared to the FB ADC of HCV patients, but not the BH ADC of the HCV patients [see Table 1]. Liver ADC was significantly lower on BH compared to FB in all groups with a mean difference of 0.36±0.20 x10^{-3} ($p<0.01$) [Table 1]. Across all patients, the correlation coefficient between BH and FB liver ADC was 0.77, (NAFLD, r=0.90; healthy volunteers, r=0.34; HCV, r=0.24). Bland-Altman plots demonstrated a lower ADC variation between BH and FB liver ADC (x 10^{-3} mm²/ sec) in patients compared to healthy subjects (0.11 to 0.59 in NAFLD patients; -0.15 to 0.64 in HCV patients; 0.003 to 0.87 in volunteers).[Figure2]

	BMI	Avg ADC in BH	Avg ADC in FB	ADC Reduction
Healthy [n=12]	22.74± 1.65‡	1.80± 0.18†	2.24± 0.20†	0.43± 0.22*
All Patients [n=16]	28.2± 8.46	1.52± 0.25	1.82± 0.22	0.30± 0.16*
NAFLDs [n=9]	32.22± 9.15‡	1.43± 0.27†	1.78± 0.28†	0.35± 0.12*
HCVs [n=7]	24.17± 5.78‡	1.63± 0.19†	1.88± 0.12	0.24± 0.20*
Entire Population [n=28]	25.92± 7.00	**1.64± 0.26**	**2.00± 0.30**	**0.36± 0.20***

Table 1- Average right lobe liver ADC (x 10^{-3} mm/sec) and ADC decrease (reduction) between FB and BH DWI.
‡ denotes significant difference between NAFLD and other 2 groups ($p<0.05$)
† denotes significant difference between Healthy volunteers and other groups ($p< 0.01$)
* denotes significant difference between BH and FB ($p<0.01$)

Figure 1- Bland- Altman plots showing lower (not significant) ADC variation in patients with non alcoholic liver disease. ADC values are given as × 10^{-3} mm/sec.

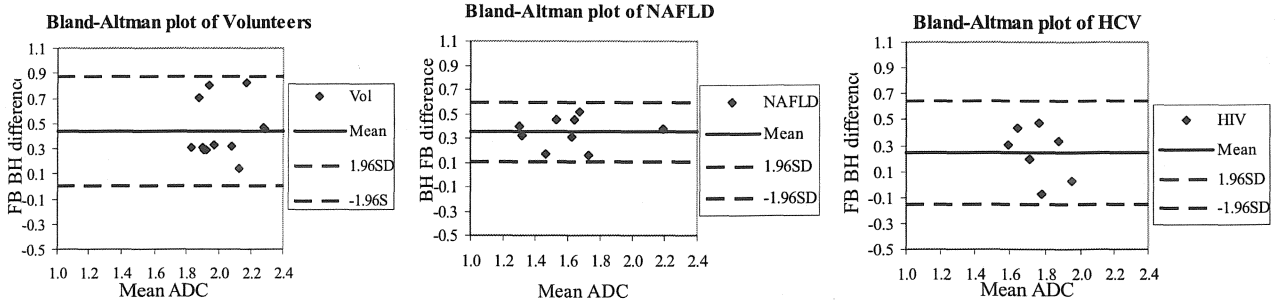

Conclusion: The correlation between BH and FB liver ADC is moderate at best such that BH and FB DWI techniques should not be used interchangeably. The higher correlation of FB with BH in NAFLD subjects, and lower variability of FB and BH in this group, suggests that disease induced changes in the liver, including changes in perfusion, may affect their FB. Alternatively or additionally, the higher BMI in the NAFLD population may also alter their FB versus BH diffusion, perhaps due to obesity related changes in respiratory volume [1]. The consistently higher ADC values in FB versus BH levels should be accounted for when evaluating and comparing different liver MR diffusion studies.

References:1. Saxena Y, Sidhwani G, Upmanyu R. Abdominal obesity and pulmonary functions in young Indian adults: a prospective study. *Indian J Physiol Pharmacol* 2009;53(4):318-26.

Imaging of Hepatic Steatosis and Hyperpolarized Carbon Metabolism at 14T –Applications to a Murine Model of Non-Alcoholic Fatty Liver Disease (NAFLD)

Andrew G. Taylor, Kayvan R. Keshari, Robert Bok, Subramaniam Sukumar, Aliya Qayyum and John Kurhanewicz
Department of Radiology and Biomedical Imaging, University of California, San Francisco (UCSF), San Francisco, California

Magnetic resonance imaging at high field allows the acquisition of anatomic images with exquisite spatial resolution and detail. Additionally, specialized pulse sequences can be used to determine the degree of adiposity of tissues *in vivo*, providing a method to visualize the severity of steatosis within the liver. Hyperpolarized ^{13}C magnetic resonance imaging and spectroscopy continues to be a valuable tool for the investigation of metabolic and biochemical processes in a variety of organs and pathologic conditions.

The goal of these studies is to utilize hyperpolarized ^{13}C MR to identify and quantify metabolic derangements in mice fed a diet deficient in methionine and choline (MCD diet), an animal model of Non-Alcoholic Fatty Liver Disease. Initial work has resulted in the successful acquisition at 14T of respiratory-gated anatomic images of the murine abdomen, the development of a pulse sequence allowing for simultaneous acquisition of quantitative fat- and water-sensitive images, and the use of hyperpolarized ^{13}C MR imaging to produce 3D maps of pyruvate metabolism within the livers of normal mice and those with NAFLD.

Co-localized water- and fat-sensitive axial images were acquired simultaneously through the livers of both normal and NAFLD mice using a frequency-specific gradient reversal technique[1]. The resulting images demonstrate a marked increase in the degree of fat signal within the hepatic parenchyma after 14 days of feeding the MCD diet when compared to the livers of normal mice **(figure 1)**. Additionally, characterization of the pulse sequence using lipid/water emulsions of varying concentrations demonstrates a linear relationship between signal intensity and fat percentage in lipid sensitive images (data not shown), allowing quantification of the increasing deposition of microscopic fat in the liver parenchyma.

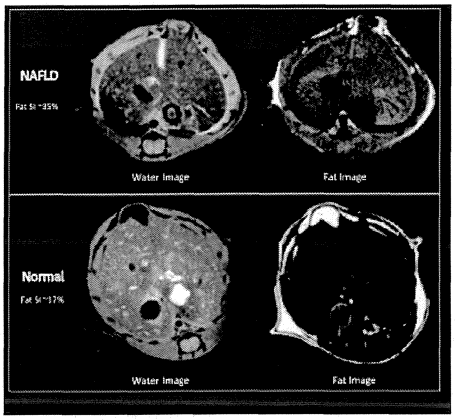

Hyperpolarized ^{13}C experiments were performed using a preparation of 14.2M [1-^{13}C]-pyruvate and 6.4M ^{13}C-urea combined with OX63 radical and polarized in an Oxford Hypersense system. Frequency specific pulses (for alanine, pyruvate, lactate and urea) were implemented with an echo-planar imaging sequence to generate 3D images of the distribution of each metabolite, and overlaid on the spatially matched anatomic images **(figure 2)**. These images provide the basis for quantitative comparison of metabolic changes in the MCD model of fatty liver disease.

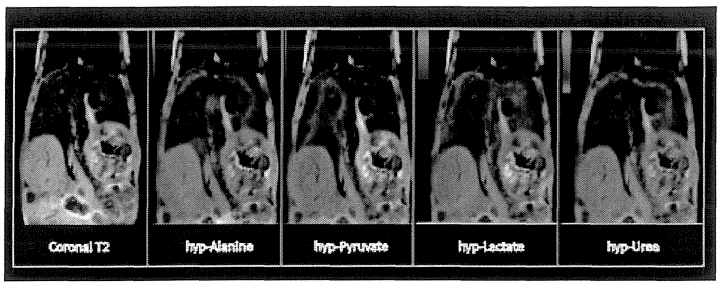

Reference:

1. Tang et al. J Mag. Res. Imaging 2007; 26(4): 1064-70.

7T human liver imaging using microstrip surface coil

Yong Pang[1], Xiaoliang Zhang[1, 2]

[1]Radiology&Biomedical Imaging, University of California San Francisco, San Francisco, CA, United States, [2]UCSF/UC Berkeley Joint Graduate Group in Bioengineering, San Francisco & Berkeley, CA, United States

Introduction: MRI can provide clinically-valuable images for hepatic diseases and has become the most accurate noninvasive method in evaluating liver lesions [1]. At high and ultrahigh field, liver images may be acquired within breath-hold period using very short TE, essentially reducing the scanning time and motion artifacts. However, B_1 variation can cause significant problems at high field [2]. This requires RF coils with deep penetration and relatively homogeneous B_1 field at high frequency. In this work, T1 weighted human liver images at 7T were acquired using a fast gradient echo sequence and a $\lambda/2$ microstrip surface coil on GE whole body 7T scanner.

Material and method: A capacitor terminated $\lambda/2$ microstrip surface coil was built to excite and detect the MR signals of the human liver. As shown in Figure 1, the microstrip coil is circular shaped with 12.5cm ID, 15.3cm OD. a capacitor with nominal capacitance of 2.7pF and a variable capacitor ranging from 1pF to 25pF were used as termination capacitors. Another distributed capacitor was placed at the center of the coil. This circular strip conductor was built on the top of a square, low-loss Teflon substrate with permittivity of 2.1, side length of 20cm and thickness of half inch. The ground was a single piece copper adhered to the bottom of the substrate. Bench testing of this coil was performed using an Agilent network analyzer. At 298.2 MHz the S11 parameter in the loaded case reached -50dB. The unloaded and loaded Q factors were 330 and 40 respectively.

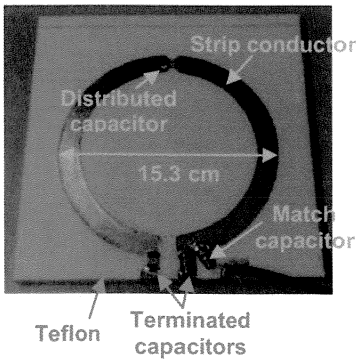

Fig. 1 prototype of the capacitor terminated $\lambda/2$ microstrip surface coil for human liver imaging.

In vivo experiments were performed on a GE whole body 7T scanner with maximum gradient strength of 4 Gauss/cm and maximum slew rate of 15 Gauss/cm/ms. The subject position was supine, entry was feet-first and the surface coil was positioned over the liver. A fast gradient echo sequence was used for imaging 8 sequential coronal slices of the liver of a health volunteer in a breath-hold. Receiver bandwidth = 23.4*k*Hz, FOV = 20cm, slice thickness = 5mm, slice spacing = 3mm, matrix = 384×256, phase FOV = 1, flip angle = 30°, TR = 6ms and TE = 1.64ms, NEX = 2. The phase encoding direction was Superior-Inferior.

Results: Each imaging set was performed within a breath hold with an acquisition time of up to 23 s. High resolution images of 8 coronal plane slices were acquired and are shown in Figure 2. The SNR of each slice is shown in table 1. In the image of the deepest slice *a*, the SNR can still reach 33.4.

Slice	a	b	c	d	e	f	g	h
Superior(mm)	5.5	13.5	21.5	29.5	37.5	45.5	53.5	61.5
SNR	33.4	36.6	61.3	51.6	59.4	63.5	78.8	96.1

Tab. 1 SNR of each slice at different coronal positions.

Conclusion and discussion: MR imaging of the human liver was performed at 7T with a gradient echo sequence using a $\lambda/2$ microstrip surface coil with a large size for better coverage. With breath holding the motion artifact was minimal allowing high SNR 7T images of the liver. This experiment has demonstrated the feasibility of liver imaging at 7T. Further investigations with higher resolution, better sequences and optimized imaging parameters are now being pursued.

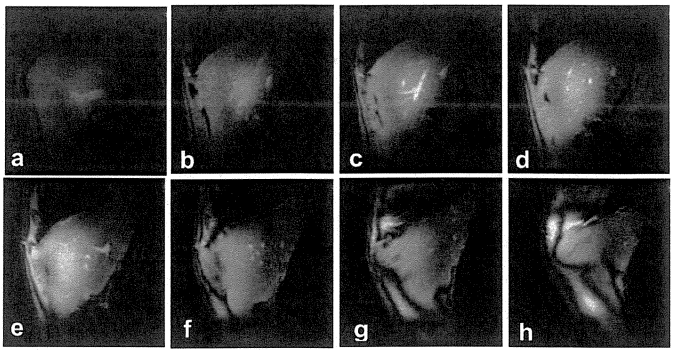

Fig. 2 8 coronal slices at different positions (superior 5.5mm to 61.5mm) using fast gradient echo. Imaging parameters: bandwidth = 23.4*k*Hz, FOV = 20cm, slice thickness = 5mm, slice spacing = 3mm, matrix = 384×256, phase FOV = 1, flip angle = 30°, TR = 6ms and TE = 1.64ms, NEX = 2.

References: [1] Halavaara J, academic dissertation, Helsinki 2002. [2] Padormo F, et al, ISMRM 2009: p754.

Acknowledgements: This work was supported in part by NIH grants EB004453, CA137298 and a QB3 opportunity award.

Variations in distal radius morphological and biomechanical indices among subjects with identical BMD values

Galateia Kazakia, Andrew Burghardt, Thomas Link, Sharmila Majumdar
Musculoskeletal Quantitative Imaging Research Group, Department of Radiology and Biomedical Imaging

Introduction: Determination of osteoporotic status is based primarily on areal bone mineral density (aBMD) and the related T-score obtained through dual x-ray absorptiometry (DXA). While aBMD has been shown to be clinically useful in predicting fracture in prospective studies, it does not entirely determine fracture risk or fully capture the impact of therapeutic interventions. Over half of osteoporotic fractures occur in patients with T-scores above the WHO threshold of osteoporosis, in part because DXA measures are insensitive to biomechanically important alterations in bone quality. The goal of this study was to determine the extant variation in densitometric, geometric, microstructural, and biomechanical parameters within groups of subjects with identical distal radius aBMD values.

Methods: High resolution peripheral quantitative computed tomography (HR-pQCT) and DXA radius data were drawn from a database that includes males and females with large variations in age, osteoporotic status, and anthropometrics. A total of 262 distal radius data sets were processed for this study. HR-pQCT scans were analyzed according to the standard clinical protocol to quantify densitometric, geometric, and microstructural indices. Micro finite element analysis was performed to calculate biomechanical indices. Factor of risk of wrist fracture was calculated from anthropometric data. Simulated aBMD calculated from HR-pQCT data and osteoporotic status as defined by DXA T-score was used to group scans for evaluation of variation in quantified indices.

Results: Indices reflecting the greatest variations within aBMD groups were volumetric BMD in the central portion of the trabecular compartment ($Tb.vBMD_{inn}$ max variation 153%), trabecular heterogeneity (Tb.1/N SD, max variation 128%), and intra-cortical porosity (Ct.Po, max variation 185%). Of the biomechanical indices, cortical load fraction (Ct.LF) had the greatest variation (max variation 96%). As expected, densitometric indices were positively correlated with aBMD values (R^2 = 0.73 to 0.37, $p<0.0001$). Cortical geometric indices cortical area (Ct.Ar) and thickness (Ct.Th) were also positively correlated with aBMD (R^2 = 0.80 and 0.70, $p<0.0001$). In the trabecular compartment, trabecular number (Tb.N) and thickness (Tb.Th) were positively associated with aBMD (R^2 = 0.25 and 0.48, $p<0.0001$) while separation (Tb.Sp) and heterogeneity (Tb.1/N SD) were negatively associated with aBMD (R^2 = 0.27 and 0.17, $p<0.0001$). Cortical porosity (Ct.Po) was negatively associated with aBMD (R^2 = 0.11, $p<0.0001$). Biomechanical parameters stiffness (K), apparent modulus (E), and estimated failure load (F) were positively associated with aBMD (R^2 = 0.77, 0.61 and 0.83, respectively, $p<0.0001$) while factor of risk was negatively associated with aBMD (R^2 = 0.80, $p<0.0001$).Distributions of biomechanical indices for data sets grouped by T-score demonstrate considerable overlap among subjects in the normal, osteopenic, and osteoporotic ranges.

Discussion: Substantial variations in indices reflecting density, structure, and biomechanical competence exist among subjects with identical aBMD values (Fig. 1). Overlap of these indices among aBMD and T-score groups reflects the reported incidence of osteoporotic fracture in subjects classified as osteopenic or normal according to T-score. Quantification of parameter variations may aid in the interpretation of DXA results and reinforces the importance of high-resolution volumetric imaging in bone quality assessment.

UD Radius aBMD 0.39
UD Radius T-score -0.9

Ct.vBMD	839	733
Tb.vBMD	91	147
$Tb.vBMD_{inn}$	50	110
Tb.N	1.16	1.77
Tb.1/N SD	0.524	0.194
Ct.Po	0.014	0.044
Ct.LF	54	40

UD Radius aBMD 0.28
UD Radius T-score -1.7

Ct.vBMD	919	781
Tb.vBMD	60	151
$Tb.vBMD_{inn}$	12	107
Tb.N	0.86	1.8
Tb.1/N SD	0.683	0.196
Ct.Po	0.005	0.024
Ct.LF	67	34

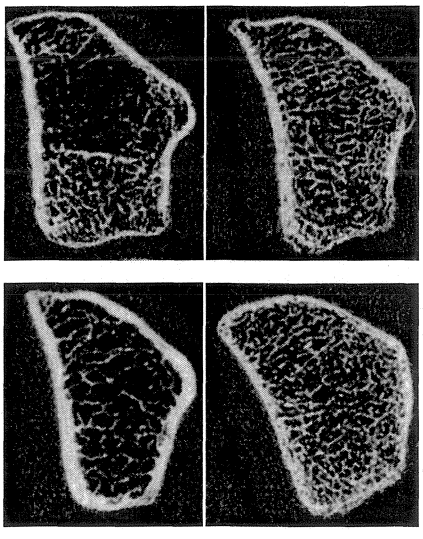

Figure. 1: Representative images of subjects with identical aBMD and T-score and large variations in select architectural and biomechanical indices. A single slice from each HR-pQCT image is shown. Image pairs are scaled to maintain relative size and image intensity.

Acknowledgements: The authors would like to thank Gregory Bernstein for his assistance with data compilation and Melissa Guan and Thelma Munoz for their support with patient scanning and clinical coordination. Funding for this project was provided by NIH K01 AR056734-01 (GJK), NIH/NCRR UCSF-CTSI Grant Number UL1 RR024131-01 (AJB), NIH R01 AG17762 (SM), and a grant by Merck & Co., Inc (TL).

Quantitative characterization of motion artifact in the HR-pQCT images of distal radius and tibia

M. Sode[1,2], A.J. Burghardt[2], J.B. Pialat[2,3], T.M. Link[2], S. Majumdar[1,2]

[1]Joint Graduate Group in Bioengineering, University of California at San Francisco and Berkeley, San Francisco and Berkeley, California, USA
[2]Musculoskeletal Quantitative Imaging Research Group, Department of Radiology and Biomedical Imaging, University of California at San Francisco, San Francisco, California, USA
[3]INSERM U831 and Université de Lyon, Lyon, France

Motion artifacts are commonly seen in *in vivo* high-resolution peripheral quantitative computer tomography (HR-pQCT) images, especially at the radius. Compromised image quality especially confounds the accuracy of trabecular structure measurements, as well as density and cortical geometry measurements. It often leads to repeating the acquisition, thereby exposing the subject to more radiation from HR-pQCT images. A non-subjective, standardized procedure for making an immediate decision for repeating the acquisition is necessary. To achieve this goal, (1) an optimal metric for estimating the error in density and structure measures due to motion degradation is established, and (2) correlations between the metric and expected errors in density and structure measures is quantified in this study.

All dataset with repeated acquisitions of the same site acquired during a single exam collected for various studies conducted in our laboratory were retrospectively evaluated. Two trained observers independently graded all the images according to the manufacturer-suggested image quality grading system. In case of disagreement, a consensus grade was decided mutually. For this study, all exams with pairs that include at least one grade 1 image (no visible motion) were included. A total of 54 pairs of HR-pQCT images of the distal radius (N=33) and tibia (N=21) acquired for 51 women (age = 59±14 yr) and 3 men (46±2 yr) resulted. The cortical and trabecular densitometric and structure indices were calculated for each image, and the % difference between the pair was calculated as the error due to motion. After the raw cone beam projection images were parallelized and corrected for dark and flat field intensity, four commonly used similarity measures, namely sum of squared intensity difference (SSD), ratio image uniformity (RIU), and cross correlation (CC) were used to compare the parallelized projection images, as well as entropy on the difference image. The grater the value of a similarity measure, the larger the disagreement between the projection images, presumably caused by patient motion during acquisition. A linear regression analysis was performed for the correlation (Spearman's ρ) between the % error in each index and the similarity measures.

With increased motion artifact, cortical volumetric bone mineral density (Ct.vBMD) and cortical thickenss (Ct.Th) were increasingly underestimated, and bone volume fraction (BV/TV) and trabecular number (Tb.N) were increasingly overestimated (Figure 1). All similarity measures positively and significantly correlated with most of the % error in density, cortical geometry, and trabecular structure parameters (ρ=0.27-0.58; all p≤0.04) (Figure 1). For instance, a 50% increase in SSD results in up to 4-fold increase in the errors in the Tb.N at the distal radius and tibia. This study is novel in providing the empirical data that can serve as a basis for establishing a non-subjective, standardized criteria for repeating the acquisition according to the specific study design.

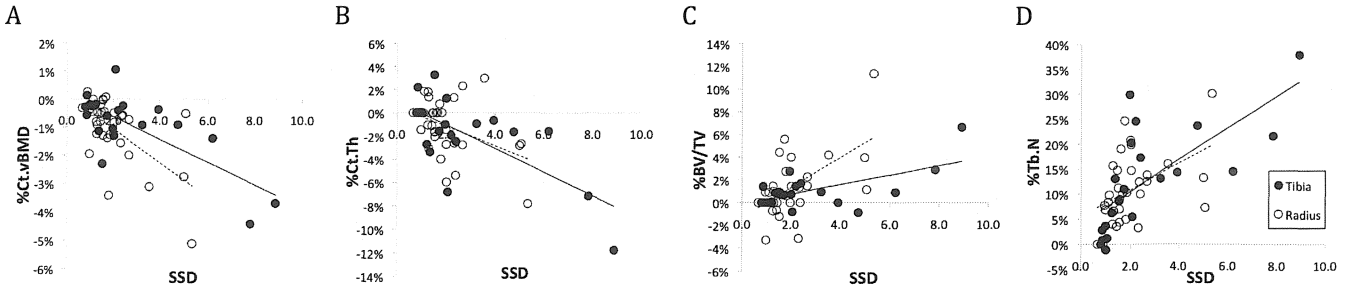

Figure 1. The correlations between % difference in (a) Ct.vBMD, (B) Ct.Th, (C) BV/TV, and (D) Tb.N and SSD.

Table 1 Correlations (Spearman's ρ) between the normalized similarity measures of the projection images with motion artifact and the absolute percent errors introduced to the densitometric, cortical geometric and trabecular structure indices at the distal radius and tibia.

	Tot.vBMD		Ct.vBMD		Tb.vBMD		Ct.Th		Ct.Ar		BV/TV		Tb.N		Tb.Th		Tb.Sp	
	Rad	Tib	Rad	Tib	Rad	Tib	Rad	Tib	Rad	Tib	Rad	Tib	Rad	Tib	Rad	Tib	Rad	Tib
SSD	0.35[a]	NS	0.37[a]	0.63[b]	0.43[a]	0.49[a]	0.53[b]	0.50[a]	0.50[b]	0.47[a]	0.39[a]	0.46[a]	0.46[b]	0.83[a]	NS	0.81[c]	0.48[b]	0.82[a]
CC	NS	NS	0.40[a]	0.54[a]	NS	NS	NS	NS	NS	NS	NS	NS	0.42[a]	0.77[a]	0.38[a]	0.73[c]	0.41[a]	0.75[a]
RIU	0.41[a]	NS	0.41[a]	0.61[b]	0.40[a]	NS	0.52[b]	0.49[a]	0.55[b]	0.47[a]	0.40[a]	NS	0.45[b]	0.79[a]	0.34[a]	0.77[c]	0.47[b]	0.78[a]
E	0.37[a]	NS	0.41[a]	0.58[b]	0.46[b]	NS	0.38[a]	0.46[a]	0.36[a]	NS	0.47[b]	NS	0.37[a]	0.83[a]	NS	0.81[c]	0.38[a]	0.82[a]

N.B. [a] $p < 0.05$; [b] < 0.001; [c] $p < 0.0001$; NS, not significant.

HR-MAS Spectroscopy of Human Intervertebral Disc Tissue Demonstrates the Lactate/N-Acetyl Ratio as a Potential Marker for Painful Degenerative Disc Disease

R. B. Iman[1], S. Hu[2], L. DeLosSantos[1], J. Claude[3], J. Peacock[3], S. Majumdar[1], and J. Kurhanewicz[1]

[1]Radiology, University of California, San Francisco, San Francisco, CA, United States, [2]Orthopaedic Surgery, University of California, San Francisco, San Francisco, CA, [3]NociMed, Redwood City, CA

Introduction

The clinical evaluation of low back pain is difficult. The intervertebral disc is thought to be a primary source of this pain. MR is useful for grade disc morphology, but not specific enough to identify painful discs because altered morphology does not necessarily equal painful discs. The current gold standard to determine the specific disc causing back pain is provocative discography and it is invasive, painful and has a positive predictive value of only 50-60%. (1) There is also a lack of objectivity in patient reported pain. There is currently no non-invasive marker for disc pain. The N-acetyl peak of proteoglycans (chondrointin sulfate, keratan sulfate, and heparan sulfate) is resolved at 2.04ppm and has been shown to decrease with disc degeneration. (2) Another published HRMAS disc study suggested that lactate and the proteoglycan N-acetyl levels could provide a quantitative method for identifying painful intervertebral discs. (3) However, this prior study did not compare patients with degenerated discs with and without pain, which is the critical clinical question, and the focus of the current study. To determine whether chemical biomarkers can discriminate painful from non-painful degenerated discs, *ex vivo* long echo-time ^{1}H high-resolution magic angle spinning (HR-MAS) spectroscopy data were acquired from patients with intervertebral disc tissue and correlated with a clinical assessment of pain.

Methods

Twenty-one intervertebral discs were surgically removed from 15 different patients with degenerated painful (N=12) and degenerated non-painful (N=9) diagnoses. The disc nucleus was pathologically separated from the annulus prior to the HR-MAS study. Discogenic pain patients were defined by a combination of pathologic findings on MRI and CT discography. In this abstract, the focus is on the chemical changes in the nuclear samples since in *in vivo* ^{1}H PRESS spectroscopic disc patient studies, the select volume is centered on the nucleus (4). Samples were weighed (mean 15.13 ± 7.98) and placed into custom designed 20 or 35 µl leak proof zirconium rotors containing 3.0 µl D_2O + 0.75% TSP. ^{1}H HR-MAS data were acquired at 11.7T, 1°C, and 2,250 Hz spin rate using a Varian INOVA spectrometer, equipped with a 4 mm gHX nanoprobe. A long echo time rotor synchronized Carr-Purcell-Meiboom-Gill (CPMG) sequence was acquired with 2s relaxation, 2s presaturation, 2s acquisition (TR = 6s), 40,000 points, 20,000 Hz spectral width, 144 echo time and 512 transients. The Electronic Reference To access In vivo Concentrations (ERETIC) (5) method was used as a quantitation standard. A student's T-test was performed to determine if there was a significant difference between the two groups of patients.

Results

Figure 1 shows representative 1D cpmg HR-MAS spectra of a) non-painful degenerative and b) painful degenerative intevetebral discs. T_2 filtered data was used in hopes of resolving the lactate doublet at 1.33ppm from lipids; however, as can be seen in the painful disc spectrum, residual lipid often remained prohibiting the accurate quantification of the lactate doublet in disc samples. However, the lactate quartet was well resolved and of a sufficient signal to noise ratio to robustly quantify lactate in cpmg spectra. Visually, both spectra demonstrate chemical changes typical of disc degeneration, including, an increase in resolution of the resonances in the carbohydrate region of the spectrum, decreased N-acetyl and increased lactate and alanine peaks. Important to the current study, there was a 2-fold higher mean lactate in painful vs. non-painful disc tissue, but due to the large variability of lactate measurements in both patient cohorts, the difference in lactate levels was not significant (4.14±4.72 vs. 2.17±1.11, p=0.19). Additionally the N-acetyl peak was not different between the painful and non-painful cohorts (23.65±27.05 vs. 17.74±8.17, p=0.49). The relative ratios of the lactate/N-acetyl are shown in figure 2 provide the best discrimination of painful from non-painful degenerated discs. The ratio in the painful discs (mean = 0.19 ± 0.08) was significantly higher than in non-painful discs (mean = 0.12 ± 0.03, p=0.02), however there was still overlap of the individual values.

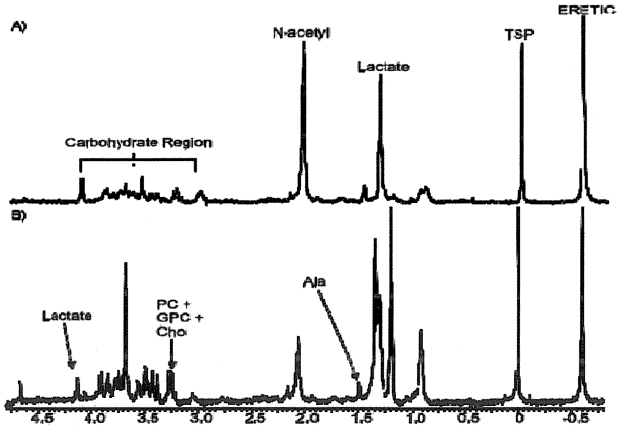

Figure 1: ^{1}H HR-MAS spectra of A) non-painful and B) painful degenerative intervertebral discs.

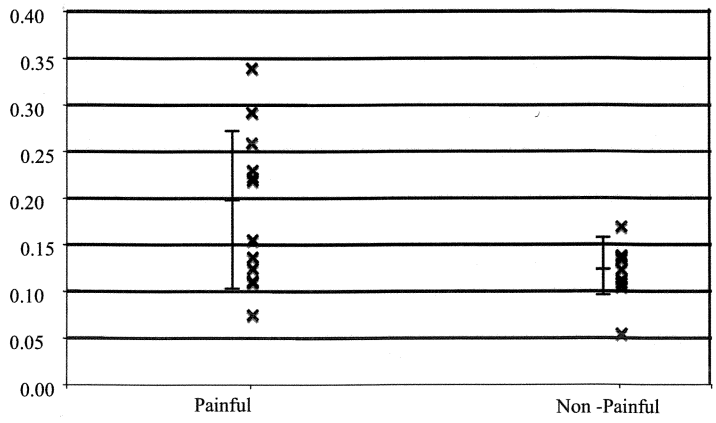

Figure 2: Lactate/N-acetyl ratio in painful and non-painful degenerative intervertebral disc.

Discussion and Conclusions

This study demonstrates that the lactate/N-acetyl ratio has potential for quantitatively discriminating painful from non-painful degenerated discs. However, overlap in the individual lactate/N-acetyl ratios warrants further study to understand whether the overlap is due to a true overlap in disc chemistry or insufficient clinical classification of pain. Additionally, the predictive ability of the lactate/N-acetyl ratio could be improved through the addition of other chemical markers such as water and lipid content as well as other imaging approaches, such as T1ρ.

References

1) Carragee EJ et al. Spine 2006;31(18):2115-2123; 2) Keshari KR et al. Spine 2005;30(23):2683-2688; 3) Keshari KR et al. Magn Reson Med 2005;53(3):519-527; 4) Zuo J et al, Magn Reson Med 2009;62(5):1140-1146; 5) Albers et al. Magn Reson Med 2009;61(3):525-532;

Association of Physical Activity with Focal Knee Lesions in Subjects with Risk Factors for Knee Osteoarthritis and Normal Controls - Data from the Osteoarthritis Initiative

A. Arulanandan, W. Virayavanich, L. Nardo, H. Alizai, T. Baum, G. B. Joseph and T.M. Link

Musculoskeletal and Quantitative Imaging Research, Department of Radiology and Biomedical Imaging, University of California San Francisco, 185 Berry Street, Suite 350, San Francisco, CA 94107, USA

Purpose:
To evaluate the association of physical activity with prevalence, incidence and progression of focal knee lesions over 36 months in subjects with risk factors for knee osteoarthritis (OA) and normal controls.

Materials and Methods:
Seventy-eight subjects (38 males, 40 females) with risk factors for knee OA were randomly selected for this study from the Osteoarthritis Initiative (OAI) incidence cohort. Additionally, 45 subjects (15 males, 30 females) with no risk factors for knee OA from the OAI control cohort were included. All subjects were 45-55 years old, had a BMI of 19-27 kg/m², had no knee pain in either knee (WOMAC pain score of zero) and had no radiographic OA (Kellgren-Lawrence score of zero). Subjects underwent 3T MRI of the right knee at baseline and after 36 months. MR images were assessed by three radiologists for the presence and severity of focal knee meniscal and cartilage lesions using the whole organ MRI score (WORMS). The Physical Activity Score for Elderly (PASE), which assesses leisure, household and occupational activities, was completed by all study participants at baseline, 12, 24 and 36-month follow-up. Multivariate regression models (adjusting for gender, age and BMI) were used to analyse the impact of OA risk factors and physical activity on prevalence, severity, incidence, and progression of focal knee lesions.

Results:
At baseline, meniscal lesions were prevalent in 46% of subjects with OA risk factors, as compared to 38% of controls. Similarly, cartilage lesions were prevalent in 47% of subjects with OA risk factors, as compared to 42% of controls. Incidental meniscal lesions during the 36 month follow-up were observed in 12% of the subjects with OA risk factors and in 11% of the normal controls. Incidental cartilage lesions were diagnosed in 6% of the subjects with OA risk factors, but in none of the normal controls. The prevalence and severity of both mensical and cartilage lesions were not significantly different between groups ($p>0.05$). However, higher PASE scores (averaged over 36 months) were significantly ($p<0.05$) associated with the baseline and 36 month follow-up prevalence and severity of meniscal and cartilage lesions in both groups. Subjects whose PASE scores increased over 36 months had a significantly ($p<0.05$) higher incidence and progression of meniscal and cartilage lesions over 36 months, independent of subject group.

Conclusion:
Middle-aged subjects with and without OA risk factors had a similar prevalence and severity of focal knee lesions. Higher physical activity scores were associated with higher prevalence and severity of focal knee lesions independent of subject group. Additionally, the incidence and progression of focal knee lesions were related to increasing PASE scores over 36 months.

Abnormal Tibiofemoral Kinematics Following ACL Reconstruction are Associated with Early Cartilage Matrix Degeneration Measured by MRI T1rho

[1,2]Bryan Haughom; [1,2]William Schairer; [2]Richard B Souza; [2]Dana Carpenter, [3]C Benjamin Ma, [2]Xiaojuan Li
University of California San Francisco [1]School of Medicine,[2] Department of Radiology, [3]Department of Orthopedic Surgery

Introduction: Previous large cohort studies suggested that subjects with anterior cruciate ligament (ACL) injury had a high risk of developing post-traumatic osteoarthritis, even after ACL reconstruction.Abnormal kinematics following ACL reconstruction are thought to contribute to cartilage damage by altering loading patterns in the reconstructed knee. Proving a connection between altered kinematics and the development of cartilage damage has proven difficult, as the latent period between surgical reconstruction and cartilage degeneration, as shown in radiographs, is long. We have developed MR methods to quantify knee kinematics and MR T1rho to detect early cartilage matrix degeneration prior to any morphological changes in the cartilage. Our study aimed to assess whether altered kinematics following ACL reconstruction are associated with early cartilage degeneration as measured by T1rho MRI.

Methods: Eleven patients (7 women and 4 men, age: 33 $\pm$ 9 years) underwent 3Tesla MR imaging 18 $\pm$ 5 months following ACL reconstruction using 8-channel knee coil. All patients were reconstructed using an anteromedial drilling technique. Images were obtained at knee extension and 30° flexion under simulated loading (125N), using an in-house developed loading device. Anterior tibial translation (ATT) and tibial rotation (TR) between flexion and extension, and T1rho relaxation times of the knee cartilage were quantified using sequences previously developed in our lab. The cartilage was divided into five compartments: medial and lateral femoral condyles (MFC/LFC), medial and lateral tibias (MT/LT), and patella. A sub-analysis of the weight-bearing (wb) region of the femoral condyles was also done. Percentage change in cartilage T1rho relaxation time was determined between the injured and uninjured knees across all compartments of the knee. Patients were categorized as having "abnormal" kinematics – either ATT or TR – if difference between knees for the kinematic variable in question was outside one standard deviation from the mean (defined as the group standard deviation of the contralateral healthy knees). Intra-subject differences were analyzed with paired t-tests, while inter-group differences were analyzed with unpaired t-tests.

Results: Seven patients were defined as having "restored" ATT, while only 3 had "restored" TR. There were statistically significant ($p=0.05$) percentage increases in the percentage change of the T1rho relaxation times of the MFC-wb, MT, patella and overall average cartilage in the "abnormal" ATT group. (Figure 1) No statistically significant differences between "restored" and "abnormal" TR groups were observed, however the percentage change of the MFC cartilage T1rho approached significance ($p = 0.08$).

Conclusions: Quantitative MRI allow us to detect early cartilage matrix damage in the ACL reconstructed population. Utilizing our novel loading device in conjunction with T1rho MRI, we were able to, for the first time, quantify the relationship between altered tibiofemoral kinematics and the development of cartilage degeneration. It appears as if kinematic changes, particularly in the anterior-posterior plane, following ACL reconstruction may predispose patients to cartilage matrix degeneration as early as 18 months following surgery. Our results may indicate that restoring native knee kinematics following ACL injury may prevent progression of cartilage damage.

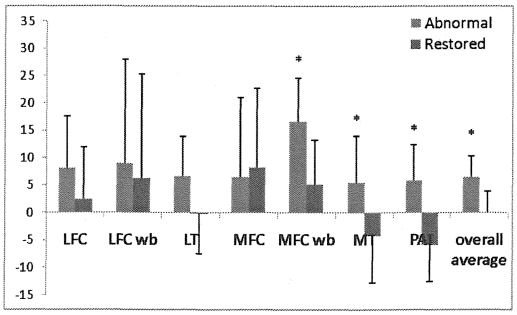

Figure 1 Percentage change of T1Rho relaxation times in patients with "abnormal" and "restored" ATT. Positive values imply greater T1ρ values in the injured knee.- * $p \leq 0.05$

Effects of Age and Sex on the Strength and Cortical Thickness of the Femoral Neck

R.Dana Carpenter[a]; S. Sigurdsson[b]; S. Zhao[a]; Y. Lu[c]; G. Eiriksdottir[b]; G. Sigurdsson[b,d,e]; B.Y. Jonsson[f]; S. Prevrhal[g]; T.B. Harris[h]; K. Siggeirsdottir[b]; V. Guðnason[b,e]; T.F. Lang[a]

[a]Department of Radiology and Biomedical Imaging, University of California, San Francisco; [b]Icelandic Heart Association; [c]Department of Health Research and Policy, Stanford University; [d]Landspitali-University Hospital, Reykjavik, Iceland; [e]University of Iceland; [f]Malmo University Hospital, Malmo, Sweden; [g]Philips Medical Systems, Inc.; [h]Intramural Research Program, National Institute on Aging

INTRODUCTION: The femoral neck, which connects the head and diaphysis of the femur, is one of the most common sites of hip fracture. In this study we used quantitative computed tomography (QCT) to investigate the effects of age and sex on femoral neck size, shape, cortical thickness, and strength. We also sought to determine whether a reduced reconstruction field of view centered on the hip offers a more detailed evaluation of femoral neck structure without increasing radiation dose to the subjects.

METHODS: A group of 48 men (22 aged 65-75 years, 26 aged 80-90 years) and 59 women (32 aged 65-75 years, 27 aged 80-90 years) enrolled in the Age, Gene/Environment Susceptibility-Reykjavik study were imaged with *in vivo* QCT. Imaging was performed with a scanning FOV of 500 mm, and images were reconstructed with a 500-mm FOV (0.98-mm voxels) and with a 200-mm FOV (0.39-mm voxels) centered on the left hip. The proximal femur was segmented from the surrounding soft tissue in both QCT images, and the images were reformatted in a standard reference frame based on anatomic landmarks. The femoral neck cross-section of minimum cross-sectional area (minCSA) was isolated for standard mechanical engineering beam analysis. Femoral neck cross-sectional moment of inertia (a measure of the spatial distribution of bone) was computed for bending directions near those experienced during daily activities like standing and walking (I_{AP}) and for bending directions not commonly experienced in daily life (I_{IS}). Bending strength (M_y) was averaged over 360 different bending directions, and axial compressive strength (F_y) was computed for a force applied along the long axis of the femoral neck. Cortical thickness in 8 octants equally spaced among the principal axes of the minCSA section was computed based on density profiles extending through the cortex. Generalized linear models accounting for height, weight, age group (younger or older), and sex were used to detect age- and sex-based differences in the least-square mean values of femoral neck size, shape, cortical thickness, and strength.

RESULTS: Men had a 46% higher M_y and a 23% higher F_y than women, while women had a 13% thicker inferior cortex than men. Cortical thickness did not correlate with bending or axial strength after adjusting for overall volumetric bone mineral density. Both minCSA and I_{AP} were higher in the older, gender-pooled age group, but F_y, M_y, and I_{IS} did not differ between the two age groups. The age-related difference in minCSA and sex-related difference in cortical thickness were only statistically significant for the reduced FOV (200-mm) images.

CONCLUSIONS: The results suggest that age-related expansion of the femoral neck primarily occurs in the superior and inferior directions and helps maintain homeostasis of femoral neck stiffness and strength. The higher bending strength of the male femoral neck may partly explain why elderly men have a lower risk of hip fracture than elderly women. Using a reduced FOV enhanced our ability to detect age- and sex-related differences without increasing radiation dose.

T_1 correction in multipeak T_2*-IDEAL gradient-echo imaging for the quantification of intermuscular adipose tissue

Dimitrios C. Karampinos[1], Huanzhou Yu[2], Ann Shimakawa[2], Thomas M. Link[1], Sharmila Majumdar[1]

[1]MQIR Group, Department of Radiology, University of California, San Francisco, CA, USA, [2]Applied Science Laboratory, GE Healthcare, Menlo Park, CA USA

Introduction: Intermuscular adipose tissue (IMAT) has been recently associated with different metabolic abnormalities including obesity and insulin resistance [1]. Chemical shift based water/fat separation, like iterative decomposition of water and fat with echo asymmetry and least-squares estimation (IDEAL) gradient-echo imaging, has been proposed for mapping the spatial distribution and quantifying the amount of IMAT [2-4]. An important confounding factor in the IDEAL-based quantification of the IMAT fat fraction is the large difference in T_1 between muscle and fat (1500 ms versus 360 ms at 3 T), which can cause significant overestimation in IDEAL-based fat fraction measurements [5,6]. T_1 unbiased estimation of the fat fraction is, in general, a problem involving both water/fat separation and T_1-correction. In the present work, different T_1-correction approaches in dual flip angle experiments are evaluated in terms of accuracy and noise performance.

Methods: T_1-bias minimization/correction can be performed following three approaches, depending on the selection of the two flip angles:

Equal small flip angles (ESFA) approach: the two flip angles are small, equal and selected so that both water and fat signals are T_1 independent (no T_1 estimation required).

Unequal large flip angles (ULFA) approach: the two flip angles are large and not equal (T_1 estimation is required).

Unequal small flip angles (USFA): the first flip angle is selected such that the water signal is T_1 independent and the second flip angle is selected so that the fat signal is T_1 independent (no T_1 estimation required.

Quantitative IDEAL measurements are performed on a water-fat phantom containing 28 vials with varying fat content and T_1 of water using an investigational version of multi-peak T_2* IDEAL [4]. The calf muscle region of a healthy volunteer is also scanned at 3 T. Both phantom and *in vivo* experiments are repeated multiple times to assess noise performance.

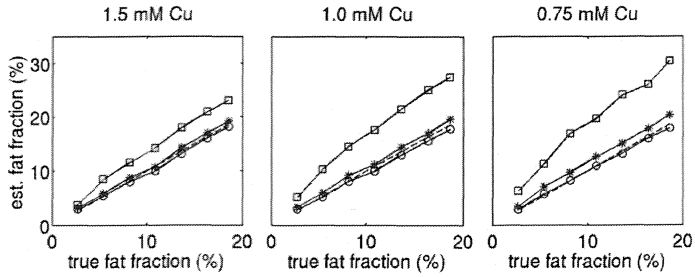

Fig. 1: T_1 bias effect on phantom results. Symbols represent different flip angles results. Squares correspond to 42°, stars to 11.6°, circles 3.7° and dashed line to nominal values.

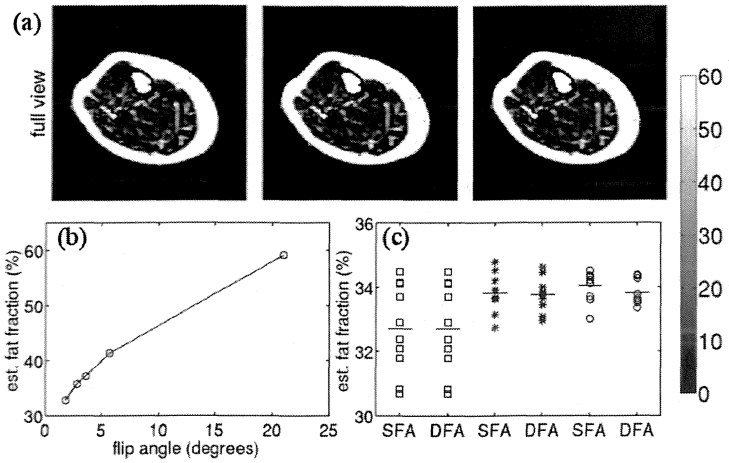

Fig. 2: *In vivo* results: (a) fat fraction maps, (b) T_1 bias effect on an ROI, (c) results of different T_1 correction approaches for multiple repetitions(squares represent ESFA, stars USFA and circles ULFA), .

Results and Discussion:

Fig. 1 shows that the T_1 bias effect is important in measurements of a phantom mimicking the T_1 range of the muscle. The use of USFA minimizes the standard deviation of fat fraction (results not shown). *In vivo* fat fraction measurements are also severely affected by the T_1 bias effect (results for a muscle ROI in Fig 2b). All three T_1 correction/minimization approaches lead to minimized T_1 bias effects. The USFA approach shows the lowest dispersion of the 10 repetitions of the same measurement around the corresponding mean values (Fig.2c).

Conclusion: The use of USFA approach minimizes the T_1 bias effect on quantitative chemical shift based water/fat separation with improved noise properties over the USFA and ULFA approaches.

References: [1] Gallagher et al, AJCN 81: 903-910, 2005, [2] Reeder et al, MRM 51: 35-45, 2004, [3] Wren et al, AJR 190: W8-W12, 2008, [4] Yu et al, MRM 60:1122-1134, 2008, [5] Liu et al, MRM 58: 354-364, 2007, [6] Bydder et al, MRI 26: 347-359, 2008.

Composition of osteoarthritic and osteoporotic femoral bone: a comparative FTIR study

Joyce Pang[1], Janina Patsch[2], Thomas Link[3], Sharmila Majumdar[3], Galateia Kazakia[3]

[1]Department of Molecular and Cell Biology, University of California, Berkeley; [2]Department of Radiology, Medical University of Vienna; [3]Department of Radiology and Biomedical Imaging, University of California, San Francisco

Introduction: Osteoarthritis (OA) and osteoporosis (OP) are serious musculoskeletal disorders highly prevalent in the aged population. OA, characterized by joint and cartilage degradation, is also known to cause remodeling and thickening of subchondral bone [1]. OP is defined by degradation of bone structure resulting in decreased bone mass and increased risk of fracture [2]. While these structural changes are well documented [3,4], compositional differences between OA and OP bone are as yet unclear, particularly at the femur, a common site of OA and OP pathology. The majority of studies on bone quality and composition have investigated these diseases individually, through analysis of remote iliac crest biopsies rather than tissue taken from the involved site. This study aims to compare OA and OP bone composition in samples obtained from hip arthroplasty surgery using Fourier Transform Infrared (FTIR) spectroscopy.

Methods: Trabecular bone specimens from the proximal femur of eleven OP patients with hip fractures and ten OA patients were obtained during total hip replacement surgery. Samples from 2 sites were obtained from each donor: 1) central in proximity to the femoral neck and 2) subchondral in the principal compressive region. All patients were male with a mean age of 70 years, no malignancies and no treatment in those with osteoporosis. Specimens were fixed and dehydrated in ethanol, then homogenized with potassium bromide to form a pellet for FTIR spectra acquisition. FTIR spectra were obtained using a benchtop interferometer system (Thermo Nicolet) at a spectral resolution of 4 cm^{-1}. The spectra were transferred to chemical imaging software (Isys) for analysis. Focusing on the amide I (1600-1700 cm^{-1}), phosphate (PO_4, 900-1200 cm^{-1}), and carbonate (CO_3^{2-}, 890-840 cm^{-1}) bands, spectra were baseline corrected. From the integrated areas, mineral:matrix (PO_4/amide I) and carbonate:phosphate (CO_3^{2-} / PO_4) ratios were determined. Additional peak heights were measured to calculate crystallinity (1030 cm^{-1}/1020 cm^{-1}) and crosslink ratio (1660 cm^{-1}/1690 cm^{-1}). Statistical comparisons were performed using paired t-tests or Wilcoxon signed-rank tests as needed.

Results: No significant differences between OP and OA femoral samples were found for the parameters measured from FTIR spectroscopy (Table 1). However, comparing the central site alone, OP bone trended towards lower mineral:matrix (24% lower though not significant at p=0.098). Within the OP specimens (Table 2), bone from the central site (close to the site of fracture) trended towards lower mineral:matrix (22% lower though not significant at p=0.098) and lower carbonate:phosphate (13% lower though not significant at p=0.082). This trend was not evident in the OA samples (Table 3).

Discussion: Our results suggest that regional variations in mineralization exist in OP but not in OA femoral bone. In OP samples, a trend towards decreased mineralization was found at the site of femoral neck fracture as compared to the subchondral region of the femoral head. This is consistent with previous work that found lower mineralization near the fracture site and differences between OA and OP at the site of fracture but not at remote donor sites [5]. The decreased phosphate and carbonate content is presumably related to imbalances in bone remodeling mechanisms, possibly forming immature, less mineralized bone tissue during disease progression prior to osteoporotic fracture.

Table 1. FTIR analysis results for osteoarthritis and osteoporosis femoral bone samples

	OA (n=10)	OP (n=11)	p-value
mineral:matrix	5.47 ± 0.51	4.99 ± 0.86	0.14
carbonate:phosphate	0.0157 ± 0.002	0.0167 ± 0.002	0.21
crystallinity	1.01 ± 0.02	1.01 ± 0.02	0.96
crosslink ratio	1.36 ± 0.09	1.35 ± 0.06	0.75

Table 2. FTIR analysis results for osteoporosis samples grouped by location

	central (n=11)	subchondral (n=11)	p-value
mineral:matrix	4.43 ± 1.70	5.54 ± 0.86	0.09
carbonate:phosphate	0.0156 ± 0.003	0.0178 ± 0.002	0.08
crystallinity	1.02 ± 0.03	1.01 ± 0.02	0.31
crosslink ratio	1.36 ± 0.09	1.34 ± 0.10	0.32

Table 3. FTIR analysis results for osteoarthritis samples grouped by location

	central (n=11)	subchondral (n=11)	p-value
mineral:matrix	5.65 ± 0.71	5.29 ± 0.82	0.28
carbonate:phosphate	0.0153 ± 0.003	0.0161 ± 0.003	0.77
crystallinity	1.02 ± 0.02	1.01 ± 0.02	0.30
crosslink ratio	1.41 ± 0.097	1.31 ± 0.14	0.13

References: [1]Goldring et al, JCellPhysiol 2007 [2]Cummings et al, Lancet 2002 [3]Blain et al., Bone 2008 [4]Fazzalari et al, Bone 1992 [5]McCreadie et al, Bone 2006

Relationship between Biomechanics and the Composition of Articular Cartilage – Preliminary Findings

[1,2]Fang C, [1,3]Charette K, [1]Gilleran T, [1]Wu S, [1]Luke A, [1]Li X, [1]Majumdar S, [1]Souza RB
[1]Radiology and Biomedical Imaging, University of California San Francisco, San Francisco, CA.
[3]University of California Berkeley, Berkeley, CA. [3]Bay School of San Francisco, San Francisco, CA.
charlesfang@berkeley.edu

INTRODUCTION: Knee osteoarthritis (OA) is a degenerative joint disease affecting cartilage. Although the current understanding of the progression of OA is poor, previous studies suggested that abnormal loading sets off a destructive cycle of damage and shear, and that the external knee adduction moment is of particular importance in the development of OA. Using quantitative magnetic resonance imaging and motion capture, we can assess how the biochemical state of the cartilage is affected by the differences in loading patterns across individuals. The aim of this study, therefore, was to demonstrate a relationship between knee kinetic parameters and the corresponding T1ρ and T2 times. We hypothesized that we would see an increase in T1ρ and T2 values with increased average and peak knee moments.

METHODS: A total of 8 healthy subjects (4 male, 4 female, mean age = 20.8 ± 1.75 years, mean weight = 63.7 ± 13.3 kg, mean height = 1.69 ± 0.07 m) were recruited from the UCSF student population. These subjects were studied using a 3 T GE Signa MRI scanner and an 8-channel phased-array knee coil. The imaging protocol contained sequences for cartilage morphology and 3D quantitative T1ρ and T2 mapping. These images were post-processed with in-house software to identify and quantify the medial and lateral compartments of the cartilage. A medial-to-lateral ratio for both T1ρ and T2 was computed to explore the differences in biochemistry within a single individual. Subjects were also examined using a ten-camera infrared VICON motion capture system with a set of lower body markers. Motion capture of the subjects doing one leg hops at 100 BPM on each side were obtained. Net knee moments were calculated using standard inverse dynamics equations in Visual3D software. Relationships were computed in SPSS software using Pearson's Correlations Coefficients.

RESULTS: Images of 8 left knees and 6 right knees were ultimately collected. Average T1ρ = 37.0 ± 3.45 ms, average T2 = 27.6 ± 2.48 ms over all components. Peak flexion, adduction, and internal rotation moments (Nm/kg) are, respectively, 2.85 ± 0.65, 0.75 ±0.40, and 0.68 ± 0.27.

R values (n=14)	Peak Flexion	Peak Adduction	Peak Internal Rotation
T1ρ Lateral	0.314	0.240	-0.066
T1ρ Medial	-0.067	0.469*	0.086
T1ρ M/L	-0.592*	0.359	0.249

Figure 1: Pearson's Correlation coefficients of knee moments against T1ρ relaxation times. * denotes significance at $p < 0.05$

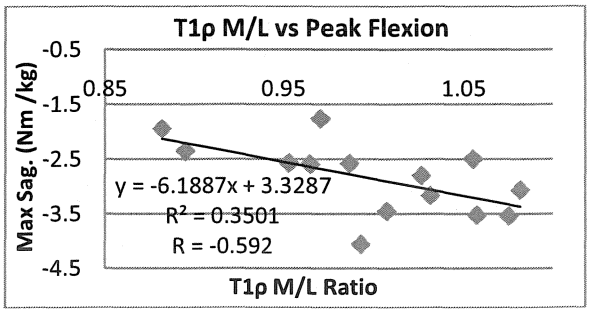

Figure 2: Relationship between peak flexion moments and T1ρ M/L Ratio. Extension moments are (+), Flexion moments are (-)

CONCLUSION: These preliminary results are consistent with our hypothesis, which suggested that higher loads placed on cartilage directly affect the biochemistry of the cartilage, elevating T1ρ values. Even in healthy individuals, it seems that the cartilage is responsive to changes in loading patterns. More work is necessary to confirm these relationships with larger sample sizes and additional exercises.

IMAGING MMP EXPRESSIONS AND PROTEOGLYCANS IN HUMAN OSTEOARTHRITIC KNEE

David C. Miller, Joseph Schooler, Hilla Wahnishe, Sarmad Siddiqui, Xiaojuan Li, Sharmila Majumdar and Ella F. Jones

Background: Osteoarthritis (OA) is the most common form of arthritis. Owing to the lack of sensitivity and specificity, standard magnetic resonance (MR) or computed tomography (CT) imaging techniques have met with difficulties to detect early biochemical events that lead to cartilage degeneration. More recently, $T_{1\rho}$ relaxation mapping by MR has been proposed to detect the loss of proteoglycan (PG) macromolecules at early stages of OA. Although such clinical technique has shown great promises for measurements of macromolecular changes in early cartilage failure, the direct link from the earliest pathological signaling pathway to the change of macromolecules that leads to structural and functional degradation is still missing. Matrix metalloproteinases (MMPs) are known to be involved in early events of arthritic diseases. In particular, active MMP-9 and -13 are key enzymes that are responsible for the degradation of collagens and PG at early stages of OA. In this work, we successfully demonstrate the utility of optical and MR imaging to account for the MMP activities and their correlation with PG content in knee specimens from OA patients. **Methods**: Human femoral condyles were collected from patients diagnosed with severe osteoarthritis during total knee replacement surgeries at the UCSF Dept. of Orthopedic Surgery. Specimens were immediately placed in specimen cups and frozen at -80 °C. For imaging, specimens were thawed overnight and incubated in 0.2 μM of MMPSense680 and incubated in the dark at 37 °C for 2 h. The specimens were removed and washed with PBS followed by optical imaging and histology. The corresponding $T_{1\rho}$ MR measurements were collected from a 3T whole body MR scanner using spin-lock techniques and an SPGR image acquisition. **Results**: All osteoarthritic knee specimens showed intense signal for MMP activities after 2 h incubation. The corresponding $T_{1\rho}$ values were in the range of 48 to 75 ms indicating a severe loss of PG macromolecules and cartilage degeneration (Figure 1). The overall MMP activity measured by optical imaging (normalized in efficiency) directly correlates to the $T_{1\rho}$ measurements, showing high MMP activities in specimens with severe loss of PG (Figure 2). **Conclusion**: We have successfully demonstrated the upregulation of MMP expressions in OA cartilage from knee specimens in patients. Through the combination of optical and MR imaging, we have now established the correlation of the upstream MMP molecular events to the downstream macromolecular PG changes that ultimately lead to the degradation of cartilage integrity in OA patients.

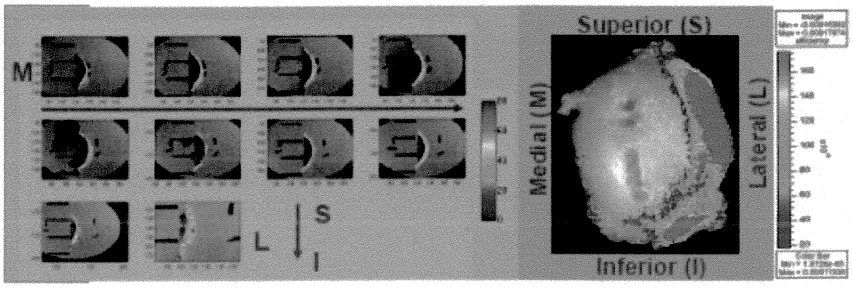

Figure 1. *A representative image of T1p mapping (left) by MR and MMP expression detection by optical (right).* Left: T1p map of a human medial posterior femoral condyle specimen imaged from medially to laterally. Cartilage T1p relaxation times, in miliseconds, are overlaid with a color scale for visualization. Right: A femoral condyle was treated with MMPSense and examined by reflectance optical imaging. The optical signal was normalized against the background. Signals observed here indicate a high expression of MMP-9/-13 in the lateral posterior and lateral inferior compartments.

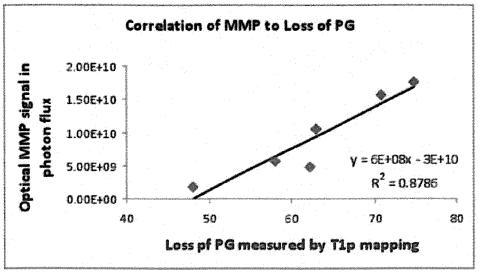

Figure 2. MMP expression measured by optical imaging was correlated with the loss of PG content measured by MR T1ρ mapping. Five different samples were plot using a linear regression model. Results shown here indicate there is a positive correlation of MMP and PG depletion and the R^2 value at 85%.

Linking Gene Expression and Biochemical Composition Changes Using HR-MAS Spectroscopy in Human Osteoarthritic Cartilage

Kimberly Loo[1,2], Sarmad Siddiqui[2], Emily Chin[3], Tamara Alliston, Ph.D.[3], John Kurhanewicz Ph.D.[2], Michael Reis, M.D.[3], Xiaojuan Li, Ph.D.[2]

[1]University of California, Los Angeles (UCLA), CA [2]Department of Radiology and Biomedical Imaging, University of California, San Francisco (UCSF), CA, [3]Department of Orthopaedic Surgery, UCSF, CA
lookimberly@ucla.edu

Introduction:
Osteoarthritis (OA) is a disease characterized by the degradation of hyaline articular cartilage. The procedure has shown to be involved with complex degradation in extracellular matrix, and alterations in metabolism and gene expression profiles of chondrocytes. Our long term research goal is to explore the potential link between MR measures and cartilage molecular and genetic activities during the disease. Such correlative data will provide a better understanding of pathophysiology of OA, and to improve the non-invasive diagnosis and treatment monitoring of OA using *in vivo* MR techniques. Towards this goal, High Resolution Magic Angle Spinning (HR-MAS) NMR spectroscopy was used in this project. HRMAS spectroscopy is ideal for analyzing intact tissue samples as it provides spectral resolutions comparable to that of tissue extract solutions while maintaining tissue integrity for downstream applications. The aim of this study is to 1) examine the impact of HRMAS experiment on mRNA integrity of human cartilage tissue, and 2) correlate HR-MAS findings of human cartilage with gene expression, particularly the expressions of collagen 2, aggrecanase, and matrix metallopeptidase (MMP) 13 which were quantified using quantitative real time polymerase chain reaction (qRT-PCR).

Methods:
Cartilage punches were acquired from total knee arthroscopy (TKA) surgeries (n=18). Following extraction, samples were frozen immediately until RNA extraction or HR-MAS spectroscopy experiment. Fifteen samples were analyzed directly for RNA extraction, and three samples were analyzed for HR-MAS immediately followed by RNA extraction. The HRMAS spectra was acquired at 500 MHz using a CPMG sequence at temperature =1°C, spin rate = 2250 Hz, and acquisition time = 144 ms. For mRNA quantification, the punches were extracted and homogenized with a Trizol reagent (Invitrogen). The aqueous phase of the homogenate was mixed with 70% ethanol and the RNA was then isolated using the PureLink Micro-to-Midi Total RNA purification System kit (Invitrogen) and treated with DNAse (Invitrogen). A 260/280 test was performed on the samples for examining mRNA purity using the Micro-Volume UV-Vis Spectrophotometer Nanodrop 2000 (Thermo Fisher Scientific). RNA was converted to cDNA using the QuantiTech Reverse Transcription Procedure (Qiagen). qRT-PCR was performed using SYBR Green master mix protocol.

Results:
The 260/280 ratios of punches underwent direct RNA extraction ranged from 1.41 to 1.5 whereas the 260/280 ratios of punches that underwent HR-MAS then RNA extraction ranged from 1.39 to 1.46. The fold calculations of the qRT-PCR data showed an up regulation of collagen 2 and MMP13 in OA punches compared to the control cartilage (Fig.1).

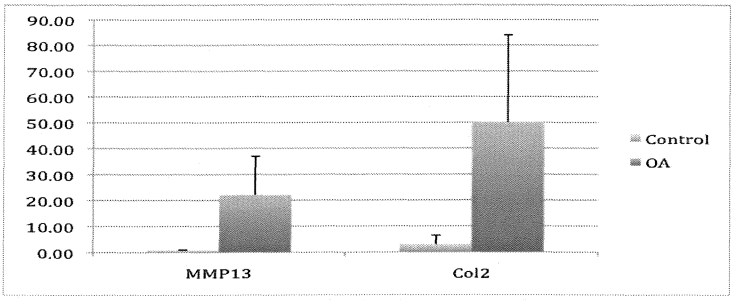

Fig.1: Collagen 2 and MMP 13 fold change of gene expression.

Discussion:
Our results suggested MMP13 and collagen 2 were up-regulated with OA, consistent with previous literature. The comparable 260/280 ratios suggested that HR-MAS does not significantly disrupt the integrity of such genes in OA cartilage. On-going work includes conducting experiments with larger sample size and examining correlation between HR-MAS data and gene expression,

Acknowledgement The work was supported by NIH R21056773.

Non-invasive Protein Synthesis Rate Determination in Skeletal Muscle following Unilateral Exercise via Dynamic PET/CT with L-[methyl-^{11}C]methionine

R. Harnish; T. Streeper; I. Saeed; M. Pampaloni; H. Vanbrocklin; N. Nguyen; R. Hawkins; S. Danoon; J. Slater; J. Blecha; C. Schreck; T. Lang

INTRODUCTION: Skeletal muscle is subject to a continual balance between protein synthesis and degradation. Age- and disease-related changes in this balance are reflected in the kinetics of amino acid incorporation into skeletal muscle, which is normally studied using invasive and painful biopsy techniques. Building on work done by Fischman et al (Proc. Natl. Acad. Sci. USA 95 (1998)), we employ dynamic PET to estimate the rate of incorporation of L-[methyl-11C]methionine into skeletal muscle, using a modern volumetric PET/CT scanner to quantify the distribution of 11C-MET uptake in a large volume of thigh muscle. To reduce subject discomfort associated with obtaining the radial arterial input function often used with kinetic studies, we have employed a method to acquire an image derived input function (IDIF) from dynamic ROI analysis of the femoral arteries. Finally, to determine whether 11C-MET kinetics were responsive to a physiologic stimulus, we imaged after acute unilateral exercise, hypothesizing increased uptake in the exercised vs. the controlled limb.

METHODS: One male and five female subjects performed isokinetic knee extension of the right leg, activating the thigh muscles. After 2 ± 1 hours, subjects were injected with 10-25 mCi 11C-MET solution, and imaged using a dynamic PET protocol. To obtain the IDIF, early time-frames of the dynamic PET image were used to segment the femoral arteries and surrounding tissue. IDIFs were obtained by superposition of time activity curves (TACs) in the arteries and surrounding tissue, which were combined so as to correct for partial volume errors due to scanner resolution. Skeletal muscle TACs were defined by ROIs placed on the quadriceps muscle in the exercised leg in each frame. Image data were analyzed according to a three compartment model. For each subject the IDIF and TAC were used to derive a Patlak plot (Figure-1), in which the slope K represented the proportion of 11C-MET incorporated into the bound skeletal muscle compartment. To validate the IDIF against blood sampling, we measured a radial artery input function in the male subject (Figure-1).

RESULTS: Among female subjects imaged 2-3 hours after exercise, we obtained a lumped constant, proportional to PSR, of K = 0.017 ± 0.008 vs. Fischman's K = 0.018 ± 0.005, and observed no distinct enhancement of uptake in the exercised limb. The subject that was exercised 1 hour before imaging did show enhancement (K = 0.041) in the exercised limb (Figure-2).

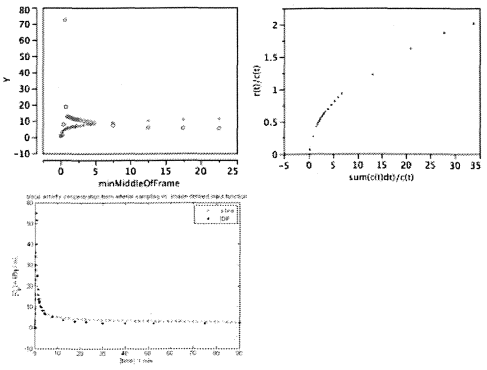

Figure 1 Top-Left: IDIF(red) and TAC(blue) for one subject. Top-Right: Patlak-curve. Bottom: IDIF vs. radial-arterial-input-function

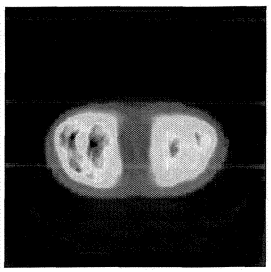

Figure 2

CONCLUSIONS: 11C-MET has excellent uptake in muscle, confirming earlier work. Our results were consistent with earlier studies, and our initial findings indicate that the kinetics of 11C-MET uptake in muscle may favor imaging subjects one hour after exercise, compared to 2-3 hours as observed in biopsy studies using other labeled amino acids.

The Spatial Distribution of Cartilage MR T_2 in a Subset of the Incidence and Control Cohorts of the Osteoarthritis Initiative

G. B. Joseph[1], T. Baum[1], C. Stehling[1], J. Carballido-Gamio[1], M. C. Nevitt[2], J. Lynch[2], C. E. McCulloch[2], S. Majumdar[1], Thomas M. Link[1],

[1]Musculoskeletal and Quantitative Imaging Research, Department of Radiology and Biomedical Imaging, UCSF
[2]Department of Epidemiology and Biostatistics, UCSF

Purpose:
The Osteoarthritis Initiative (OAI) is a multi-center, longitudinal study aimed at assessing biomarkers in osteoarthritis (OA) including those derived from magnetic resonance (MR) imaging. The purpose of this study is to compare the spatial distribution of cartilage MR T_2 between a subset of patients from the control and incidence cohorts of the OAI, using grey level co-occurrence matrix (GLCM) texture parameters.

Methods:
Equal sized (n=57) samples of subjects from the incidence and control cohorts of the OAI were included in this study based on the following inclusion criteria: (1) age range 45-55 years (2) body mass index (BMI) of 19-27 kg/m^2 and (3) Western Ontario and McMaster University (WOMAC) pain score of zero at the time of magnetic resonance (MR) imaging. Subjects from the incidence cohort did not have symptomatic knee OA, but had risk factors for OA, such as knee surgery or previous injury. Subjects from the control cohort had neither knee symptoms nor risk factors for OA. MR sagittal 2D MSME (TR = 2700 ms, TE_1-TE_7 = 10-70 ms) images were used to calculate T_2 relaxation time using 6 echoes (TE = 20-70) and 3 parameter fittings accounting for noise. Articular cartilage was segmented into four compartments: medial/lateral femur/tibia. Mean cartilage T_2 as well as a GLCM (which quantifies the spatial distribution of cartilage T_2 values), were calculated for each compartment. GLCM texture parameters including entropy, contrast, and angular second moment (ASM) were calculated at 0 degrees 45 degrees, 90 degrees, and at 135 degrees, with 1 pixel offset. Differences in cartilage mean cartilage T_2 and GLCM texture parameters were assessed between control and incidence groups using regression models adjusted for BMI and age.

Results:
Subjects from the incidence cohort had significantly ($p < 0.05$) elevated mean cartilage T_2 (medial femur, medial tibia), elevated GLCM-contrast (medial tibia), elevated GLCM-entropy (medial femur), and decreased GLCM-ASM (medial femur), compared to control subjects. Of all compartments, mean T_2 was greatest in the medial femur (mean T_2 incidence cohort = 37.74±2.28 ms, mean T_2 control cohort = 36.90±2.18 ms) and lowest in the lateral tibia (mean T_2 incidence cohort = 28.20±1.75 ms, mean T_2 control cohort = 28.08±1.83 ms).

Conclusions:
This study evaluated mean T_2 values as well as the spatial distribution of cartilage T_2 using GLCM texture analysis. The results indicate that both mean and spatial distribution of cartilage T_2 values differ between subjects in the incidence and controls cohorts of the OAI, in particular in the medial femoral condyle. Subjects at risk for OA not only have elevated mean T_2, but also have a more heterogeneous distribution of T_2 pixel values. While both subject cohorts were asymptomatic, their cartilage biochemical compositions (as assessed by cartilage T_2 parameters) differed. These results suggest that GLCM texture analysis supplements the standard measurements of mean T_2 and may aid in the detection of early OA.

Perfusion abnormalities of bone marrow edema-like lesions in knees with anterior cruciate ligament injury using dynamic contrast-enhanced MRI

Jin Zuo, Sharmila Majumdar, Xiaojuan Li
Musculoskeletal Quantitative Imaging Research, UCSF

Introduction Anterior cruciate ligament (ACL) tear is a risk factor of post-traumatic osteoarthritis (OA) [1]. The disease is frequently associated with bone marrow edema-like (BMEL) lesions which have been associated with disease progression and pain in OA. The aim of this study is to apply DCE MRI to evaluate bone marrow perfusion in patients with ACL tears, and to compare the perfusion patterns between BMEL region and normal appearing bone marrow region (NBM).

Method MR images were acquired on a GE 3T MR scanner with a quadrature knee coil. Seven subjects were studied: 5 patients had acute ACL injury and were scanned; one patient had chronic non-operative ACL tear and 1 healthy control. The imaging protocols included sagittal FSE T2-weighted images with fat saturation for evaluating BMEL (TR/TE = 3700/43ms). For DCE-MRI, a bolus of 0.1 mmol/kg body weight Gd-DTPA was administered. T1-weighted SPGR sequences were scanned before and during contrast agent administration (TR/TE = 8/3ms, temporal resolution = 10s, time points =50). BME was segmented from T2-weighted images. Signal intensity changes of BMEL to normal bone marrow were calculated. Based on the signal-time curve obtained from DCE-MRI, peak time, peak value (normalized to baseline signal intensity) and slope of the enhancement were quantified for each pixel [2]. The region of interest (ROI) of BME was later overlaid to the perfusion map after registration. The average parameter was calculated within BMEL and within NBM.

Results Six BMELs were found in acute ACL injured knees. No BMELs were found at 1-year follow up. No BMELs were found in the patient with chronic ACL tear and in healthy controls. Figure A shows T2-FSE images for a ACL-injured knee with BME (red ROI) and NBM (blue ROI) in the same compartment; Representative time signal intensity curves (normalized to baseline signal) from BMEL and normal bone marrow in acute ACL-injured knee, normal appearing bone marrow in non-operative chronic ACL-injured knee and control knee are plotted in Fig. B. The normalized signal intensity in the BMEL showed a significant increase compared with NBM, chronic ACL and control subjects. Significant differences were observed between BMEL and NBM for peak value (P =0.003) and slope (P=0.015). No significant differences (P=0.09) were found for peak time between the two groups (Fig. C).

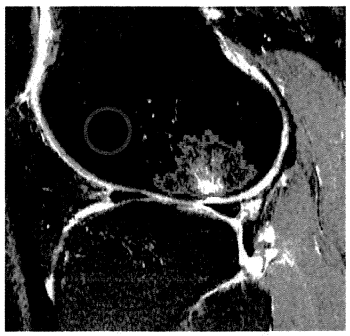

A

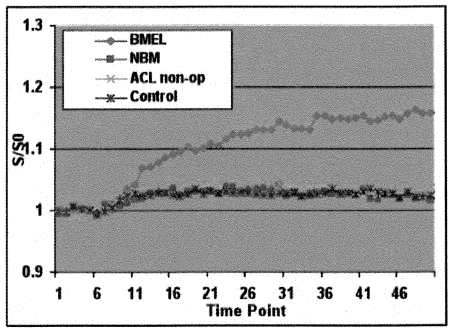

B

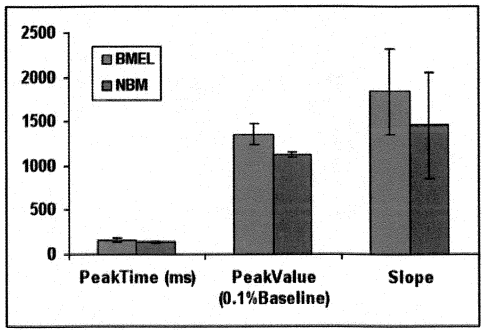

C

Discussion BMEL lesion was evaluated with DCE MRI and depicted different intensity curve compared with normal appearing bone marrow. Peak value and slope indicated significant differences between these two groups, suggesting that these two parameters may be useful biomarkers for the early diagnosis of bone perfusion abnormality. Quantifying perfusion parameters within bone marrow and subchondral bone in acutely-injured knees may identify risk factors for post-traumatic OA development.

Funded by: NIH K25 AR053633 and UCSF REAC.

References [1] Lohmander et al. Arthritis Rheum 50:3145-52. [2] Noworolski et al. MRM 53:249- 55.

QUANTITATIVE IN VIVO HR-PQCT IMAGING OF 3D RADIOCARPAL AND METACARPOPHALANGEAL JOINT SPACE DISTANCES IN RHEUMATOID ARTHRITIS

Andrew J. Burghardt[1], Christina Kurhanewicz[1], John B. Imboden[2], Sharmila Majumdar[1], Thomas M. Link[1], Xiaojuan Li[1]

[1] Musculoskeletal Quantitative Imaging Research Group, Department of Radiology and Biomedical Imaging, University of California, San Francisco; San Francisco, CA USA

[2] Department of Medicine, University of California, San Francisco and Division of Rheumatology, San Francisco General Hospital; San Francisco, CA USA

Purpose: In this technique development study, high-resolution peripheral quantitative computed tomography (HR-pQCT) was applied to non-invasively image the radioulnar (RU), radiocarpal (RC) and metacarpophalangeal (MCP) joints of patients with established rheumatoid arthritis (RA). Automated image processing methods were developed to quantify 3D MCP joint space morphology.

Methods: HR-pQCT imaging (82μm isotropic resolution) of the dominant hand was performed in patients with diagnosed rheumatoid arthritis (RA, N=7, age:54±14) and young healthy controls (CTRL, N=2, age:36±17). An automated segmentation technique was developed to individually segment the articulating joint space in the RU, two RC, and the 2nd to 4th MCP joints. The 3D distance transformation approach was applied to spatially map joint space distance and was summarized by the mean joint space distance (JSD) and standard deviation (JSD.SD) – a measure of joint space heterogeneity. The *in vivo* precision for each measure was characterized using root mean square coefficient of variation (RMSCV%) from repeat acquisitions performed on two RA patients.

Results: The *in vivo* reproducibility was high for JSD (RMSCV: 1.3%) and moderate for JSD.SD (RMSCV: 9.4%) despite one repeat measure with substantial motion artifacts. Qualitatively, the HR-pQCT images and pseudo-color JSD maps showed global joint space narrowing as well as focal defects in RA patients compared to CTRL (Fig 1).

In a modest number of subjects there was a general trend for decreased JSD at the MCP and comparable or greater JSD at the radial joints in RA subjects compared to CTRL. Joint space heterogeneity (JSD.SD) all tended to be greater in RA patients compared to CTRL (Fig 2).

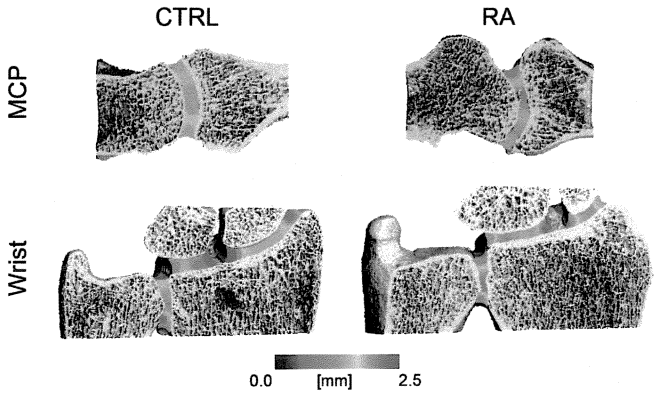

Figure 1: 3D pseudo-color JSD maps for the MCP (top) and radius (bottom)

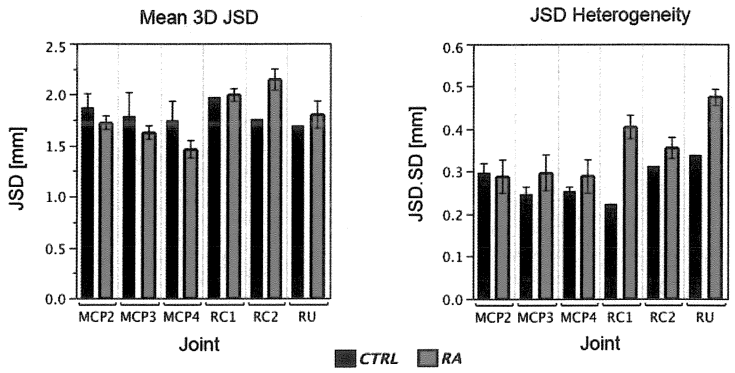

Figure 2: 3D Joint space distance (left) and joint space heterogeneity (right)

Conclusions: This study has established the feasibility of *in vivo* quantification of 3D joint space morphology in RA using HR-pQCT. This technology has the potential to provide a highly resolved, longitudinal assessment of joint morphology, which could provide new insights into clinical research studies of early disease progression and the efficacy of therapeutic interventions.

Title: Bone Structure Changes in Hypertensive Rats using MicroCT Imaging

Authors: Bryan J Hermannsson[1], Andrew J Burghardt[1], Youngho Seo[1], Sharmila Majumdar[1], Kathleen Brennan[2], Grant T Gullberg[2,1]

1. Radiology, University of California San Francisco, San Francisco, CA, USA
2. Radiotracer Development & Imaging Technology, Lawrence Berkeley National Laboratory, Berkeley, CA, USA.

Abstract Body:

Purpose: The goal of this project is to quantify the effects of hypertension on bone quality and structure using microCT imaging techniques.

Materials and Methods: For this study, we used 8 spontaneous hypertensive rats (SHR), born with high blood pressure, and 4 age-matched Wistar Kyoto (WKY) rats as controls. Ages ranged from 16 to 18 months. The left tibia from each specimen were excised and imaged in a 3mm section at the proximal metaphysis using a desktop microCT system (μCT-40, Scano Medical) at 8 μm- isotropic resolution. Trabecular and cortical regions of interest (ROI) were drawn semi-manually for each specimen, starting adjacent to the proximal growth plate and extending distally 250 slices (2 mm). Trabecular and cortical morphological parameters were calculated from binary images created by applying a single grayscale threshold visually selected to best represent all ranges of bone structure in all specimens.

Results: Overall tibial trabecular bone structure was robust in SHR specimens, while cortical bone was compromised as compared with the WKY controls. As seen in Fig 1, the SHR group was found to have statistically significant greater BV/TV, Tb.N, and lower Tb.Sp. In contrast they showed a significantly lower Ct.Th and Ct.TMD.

Conclusions: Despite their poor cardiovascular health, SHRs were found to have trabecular bone structure normally associated with greater bone strength. However, the higher trabecular bone volume was offset by cortical bone deficits, which likely resulted in altered load distribution and may lead to compromised bending strength. A decrease in the load-bearing cortical bone often results in an increase of trabeculae to compensate for the loss.

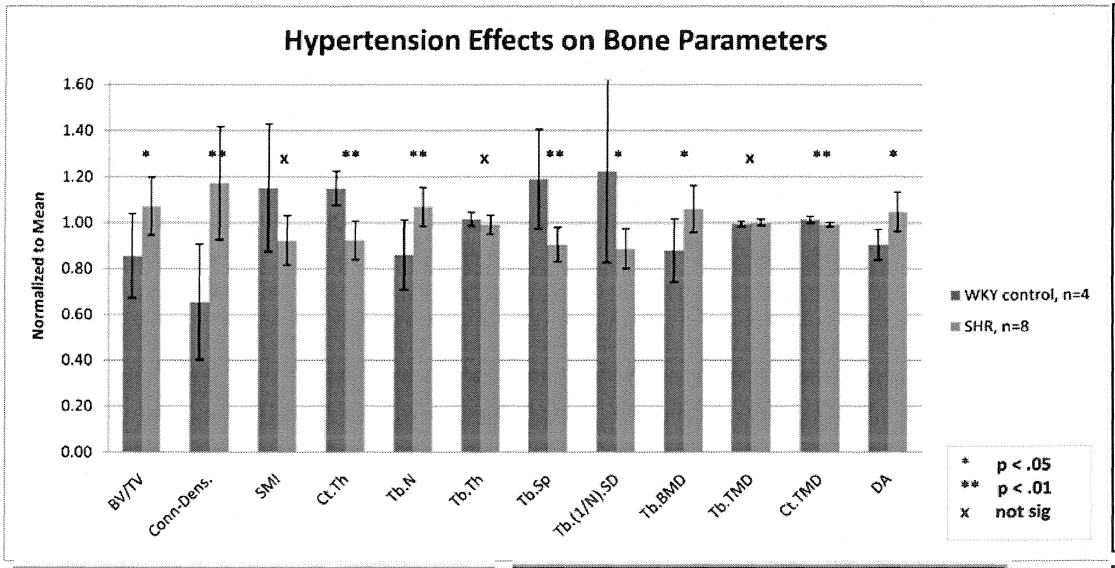

Fig 1: Bars show the bone parameter changes in hypertensive rats. Values are normalized to the mean to show changes. Error bars show ± 1 StDev.

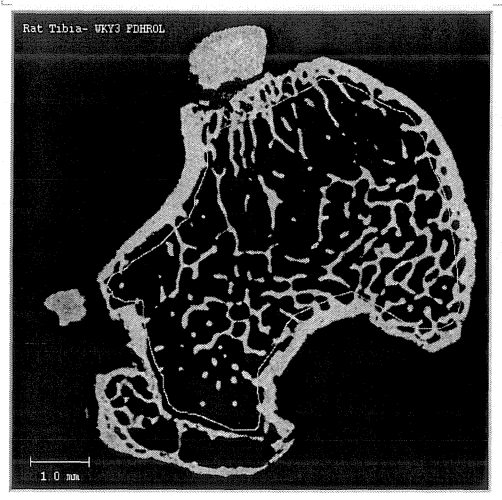

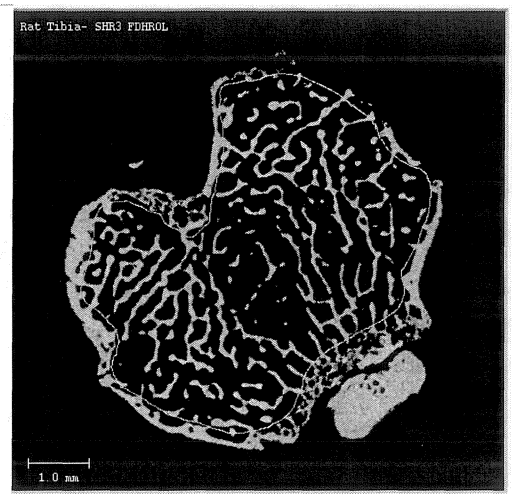

Fig 2: Slice matched microCT images. Green line indicates trabecular ROI.

Fig 2a: WKY control, low Tb.N, high Ct.Th

Fig 3a: SHR, high Tb.N, low Ct.Th

Clinical Utility of Magnetic Resonance Neurography of the Ulnar Nerve at the Elbow

Nayela Keen, MD, Cynthia Chin, MD, John Engstrom, MD, David Saloner, PhD, Lynne Steinbach, MD

Purpose. Focal ulnar nerve dysfunction at the elbow is a frequent clinical problem, and early diagnosis with clinical examination and electrophysiological studies is limited. Magnetic resonance (MR) neurography is an imaging study tailored to examine peripheral nerves and is a potentially useful new diagnostic tool in the evaluation of ulnar neuropathy at the elbow. The current study assessed the value of MR neurography as a diagnostic test for ulnar neuropathy at the elbow.

Materials and Methods. MR neurograms of the ulnar nerve at the elbow were performed on 21 patients with signs and symptoms of ulnar nerve dysfunction as evaluated by a neurologist. These findings were compared with MR neurograms of the elbow of 10 normal volunteers. Symptomatic and normal elbows were imaged in the supine position in a small extremity coil on one of three 1.5 T MR units. The sensitivity, specificity, and accuracy of MR neurography in detecting ulnar nerve abnormality were determined.

Results. For average ulnar nerve size, median latencies in the symptomatic and normal groups were 0.11 cm^2 and 0.06 cm^2 respectively; the distributions in the two groups differed with high statistical significance (Mann–Whitney $U = 190.5$, $n_1 = 21$, $n_2 = 10$, $P < 0.001$ two-tailed). For relative signal intensity, median latencies in the symptomatic and normal groups were 2.2 and 1.4 respectively; the distributions in the two groups differed significantly (Mann–Whitney $U = 167$, $n_1 = 21$, $n_2 = 10$, $P < 0.01$ two-tailed). When using a size cutoff of 0.08 cm^2 for a positive test, sensitivity was 95%, specificity was 80%, and accuracy was 90%. At this size, MR neurography demonstrated a positive correlation with EMG results in eleven of thirteen symptomatic patients.

Conclusions. Ulnar nerve size and relative signal intensity were greater in patients with symptoms of ulnar nerve dysfunction than in the normal volunteers. MR neurography of the elbow correlates well with symptoms and EMG findings related to ulnar neuropathy in the elbow region. It is a useful diagnostic test for evaluation of ulnar nerve dysfunction at the elbow.

Co-Analysis of Structural Imaging and DTI in Alzheimer's Disease

V.A. Cardenas, D. Tosun, N. Schuff, and M.W.Weiner

Introduction

Our current implementation of nonlinear registration of structural images uses T1-weighted images with uniform contrast white matter, and therefore voxel-wise analyses of structural changes may be insensitive to disease-effects within the white matter. To address this limitation, we proposed a deformation morphometry co-analysis with diffusion tensor imaging (DTI), which provides good imaging of white matter.

Methods

Twenty-two patients with Alzheimer's Disease (AD) and 27 cognitively normal healthy elderly controls (CN) were studied using T1-weighted imaging and DTI collected on a 4T MRI system (Bruker/Siemens). Images were registered to standard space. The determinant of the Jacobian from registration of each T1 image to the atlas was computed at each voxel to yield maps of deformation (JAC). Fractional anisotropy (FA) at each voxel was computed in subject space, then each subject's T1-> atlas registration was applied to each subject's FA map to yield FA maps in standard space. Linear models were: 1) FA maps as dependent variables (DV) with group and age as independent variables (IV), 2) JAC maps as DVs with group and age as IVs, 3) multivariate analysis with JAC and FA maps as DVs with group and age as IVs, and 4) JAC maps as DVs with group, age, and FA maps as IVs.

Results

The top panel of Figure 1 shows small regions where reduced FA is associated with AD (blue/green). The bottom panel shows that AD is associated with large regions of atrophy (blue/green) throughout the brain, including posterior parietal, temporal, and frontal regions. The top panel of Figure 2 overlays the group t-statistic maps from the multivariate analysis with the univariate FA analysis, and the bottom panel shows overlays with the univariate JAC analysis, to demonstrate where multivariate analysis leads to improved detection of disease effects. Red shows regions where the effect of AD was only detected when both FA and JAC were used as DV. Yellow shows regions where an AD effect was detected using either the multivariate or the univariate model. Green shows regions where the AD effect was only detected using the univariate analysis. As shown, the multivariate analysis is far superior than the univariate FA analysis (note large regions of red, few regions of yellow or green in Figure 2, top), while the univariate analysis of JAC is nearly as sensitive as the multivariate analysis (note large regions of yellow, few regions of red or green in Figure 2, bottom). Lastly, co-analysis using JAC as DV covarying for FA did not result in greater detection of the effect of AD.

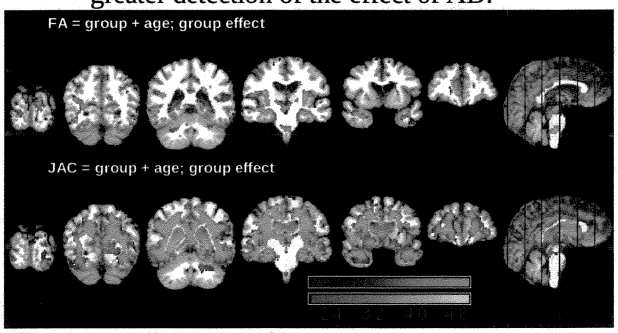

Figure 1: Group effects on FA and JAC.

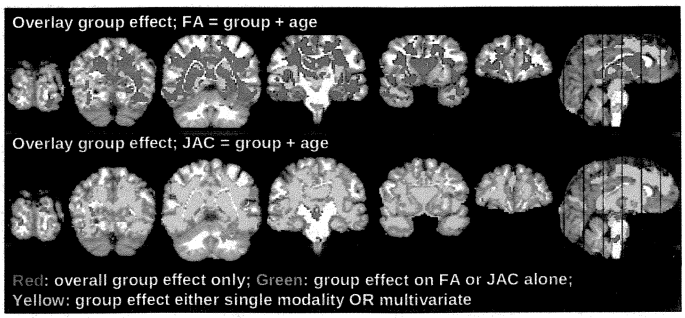

Figure 2: Overlay group t-statistic maps.

Discussion

We found that co-analysis of structural images and DTI did not reveal significantly more AD-related brain abnormalities than a voxel-wise analysis of structural images alone. However, the value of co-analysis may vary across different stages of the disease, especially in early AD. In future work, we will explore alternatives to voxel-wise analysis to identify regions in different modalities jointly associated with disease.

Acknowledgments This work was supported in part by NCRR P41RR023953.

Dissociated Gray Matter Atrophy and Hypoperfusion in Alzheimer's Disease and Parkinson's Disease

Y. Zhang[1,2], D. Tosun[1], P.Mojabi[1], M. Nezamzadeh[1,2], W. Zhan[1,2], C. Shirley[1,2], G. Kang[1], G. Glass[1,2], W. Marks [,2], MW. Weiner[1,2], N. Schuff[1,2]

[1] Department of Veterans Affairs Medical Center, San Francisco, CA, USA. [2] University of California, San Francisco, CA, USA.

Background: MRI studies reported gray matter structural and functional alterations in Alzheimer's disease (AD)[1,2] and Parkinson's disease (PD)[3,4]. However, whether AD and PD exhibit different relations between their respective structural and functional alterations, which could be of diagnostic value, remains unclear. To elucidate these relationships, we performed a nonparametric co-analysis of structural and functional modalities using voxel-based morphometry (VBM) and arterial spin labeling (ASL) MRI.

Methods: 22 AD patients (age=63.4±9.2yo; MMSE=21.3±5.2yo), 26 PD patients without dementia (age=65.1±5.3; MMSE=28.4±1.2) and 19 control subjects (CN, age=62.5±7.7yo; MMSE=29.3±0.9) were imaged at 4Tesla MRI. All subjects had a high-resolution T1-weighted MRI scan to measure brain structure and ASL-MRI to measure regional brain perfusion. Gray matter (GM) loss was derived by warping each brain image nonlinearly into an atlas brain (so called VBM). The same warping procedure was also applied to perfusion data to achieve a one-to-one correspondence between structural and perfusion maps. The spatially normalized GM and perfusion maps were smoothed with a 10mm^3 FWHM Gaussian kernels. Voxel-wise group comparisons were performed separately for each image modality using using ANCOVA with age, gender and calibration measures, such as intracranial volume (TIV) and perfusion of the motor cortex, as covariate. A co-analysis of concordance/discordance between structural and perfusion changes was performed using the statistical non-parametric (SnPM) package for bi-modal imaging data[5]. Regions showing significant dissociation between one modality and another were projected onto the standard brain template.

Results: 1) AD vs. CN: AD showed diffuse gray matter atrophy bilaterally in parietal and temporal cortices, particularly in the left hippocampal region, and a prominent hypoperfusion in bilateral parietal and superior temporal regions. 2) PD vs. CN: PD was associated with hypoperfusion predominantly in the right temporoparietal cortices, similar to hypoperfusion in AD, while in contrast to AD no significant gray matter atrophy was seen. 3) AD vs. PD: AD patients had more gray matter atrophy than PD diffusely in cerebral gray matter regions, whereas PD had significantly more gray matter atrophy than AD in bilateral cerebellum. In contrast to structure, AD had more reduced perfusion in bilateral temporal regions and left posterior cingulate gyrus than PD, while the only region of reduced perfusion in PD compared to AD was a small area of the left frontal cortex. 4) Dissociated gray atrophy and hypoperfusion in AD: In AD, gray matter atrophy without hypoperfusion was seen predominantly in bilateral temporal lobes (left figure), while the reverse was not significant in any regions. 4) Dissociated gray atrophy and hypoperfusion in PD: In PD, by contrast, gray matter hypoperfusion without atrophy was seen in right temporoparietal regions (right figure), while the reverse was not significant in any region.

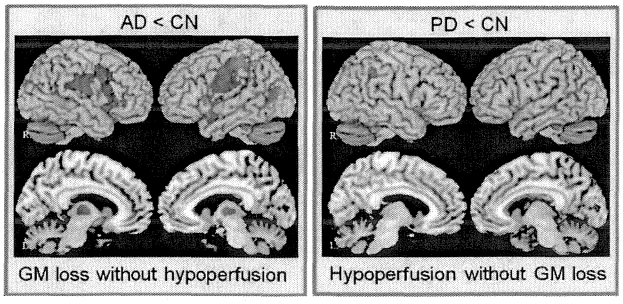

Conclusions: In conclusion, AD is associated with widespread atrophy, whereas PD is primarily associated with hypoperfusion. Detection of brain atrophy in temporoparital regions in PD patients may suggest concomitant AD.

References: 1. Du AT, et al. Neurology 2006. 2. Hua X, et al. Neuroimage 2008. 3. Derejko M, et al. Nucl Med Commun 2006. 4. Beyer MK, et al. Neurology 2007. 5. Hayasaka S, et al. Neuroimage 2006.

Combined T1- And DTI Weighted Contrast for High Resolution Human Brain Mapping Using 3D MPRAGE

M. Nezamzadeh[1,2], G. B. Matson[2,3], Y. Zhang[1,2], M. W. Weiner[1,2] and N. Schuff[1,2]

[1] Radiology, University of California San Francisco, [2] Center for Imaging of Neurodegenerative Diseases, CIND, VA medical center, San Francisco and [3]Pharmaceutical Chemistry, University of California San Francisco,

Introduction

High resolution 3D magnetization-prepared rapid gradient-echo (MPRAGE) with T1 weighting is generally the method of choice for mapping gray and white matter structures in the brain. Previously, MPRAGE has been combined with diffusion encoding [1-2] to achieve diffusion tensor imaging (DTI) without the inherent susceptibility distortions in echo planar imaging (EPI). However, an incorporation of DTI contrast in 3D-MPRAGE has not been shown before on human brain data. Furthermore, a combination of T1 and DTI weighted contrast should benefit assessment of gray/white matter boundaries, which has important implications for accurately imaging brain atrophy. The overall goal of this study was to develop multiple contrast high resolution MRI. Specifically, we show the incorporation of DTI contrast (i.e. fractional anisotropy (FA) and mean diffusivity (MD)) into T1-weighted 3D-MPRAGE using simulations based on equations given in Ref [3] as well as experimental results from human brain at 4T.

Methods

Simulations of MPRAGE were programmed in Matlab 7.0.4. For simulations of the MPRAGE signal, we used tissue parameters (to approximate human model at 4T) including T_1=1724 ms and T_2=70 ms for gray matter, and T_1=1043 ms and T_2=65 ms for white matter. For simulating diffusion contrast, we used values of apparent diffusion coefficients, ADC=0.00079 mm^2/s for gray matter and ADC=0.00056 mm^2/s for white matter based on literature values [4].

For experiments the 3D MPRAGE with DTI weighting was developed and implemented on a 4T MR scanner (Bruker, Siemens). DTI weighting in MPRAGE is achieved by applying radiofrequency (RF) pulses (90°_{+x}-180°_{+y}-90°_{-x}) in presence of diffusion sensitization gradients that encodes diffusion information in the longitudinal magnetization before the magnetization is mapped using the conventional train of shallow flip angle pulses of MPRAGE. The experiment is repeated along multiple directions to obtain DTI information. The following parameters were used; b-value=1000 s/mm^2 for diffusion encoding, derived from a gradient of strength g=15 mT/m with a duration δ=30 ms and diffusion encoding time TE_{diff}= 122 ms. A single housing transmit / 8-channel receiver head coil was used. MPRAGE parameters were; TR/TE =2000/3.1 ms, flip angle=8 degrees and 2mm isotropic resolution. Maps of MD and FA were computed using DTIstudio software.

Results

Simulation of the evolution of longitudinal magnetization in MPRAGE including DTI weighting is shown in Figure 1. Simulations were performed for linear k-space mapping. White matter with high (black) and low (green) diffusion directionality, i.e. FA, is shown in Figure 1, indicating diffusion contrast in MPRAGE. Gray matter is shown in red. The progression of the curves toward equilibrium is governed by a combination of the shallow tips and T1 [3]. The simulation shows that a substantial diffusion contrast between white matter with high and low FA values remains over a reasonable long period (about 400ms) in MPRAGE before the contrast disappears due to progression toward the steady state.

Representative experimental MPRAGE images of T1-w, MD and FA from a healthy subject are displayed in Figure 2. In general, both T1-w and FA maps show high contrast between gray and white matter. However, the FA map provides additional information not available with T1w alone, as shown in Figure 3. In detail, the intensity profiles of T1w and FA maps are superimposed in Figure 3a along a cross-section in the image (red line in Figure 2), showing systematic differences between T1w and FA. This is also depicted in the correlation map between T1w and FA in Figure 3b. In particular, T1w and FA profiles differs substantially in white matter (3c) and gray matter (3d) regions, implying additional contrast information.

Fig. 1. Simulated evolution of longitudinal magnetization in MPRAGE

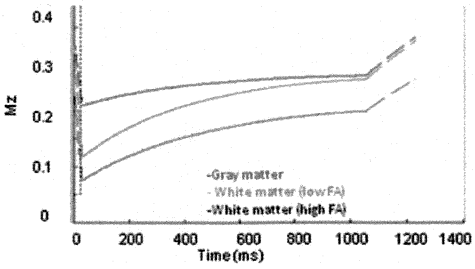

Fig. 2. Representative T1-w, MD and FA maps using DTI 3D MPRAGE from healthy human brain in vivo. The red line is a region along the brain to obtain the intensity profile of the images.

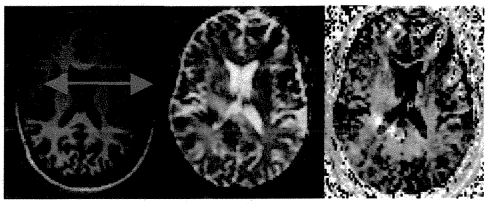

Fig. 3. Intensity profiles of T1-w (black) and FA (green) along a cross-section in the image of healthy human brain (Fig. 2) for the whole brain (a and b), white matter (c) and gray matter (d) regions. The T1-w signal intensities are scaled to 1.0.

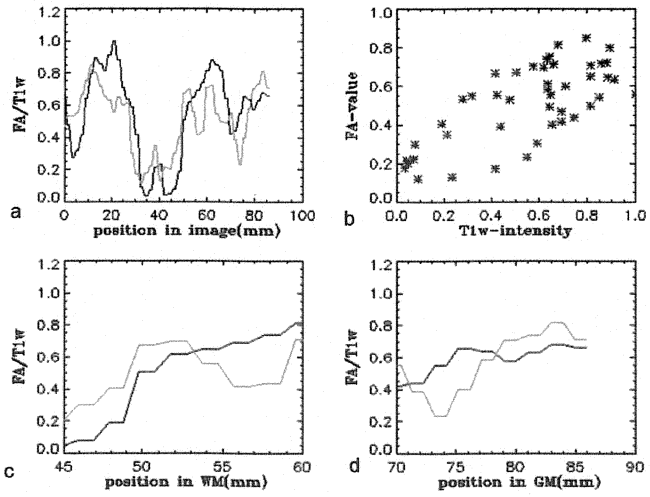

Conclusion

This study suggests DTI weighted MPRAGE is feasible for human brain imaging and expected to benefit assessment of gray/white matter boundaries. However, several limitations require improvement. First, residual transverse magnetization from diffusion weighting can interfere with the MPRAGE signal and therefore needs to be minimized either by applying crusher gradients or using RF pulses with more uniform flipping. Second, resolution was currently limited to 2 mm due to limits in SNR. We expect that SNR can be recovered and thus higher resolution afford by shortening the diffusion time (TE_{diff}) in combination with more efficient signal averaging utilizing parallel imaging. Furthermore, DTI contrast can be gained by tailoring dense k-space sampling with regard to diffusion decay of the signal.

Acknowledgement: Supported by the NIH grant (1P41RR023953).

References: 1. Numano T. et.al. MRI 23:463-468 ,2005. 2. Numano T. et.al. MRI, 24: 287-293, 2006, 3. Deichmann R. et.al. NeuroImage 12, 112-127, 2000. 4.Yoshiura T. et.al. MRM, 45: 734-740, 2001.

Nonlinear Time Course Of Brain Volume Loss In Normal Aging And Cognitive Impairment

Norbert Schuff, Duygu Tosun, Philip Insel, Gloria Chiang, Diana Sacrey, Michael W. Weiner

Background: It is now well established – based on longitudinal brain MRI - that mild cognitive impairment (MCI), potentially a transitional stage to Alzheimer's disease (AD), and AD are associated with higher rates of brain tissue loss than normal aging. Yet little is known about which parts of the brain loose tissue earlier than others and how compounding losses relate to cognitive decline. A major difficulty in solving this puzzle has been lack of an accurate model for progression of brain tissue loss. To circumvent this difficulty, we elucidated the dependence of regional brain tissue loss with age without *a-priori* models using a nonparametric approximation.

Method: Regional brain volumes from 147 cognitive normal (CN) subjects, 164 stable MCI (sMCI), 93 MCI-to-AD converters (cMCI) and 111 AD patients, between 51 to 91 years old and who had repeated 1.5T magnetic resonance imaging (MRI) scans over 30 months, were analyzed. The data was collected as part of the Alzheimer's disease Imaging Initiative (ADNI). Relations between regional brain volume change and age were determined using generalized additive models (GAM), an established non-parametric concept for approximating nonlinear relations. Changes in regional brain volumes as a function of age were fitted separately for each diagnostic group and for 40 regional brain volumes (and CSF spaces) defined with Freesurfer. To test the significance of nonlinearity between volume and age relations, we compared the fits from GAM with fits derived using a non-penalized generalized linear model (GLM), in which age was included as a linear variable while all other variables in GAM and GLM were the same.

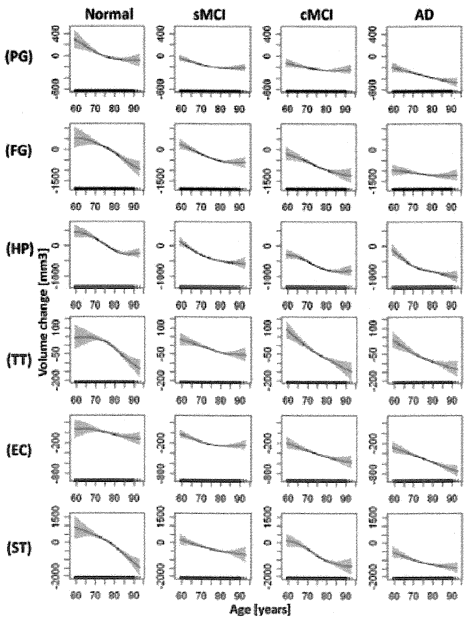

Results: Brain atrophy rates varied nonlinearly with age, predominantly in regions of the temporal lobe. Moreover, the atrophy rates of some regions leveled off with increasing age in control and stable MCI subjects whereas those rates progressed further in MCI-to-AD converters and AD patients. Representative estimations of brain volume loss as a function of age are shown in the Figure, separately for each diagnostic group and for the parahippocampal gyrus (PG), fusiform gyrus (FG), hippocampus (HP), transverse temporal lobe gray matter (TT), entorhinal cortex (EC), and superior temporal lobe gray matter (ST), in order of the significance of nonlinearity.

Conclusions: The approach has potential uses for early detection of AD and differentiation between stable and progressing MCI.

The impact of template selection on deformation based morphometry in MR-negative temporal lobe epilepsy

C. Scanlon, S.G. Mueller, S. Joshi, D. Tosun, P. Insel, I. Cheong, M.W. Weiner, K.D. Laxer

Background: Deformation based morphometry (DBM) non-linearly transforms brain images to a reference image, maximizing the alignment of the anatomies between the individual brain and the reference. The anatomical differences then lie in the deformation fields required to transform the subjects' brain. In this study we aim to compare the DBM results derived using 3 different reference images: 1) a symmetrical unbiased large deformation (ULD) atlas, 2) a standard SPM atlas, 3) a single subject atlas. Specifically, we tested the ability of the 3 atlases to optimize the abnormalities in temporal lobe epilepsy with visually normal MRI (TLE-no); a group known to demonstrate subtle volume deficits quantitatively.

Methods: T1-weighted MR imaging data was acquired for 14 TLE-no and 33 controls on a high-field 4-Tesla scanner. Images of right onset patients were right-left flipped so the ipsilateral hemisphere was on the left in all cases. A symmetrical ULD atlas brain was constructed from 31 control subjects (both original and sided flipped), where subjects are simultaneously deformed iteratively into an average brain. The second template was constructed in SPM2 with the same subjects using the recommended protocol. Finally, the control subject whose mean Jacobian determinant was closest to the ULD atlas was chosen for as the single-subject atlas.

The process of fluid flow deformation of each subject to a template was carried out identically for all templates. Jacobian determinants were calculated from the derived deformation field and the resulting maps were smoothed by a 12mm FWHM Gaussian kernel. Voxelwise statistical analysis was performed using a general linear model (GLM) to determine the effect of 'group' (patient or control) on the measurement parameter at each voxel. This was repeated for each atlas.

Individual Jacobian maps were also subdivided into 16 regions of interest. Effect sizes between patients and controls were calculated to determine the sensitivity of each atlas.

Results: In the voxel based analysis, 8 clusters were identified using the ULD atlas. Four of these clusters were also identified using the SPM template but with a smaller cluster size. No clusters were identified using the single subject atlas.

In 13 out of 16 ROIs the ULDA template analysis revealed larger effect sizes between patients and control subjects. Average effect size determined over all ROIs was 0.38 for the ULDA template and 0.26 for the SPM template (Figure 3).

Conclusion: The results demonstrate that the ULD atlas is more sensitive in detecting the subtle structural changes associated with TLE-no than the SPM or single subject atlases. The ULD atlas contains sharper features than the SPM atlas which may increase the accuracy of the registration. The ULD atlas also avoids the bias towards a particular subject's geometry when selecting a single subject atlas. The ULD atlas should be adopted in DBM studies where superior sensitivity is required.

Structural Plasticity in Stroke inferred by probabilistic fiber tracking and MEG.

Monica Bucci[1], Kelly Westlake[1], Christopher Nguyen[1], Bagrat Amirbekian[1,2], Eugenio Parati[4], Srikantan Nagarajan[1,2], Roland G. Henry[1,2,3]

Department of Radiology and Biomedical Imaging[1], Graduate Group in Bioengineering[2], Department of Neurology[3], University of California, San Francisco, California, USA. Department of Neurology, Neurological Institute Carlo Besta, Milan, Italy[4]

Introduction: Neural plasticity may play a role in motor recovery after stroke in terms of structural remodeling of white matter in the ipsilesional and contralesional hemispheres and functional reorganization of activity in the sensorimotor cortices. Animal tracing studies show evidence that in the healthy brain, neural activity in the motor areas of both hemispheres are functionally coupled and balanced in terms of mutual inhibitory control via transcallosal cortico-cortical inhibitory circuits and stroke may disrupt this balance. Moreover, intra-cortical connections between different regions, such as those between M1 and Ventral Premotor Cortex, show functional asymmetry. Previous in vivo human studies have not mapped completely these important networks and therefore we have attempted to map the structural connectivity of the network involved in hand motor function, by combining time-frequency reconstructions of magnetoencephalography (tfMEG) data, with HARDI diffusion MR data, in 4 controls and 4 stroke subjects assessed before and after a novel rehabilitation intervention.

Methods: 4 stroke subjects in subacute/chronic phase after a stroke in the sensorymotor cortex and/or internal capsule of the right hemisphere were imaged with High-angular Resolution Diffusion MRI, acquired before and after a robotic neurorehabilitation intervention for the stroke subjects. The same imaging protocol was applied to 4 healthy control subjects in a single session. For fiber tracking we used probabilistic QBall fiber tracking algorithm developed in our laboratory and based on previously validated non-parametric estimates of the uncertainties in fiber tracking directions. To locate the seed regions for Fiber Tracking of functional motor pathways within the motor cortex we used task based tfMEG activations from both hemispheres during hand motor tasks, obtained bilaterally, in both the stroke and control subjects.

Results: Seeding in MEG-based Hand Motor Region with q-ball probabilistic fiber tracking in 4 control subjects, we successfully mapped the structural connectivity of the motor network yielding known motor pathways. Seeding in MEG-based Hand Motor Region of the ipsilesional and contralesional hemispheres in the stroke patients, as they demonstrated different patterns of recovery from stroke after neurorehabilitation, we showed changes over time of the structural connectivity of both ipsilesional and contralesional areas involved in the hand motor network.

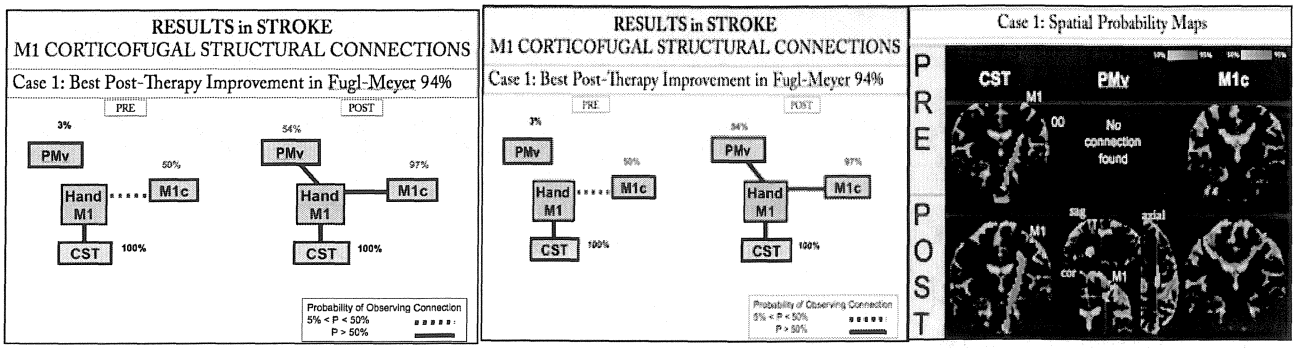

Conclusion: In our study we were able to map the hand motor structural network using probabilistic q-ball fiber tracking combined with functional data from tfMEG in normal human controls. Our preliminary data suggest a normal variability in this network. This multimodal imaging approach enables better interpretation of the underlying plastic changes after stroke and results in significant improvement over current methods to map the connections of the motor network in stroke patients where the effects of lesion, interhemispheric competition and neural plasticity related to recovery, may have altered the normal structural connectivity. In stroke patients the structural changes seen in the post- versus pre-therapy comparisons between the Intra-Hemispheric, Inter-Regional and Inter-Hemisheric connections may become a strong independent predictor of motor recovery.

A novel variational Bayesian method for spatiotemporal decomposition of resting-state fMRI

Yi-Ou Li1, Srikantan Nagarajan1, Hagai Attias2, Pratik Mukherjee1

1 University of California San Francisco, San Francisco, United States, 2Golden Metallic Inc, San Francisco, United States

Purpose

We apply a novel variational Bayesian factor partition (VBFP) to resting state fMRI data and compare it with the standard independent component analysis (ICA) algorithm [Bell & Sejnowski, Neural Computation 1998; 7:1129]. It is shown that VBFP indentifies similar functionally coherent brain networks and their temporal fluctuations as ICA does. The potential advantages of VBFP are the inference of noise model and robustness on small sample size.

Methods

Image acquisition: Ten healthy subjects were studied on 3T EXCITE MR scanners (GE Healthcare, Waukesha, WI) using an 8-channel head coil. BOLD fMRI images of the supratentorial brain were obtained using a 2D multislice gradient echo echoplanar acquisition with FOV 22x22 cm, 64x64 matrix, ASSET factor 2, 4 mm interleaved slices with no gaps, and TR of 2 sec and TE of 28 sec. Two hundred (T=200) brain volumes are collected over a period of 7 minutes with the subject's eyes closed to minimize exogenous visual activation. *Preprocessing*: (a) Motion correction (b) In-brain voxel extraction (c) Spatial smoothing (d) Temporal filtering. *Data analysis*: ICA and VBFP are applied to the fMRI data to achieve a spatiotemporal decomposition as Y=AX where Y is the TxN spatiotemporal fMRI data matrix with N in-brain voxels in each row and T time points, X is the set of decomposed spatial activation maps, A is the time course matrix containing the temporal fluctuations of the sources in X. The spatial sources are normalized to unit variance and threshold at 1.5 standard deviation with the supra-thresholded voxels displayed on the brain anatomy.

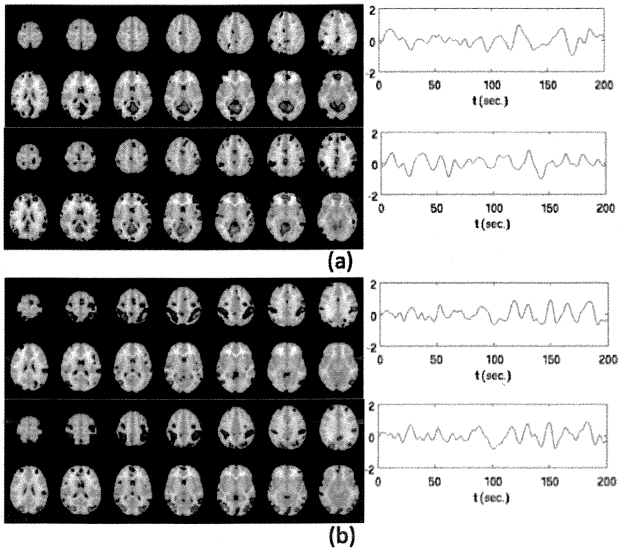

Results

Figures 1a and 1b each show a pair of activation maps and their time courses estimated by ICA (top panel in 1a and 1b) and VBFP (bottom panel). It can be observed that: in (a), the strongest regions of functional connectivity are in the bilateral posterior cingulate gyri, part of the brain default mode network; in (b), VBFP better shows anticorrelated networks than ICA, specifically, a bilateral perirolandic somato-motor network (blue regions are negatively correlated with the time course) versus a bilateral occipital network (red regions are positively correlated with the time course).

Discussion

In this work, VBFP is applied to achieve a sparse spatiotemporal decomposition of resting state fMRI data and incorporates automatic relevance determination in a fully Bayesian inference framework. Hence, the VBFP method provides a general framework for the data-driven analysis of functional imaging data such as fMRI and MEG.

PET-Optical Dual Modality Imaging of Pancreatic Cancer Using Targeted Dendritic Nanoparticles

David M. Pham[1], Jinjin Feng[1], Elizabeth Allen[2], V. Ramana Kotamraju[3], Kazuki Sugahara[3], Francis Szoka[4], Jiang He[1], Erkki Rouslahti[3], Doug Hanahan[2], Henry F. VanBrocklin[1], Ella F. Jones[1]

[1]Department of Radiology and Biomedical Imaging, UCSF; [2]Diabetes Center, UCSF;
[3]Sanford-Burham Medical Research Institute, UCSB; [4]Biopharmaceutical Sciences, UCSF

Background: Pancreatic cancer strikes more than 42,000 Americans and claims over 35,000 lives every year. The overexpressed angiogenic markers such as α_v-integrins in neovasculature are promising targets for early tumor detection. Herein, we demonstrate the utility of a new RGD sequence (iRGD) on a dendritic nanoplatform that mediates the binding and internalization in pancreatic cancer cells. **Methods:** The pegylated 6th generation PAMAM dendrimer was labeled with FAM, FAM-iRGD, Cy5.5 and/or [^{18}F]-FBAM through step-wise coupling reactions using iodoacetic anhydride and protected cysteine. Mercaptoethanol was used to neutralize the remaining iodoacetyl groups to prevent undesirable *in vivo* reactions. The resulting probes were characterized by GPC, MS and fluorescence assays. PDAC cell lines derived from the pancreas of tumor-bearing Kras^{G12D} p48-Cre Ink4a+/- and Kras^{G12D} p48-Cre p53+/- mice were used for in vitro uptake studies. The initial biodistribution and *in vivo* PET and optical imaging studies were performed using transgenic PDAC mice. **Results:** The probe synthesized for biodistribution studies contains an average of 15 FAM-iRGD. Our results indicate that the multivalent FAM-iRGD$_{15}$-dendrimer has tumor uptake >2 times higher than the native FAM-iRGD and FAM-dendrimer without iRGD (Figure 1). The PET-optical dual labeled probe comprises 15 FAM-iRDG, 1 Cy5.5 and 10 [^{18}F]-FBAM. The PET imaging at 1 h showed significant uptake in the tumor. Despite the high background signal from blood and liver, *in vivo* optical imaging at 24 and 48 h showed specific accumulation in the tumor and washout from the other organs. The *ex vivo* results at 48 h showed tumor uptake >2 times higher than that of any other organs (Figure 2). **Conclusions:** The multivalent dendrimer with high payload of iRGD shows effective targeting to pancreatic cancer. Incorporation of multiple reporters allows for dual PET and optical imaging to characterize the probe's *in vivo* biodistribution from early to late time points.

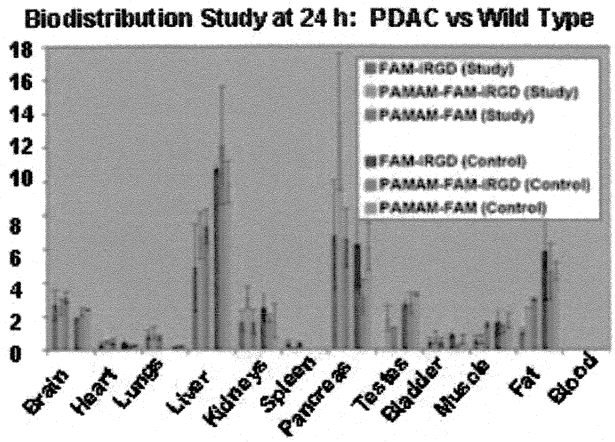

Figure 1. A preliminary biodistribution of the FAM-iRGD-dendrimer probe compared to two control probes, FAM-iRGD and FAM-dendrimer in both PDAC and wild type mouse models (n=4 for each group). PDAC transgenic mice are in blue (5FAM-iRGD), light blue (5FAM-iRGD-dendrimer) and green (5FAM-dendrimer); wild type mice are in red (5FAM-iRGD), orange (5FAM-iRGD-dendrimer) and yellow (5FAM-dendrimer). From this preliminary study, it is clear that the 5FAM-iRGD-dendrimer exhibits tumor uptake over 2 times higher than the control probes. Non-specific liver uptake is relatively low with tumor-to-liver ratio of 2:1 compared to 0.9-1.2 from the two control probes.

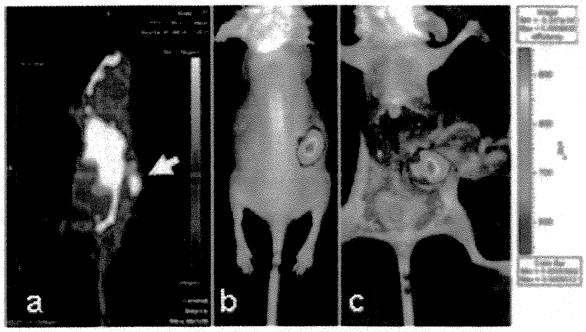

Figure 2. In vivo imaging studies of the PET-optical dual labeled probe in PDAC mice. **a)** In vivo PET image 1 h post injection; **b)** in vivo optical image 48 h post-injection; **c)** probe specificity to pancreatic cancer as confirmed by the post-mortem optical imaging study.

8 Channel 3T Neonatal MRI Volume Phased Array Reciever

Nan Tian, Brian Hill, Cornelius von Morse, Dan B. Vigneron, A. Jim Barkovich, Duan Xu

Introduction: The development of dedicated neonatal imaging coils has made high-quality anatomic imaging, diffusion tensor imaging, and proton MR spectroscopy feasible for neonates. (1) Great benefits in scanning at the 3T scanner with a phased-array receiver through the parallel imaging include increased signal-to-noise ratio (SNR), increased resolution, and reduced scan time. (2) However, challenges presents due to increased coupling 3T and limited space for pre-amplifiers and cables in neonatal coil. Here we present our initial results from the system.

Methods: A neonatal eight-channel volume phased array coil (Fig 1) with capacitive decoupling was built. A cylindrical knee phantom was scanned at 3T using body coil (birdcage type), birdcage head coil, 8 channel head coil, 8 channel knee coil and this 8 channel neonatal phased array coil without using parallel imaging for SNR comparison. Imaging parameters: 2D SCOUT; FOV: 14x14cm; matrix of: 256x256; TE: 2 ms; TR: 1000 ms; Tip Angle: 30 degree. SNR is calculated from reconstructed raw-image using Matlab.

Six signal circles (4mm diameter) were drawn at the center and the top, bottom, left, right edges of the phantom; plus one highest SNR signal spot. Four noise ROI's were drawn at the corners of the images where phantom was not present; standard deviations of the noise inside the circles were obtained. SNR was calculated by dividing signals from each signal circles to the average of the four noise circles' standard deviations.

Results: SNR of body coil: 2.39; birdcage adult head coil: 37.2. SNR of single channel surface coil: 8 channel adult head: 34.4; 8 channel knee: 103.0; and 8 channel neonatal array: 89.3. The difference in SNR of the phantom images is clear from both body coil (fig 2a) and phased array coil (fig 2b).

Conclusion and Future Work: A 3T neonatal phased array was built to provide competitive SNR performances for the 3T neonatal MRI scan. It has much higher SNR than birdcage coils and 8 channel head coil. In addition, accelerated scans of neonates can be done at 3T using this coil.

Fig 1: 8-channel phased array coils;

Figure 2, Example of SNR Measurement circles on an one channel image using Collected using 8 channel neonate phased array.

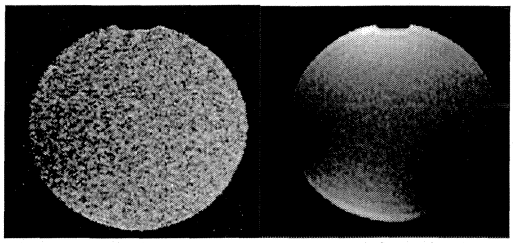

Figure 3: (left) picture reconstructed from body coil, (right) combined image reconstructed from the 8 channel neonatal phased array.

Reference: 1.Barkovich AJ., MR imaging of the neonatal brain, Neuroimaging Clin N Am. 2006 Feb;16(1):117-35, viii-ix. Review.

2. Roemer PB, Edelstein WA, Hayes CE, Souza SP, Mueller OM. The NMR phased array. *Magn Reson Med* 1990; **16**: 192-225.

Detection of early brain folding patterns in normal human fetuses from in utero MRI

Piotr A. Habas, Julia A. Scott, Ahmad Roosta, Orit A. Glenn, A. James Barkovich, and Colin Studholme

Introduction. Recent advances in fetal brain MRI reconstruction and image analysis open up opportunities for modeling of early brain development from clinical imaging. Quantification of the early fetal brain growth in utero provides a sensitive biomarker for normal/abnormal development and can potentially predict later cognitive or functional impairments that manifest themselves through structural abnormalities. In this study, we characterize early stages of sulcal formation via curvature analysis across a population of young fetuses with normal brain development imaged in utero.

Methods. Clinical MR imaging was performed on a 1.5T scanner for 40 fetuses (20.57-27.86 weeks GA) with normal brain development. For each subject, a high-resolution isotropic 3D volume was reconstructed from multiple axial, coronal and sagittal stacks of T2w 2D MR slices (Kim et al., 2010). All 3D MR volumes were automatically segmented into individual brain tissues using an atlas-based technique (Habas et al., 2010a; Habas et al., 2010b). To account for the age-related changes in the brain size, the resulting white matter (WM) maps were spatially normalized using global linear registration. Outer WM surfaces were tessellated into triangular meshes and mean surface curvature H was calculated at each mesh vertex. For temporal analysis, curvature values were mapped from subjects' surfaces onto a common group-average WM surface obtained via volumetric group-wise registration. For each vertex v of the average surface, temporal changes in surface folding were analyzed using a linear model of curvature vs. age t, $H(v,t) = B(v)\cdot t + C(v)$.

Results. The overall area of the normalized WM surface changes linearly (R^2=0.89) with the age of the fetus at the rate of 0.22cm^2/week and ranges from 8.5cm^2 at 21 weeks to 10.5cm^2 at 28 weeks.

The top figure shows typical WM surfaces with mean curvature values for subjects at 21-28 weeks GA. The average mean curvature calculated over the entire surface decreases linearly with age (R^2=0.92) at the rate of -0.03/week. This is mainly driven by the linear growth of the fraction of vertices with negative curvature values (cool colors) indicating increasing sulcation of the WM surface.

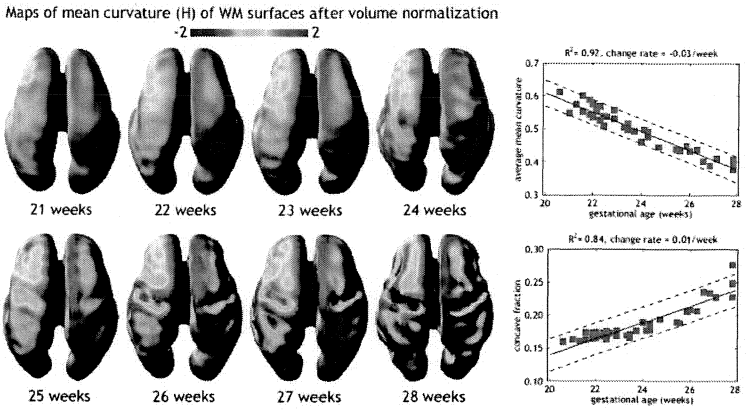

The bottom figure presents typical curvature values mapped from individual WM surfaces of subjects at 21-28 weeks GA onto the group-average WM surface. The results of vertex-wise linear modeling of temporal changes in WM surface curvature are illustrated by the B-map and T-map (far right). Statistically significant T values ($|T|>4.8$) indicate the following early brain folding patterns: formation of the central sulcus, operculization of the sylvian fissure, deepening of the parieto-occipital sulcus, formation of the calcarine sulcus and early formation of the cingulate sulcus.

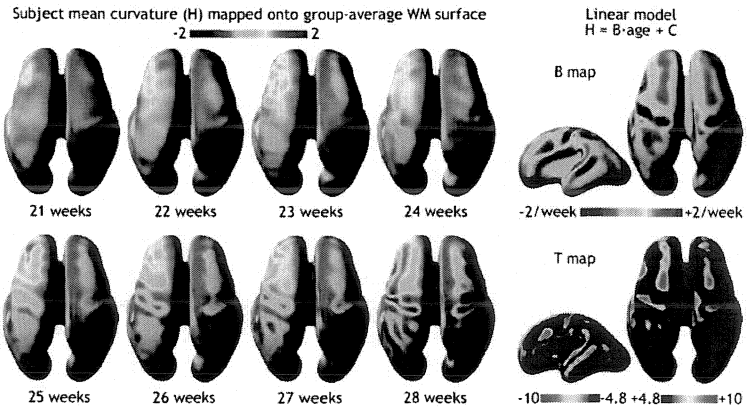

Conclusions. Mean surface curvature maps provide accurate and reliable characterization of early folding patterns in the normal human fetal brain from in utero MRI.

References

Habas et al., 2010a. Atlas-based segmentation of developing tissues in the human brain with quantitative validation in young fetuses. Human Brain Mapping, in press.

Habas et al., 2010b. A spatiotemporal atlas of MR intensity, tissue probability and shape of the fetal brain with application to segmentation. Neuroimage, in press.

Kim et al., 2010. Intersection based motion correction of multislice MRI for 3-D in utero fetal brain image formation. IEEE Trans. on Medical Imaging, 29(1), 146-158.

Diffusion tensor imaging in newborns: rejection of images affected by motion

Olga Tymofiyeva, Christopher P. Hess, Nan Tian, A. James Barkovich, Duan Xu

Introduction. Diffusion tensor MRI (DTI) enables tracking of white matter pathways. DTI has been performed on preterm- and term-infant brains [1]. Since sedation of infants is usually not performed, data quality suffers from bulk motion. The goal of this study was to analyze the occurrence of corrupted diffusion-weighted images and develop an image rejection algorithm to achieve better processed diffusion images.

Methods. DTI imaging was performed on 21 neonates, including 10 premature, 6 term neonates, and 5 term neonates at the age of 6 months. Preterm and term babies were scanned at 1.5T GE EXCITE MR scanner using half-Fourier SE EPI, with a FOV of 30cm, 128x128, min TE, 30 directions, bvalue 600 s/mm^2 for preterm and 700 s/mm^2 for term infants. 6 months scans were done on the 3T using similar protocol as the term infants. All images were zero-filled to 256x256.

The obtained diffusion-weighted DICOM images were analyzed pixelwise and the diffusion directions in which images with artifacts occurred were rejected using the following criteria. When a certain amount of pixels deviated from the corresponding mean pixel value for all diffusion directions by several standard deviations, the direction was rejected. The thresholds for the number of pixels and standard deviations were set empirically. Slices covering nasal cavities and affected by susceptibility artifacts were excluded from the analysis. The algorithm was implemented in Matlab, and data reconstruction and fiber tractography were performed using Diffusion Toolkit (dtk) [2].

Results. Figs. 1b and 1c show two typical examples of corrupted images. The use of half-Fourier k-space sampling increases sensitivity to bulk motion [3]. Depending on the direction of object motion, the DC component of the k-space is displaced either into the high spatial frequencies causing ripple-like intensity oscillations across the image (Fig. 1b) or outside of the sampled range causing a dramatic signal loss (Fig. 1c). On average 2.5 directions were rejected (range 0-8). For 3 out of 21 scans, no rejection was necessary. Fig. 2 shows an example of tractography without rejection (a) and after rejecting 3 directions (b).

Discussion. Rejection of diffusion directions in images with artifacts significantly improved fiber tractography. Unless the location of the DC component of the k-space is detected and an adaptive version of the homodyne algorithm is used [3], affected images have to be excluded from diffusion data reconstruction. Inter-image motion correction algorithms cannot correct for these errors.

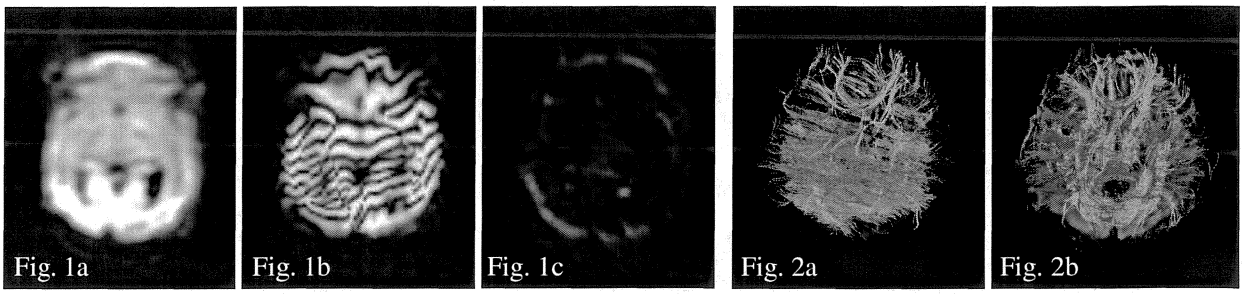

Fig. 1 Examples of a normal diffusion-weighted image of a preterm-infant brain (a) and two rejected images (b and c). Fig. 2 Tractography without rejection (a) and after rejecting 3 directions (b).

References.

1. Berman JI et al (2005) Neuroimage 27:862-71.
2. Wang R et al (2007) Proc Intl Soc Mag Reson Med 15, #3720.
3. Storey P et al (2007) MRM 57:614-19.

Hyperpolarized ^{13}C 3D Dynamic MRSI with Compressed Sensing

Peder E. Z. Larson[1], Simon Hu[1], Michael Lustig[2], Adam B. Kerr[3], Sarah J. Nelson[1], John Kurhanewicz[1], John M. Pauly[3], Daniel B. Vigneron[1]

[1]Radiology and Biomedical Imaging, UCSF, [2]Electrical Engineering and Computer Science, UCB, [3]Electrical Engineering, Stanford

Introduction: Time-resolved spectroscopic imaging following injection of hyperpolarized [1-^{13}C]-pyruvate can provide valuable and detailed metabolic information, including perfusion, uptake and kinetics. We have developed a dynamic ^{13}C 3D MRSI method combining multiband excitation pulses with a compressed sensing (CS) acquisition and reconstruction scheme that enables a 12x12x16 matrix with 3.5x3.5x5.4 mm and 10 Hz spectral resolution every 2 sec.

Methods: The compressed sensing acquisition used random phase encode blips in x and y that were applied during a flyback EPSI readout gradient [1], resulting in undersampling and an incoherent aliasing pattern suitable for CS [2]. This allowed for exploitation of the spatial and spectral sparsity of the hyperpolarized ^{13}C signal, and the encode blip patterns were varied between acquisitions to exploit the temporal sparsity. The wavelet transform applied to the time dimension was used as the sparsifying transform and a total variation (TV) penalty was also included. This sparsifying transform uses the metabolite spatial and spectral information from all time points to effectively constrain the reconstruction and exploits the generally smoothly varying temporal signal. The reconstruction was validated in simulations.

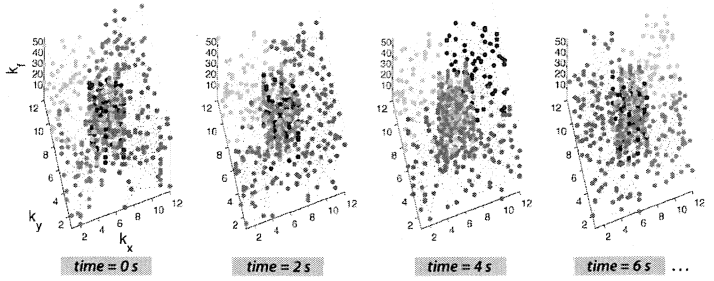

Figure 1: Randomized sampling pattern for the first four images. The color represents the phase encode ordering, which is varied for each image to increase the temporal incoherency.

A spectral-spatial multiband excitation pulse was used for efficient use of the hyperpolarized magnetization [4] with a 2.5° flip angle for [1-^{13}C]-pyruvate, the injected substrate, and 12° for the metabolic products of [1-^{13}C]-lactate and [1-^{13}C]-alanine so they can be more readily observed. Animal imaging of transgenic liver and prostate tumor models was performed on a GE 3T system using a double spin-echo sequence with TE = 160ms, TR = 250ms, 12x12x16 matrix, 3.5x3.5x5.4 mm resolution (0.066 cc) and 2 s per image – an overall 18-fold acceleration.

Results: The in vivo reconstructed spectra show improved peak detection over our previous CS algorithms [1], especially at later time points, because the new CS method utilizes all of the temporal information. At both time points, the elevated lactate clearly distinguishes the liver tumor from normal liver tissue. This acquisition allowed for measurements of localized, time-resolved metabolic information. The prostate tumor had elevated lactate with a later arrival and a longer duration than in other tissues and organs.

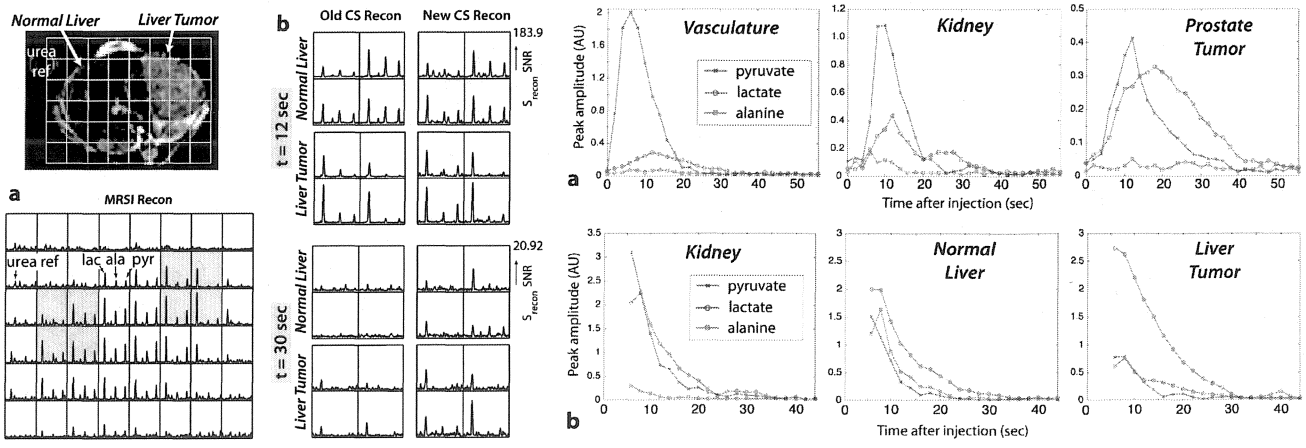

Conclusions: The improved sampling and reconstruction strategies for compressed sensing combined with efficient multiband pulses have allowed for full 3D dynamic imaging every 2 sec.

References: [1] Hu S, et al. JMR 2008; 192: 258-264. [2] Lustig M, et al. MRM. 2008; 58: 1182–1195. [3] Larson PEZ, et al. JMR 2008; 194:121-127. *We acknowledge support by NIH grant R01 EB007588 and American Cancer Society PF-09-036-01-CCE.*

Rapid 5-minute Echo-Planar Spectroscopic Imaging of Prostate Cancer Patients at 3T

G. D. Reed[1,2], P. E. Larson[1], J. Kurhanewicz[1,2], and D. B. Vigneron[1,2]
[1]Radiology and Biomedical Imaging, University of California, San Francisco, San Francisco, California, United States, [2]Joint Graduate Group in Bioengineering, UCB / UCSF, Berkeley, California, United States

Introduction

Proton spectroscopic imaging of the prostate has become a valuable clinical tool due to its effectiveness in detecting the presence and aggressiveness of prostate tumors [1]. However, the long acquisition times (typically 15-20 minutes) for the 3D phase encoding traditionally employed can be prohibitively long. A flyback echo-planar readout sequence has been developed and recently implemented for our clinical cases at UCSF. This sequence necessitates only 2 dimensions of spatial phase encoding, thus drastically reducing minimum scan time. This reduction in scan time facilitates greater flexibility in acquisition, since the shortened scan time allowing for longer repetition times (to avoid metabolite saturation) and increased encoding matrix sizes. Comparison with a 1.5T 3D phase-encoded sequence showed that the flyback sequence can achieve comparable spatial resolution (7mm isotropic), improved spectral resolution, and significantly improved SNR in a 5-minute 3T exam as compared to a 17-minute scan at 1.5T.

Methods

The sequence uses a spatially selective excitation followed by a train of dual-band spectral-spatial refocusing 180s for partial water suppression [2] and an MLEV phase-cycling pulse train for upright citrate resonances with reduced transit gain sensitivity [3]. For X-axis localization, an interleaved flyback echo-planar readout was implemented [4,5]. Using TE = 85 ms, TR = 2s, a 16×10×8 matrix could be acquired in 5.5 minutes. Two methods were independently evaluated on a 3T GE MR scanner in prostate cancer patients. First, the resolution was increased isotropically from 5.4 mm to 7.0 mm (approximately doubling the voxel volume). A second acquisition over the same volume with 5.4 mm resolution using 2 averages was also acquired (resulting in an 11 minute scan). Two spectroscopic acquisitions (one for each method) were acquired on 14 prostate cancer patients, and the data was assessed for spectral quality and diagnostic value. Flyback spectroscopy data was also compared to conventional 1.5T 3D MRSI acquisitions for the 3 of the 14 patients.

Results

All foci of abnormal metabolism, when present, were clearly visible at both the 0.16 cc (11 minute scan) and 0.34 cc (5 minute scan) resolutions. Peripheral zone voxels showed similar citrate and choline SNR for both acquisitions, and both acquisition schemes showed similar diagnostic usefulness. Patients scanned at both 1.5T using 3D phase encoding and at 3T using the flyback scan, each with 0.34 cc voxels, exhibited improved spectral resolution and a significant ($p<10^{-6}$) increase in SNR by a factor of 3.5 for both choline and citrate resonances in peripheral zone voxels. The flyback spectroscopic data was comparable or superior in diagnostic utility compared to the 1.5T data.

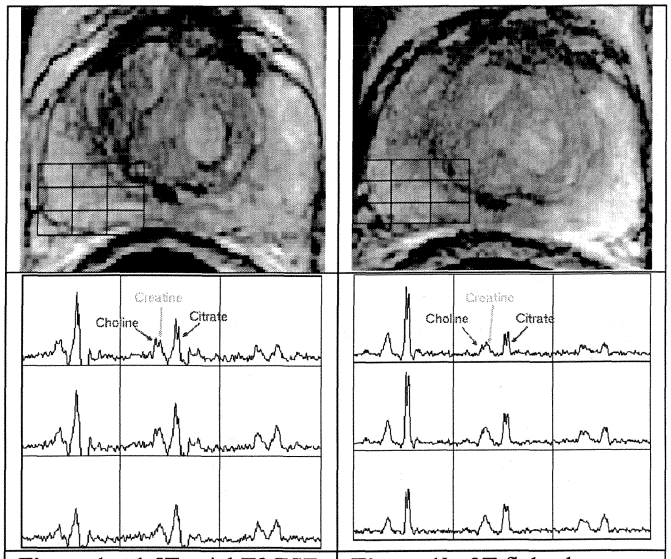

Figure 1a: 1.5T axial T2 FSE (top) and spectroscopic data (bottom) using 3D phase encoding acquisition with 7mm isotropic resolution. Scan time is 17 minutes.

Figure 1b: 3T flyback spectroscopy data from the same patient in roughly the same location shows improved SNR and citrate splitting. Scan time is 5.5 minutes.

Conclusion

3T echo-planar spectroscopic imaging of the prostate demonstrated the ability to provide fast 5-minute acquisition times without compromising data quality. This acquisition technique greatly improves the clinical applicability of prostate MRSI and is now applied to all 3T clinical patients at UCSF.

Acknowledgements: We acknowledge funding support from NIH RO1 CA111291 and CA059897.

References:

[1] J. Kurhanewicz, et al., Radiology 198(3), 795 (1996).
[2] C. Cunningham, et al., Magnetic Resonance in Medicine 53(5), 1033 (2005).
[3] A. P. Chen, et al., Magnetic Resonance Imaging 24(7), 825 (2006).
[4] A. P. Chen, et al., Magnetic Resonance Imaging 25(6), 1288 (2007).
[5] C. H. Cunningham, et al., Magnetic Resonance in Medicine 54(5), 1286 (2005).

Hyperpolarized MR imaging at 14T and corresponding histopathology for the non-invasive characterization of the TRAMP model

Kayvan R. Keshari, Subramaniam Sukumar, Robert Bok, Mark Van Criekinge, Daniel B. Vigneron, and John Kurhanewicz

Department of Radiology and Biomedical Imaging, University of California San Francisco (UCSF), San Francisco, California, United Sates

In recent work, hyperpolarized ^{13}C magnetic resonance (MR) has emerged as an exciting new technique to investigate biochemical and physiologic processes *in vivo*. Utilizing dissolution dynamic nuclear polarization (DNP), which has the potential to enhance ^{13}C MR signals 5 orders of magnitude, [1-^{13}C]pyruvate has been applied to the study of metabolism in preclinical models. Hyperpolarized enhancements are irreversibly lost due to spin relaxation mechanisms, metabolism and RF saturation. Additionally, high fields studies are hindered by increased chemical shift dispersion and T_{2^*} effects. The goal of this study was to develop a 3D frequency specific imaging sequence that could be used at high fields for molecular imaging and compare it to the histopathology of a transgenic model of prostate cancer (TRAMP).

[1-^{13}C]pyruvate (14.2M) and ^{13}C urea (6.4M) were prepared using the OX63 radical and polarized using an Oxford Hypersense. The experiments were preformed on a 14T, 600WB micro-imaging spectrometer equipped with 100G/cm gradients (Varian Instruments). An echo planar imaging (EPI) based pulse sequence was constructed using frequency specific pulses (*f = pyruvate, lactate or urea* and n,N=12) to generate a 3D image for each metabolite with an acquisition time of approximately 180ms.

$[90_f - (180_f - EPI_n)_N]_f$

To understand the histopathology of TRAMP tumors relative to hyperpolarized imaging, tumors were excised and stained using hematoxylin & eosin (H&E, for morphology), KI-67 (a nuclear stain for proliferation), and pimonidazole (PIM, a stain for hypoxia).

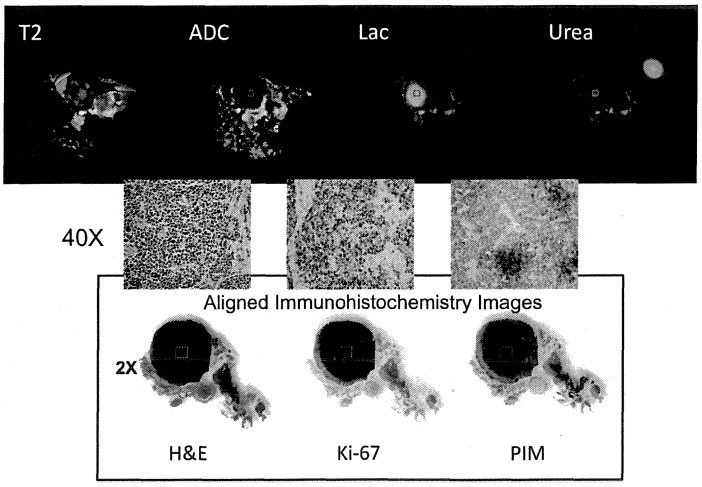

Representative ^{1}H T_2-weighted images and hyperpolarized ^{13}C 3D EPI images after injection of copolarized [1-^{13}C]pyruvate and ^{13}C urea (**Figure**) demonstrate the distribution of ^{13}C urea and [1-^{13}C]lactate, produced from pyruvate. There is good spatial correlation to the TRAMP tumor in comparison to corresponding T_2 anatomy and apparent diffusion coefficient maps (ADC). When comparing hyperpolarized data to histopathology similarities are seen between regions of necrosis and lack of hyperpolarized signal. Additionally, areas of hypoxia show varying metabolic patterns and will be further compared in a larger study. This preliminary study demonstrates the use of a pulse sequence for obtaining chemical shift specific images from hyperpolarized ^{13}C studies at high field strengths *in vivo* and provides a means to compare acquired data to corresponding histopathology to understand the underlying biochemistry.

REFERENCES:

[1] Golman K et al. Cancer Res 2003; 100(18): 10435-10439. **[2]** Ardenkjaer-Larsen J et al. PNAS 2003; 100(18): 10158-10163 **[3]** Albers MJ et al. Cancer Res 2008; 68(20): 8607-15 **[4]** Day et al. Nat Med 2007; 13(11): 1382-7

Hyperpolarized 13C Biomarkers of Androgen Independent Prostate Cancer

Robert Bok, Paniz Vafaei, Lynn DeLosSantos, Vickie Zhang, Kristen Scott, Phil Guan, Dan Vigneron and John Kurhanewicz

Introduction: Hormone therapy (androgen deprivation therapy) affects the cellular bioenergetics of the prostate and is a major component of prostate cancer treatment. Recurrent prostate cancer, following prostatectomy or radiation therapy, is commonly treated with androgen deprivation. Ultimately, this fails and the cancer progresses to an androgen independent state. However, there are currently no accurate biomarkers that clearly identify this transition. The aim of this study is to determine biochemical and hyperpolarized biomarkers of Androgen Independent Prostate Cancer (AIPC) in the TRansgenic Adenocarcinoma of Mouse Prostate (TRAMP) model. Differences in the lactate dehydrogenase (LDH) activity and Ki67 staining, prior to and post hormone therapy (surgical castration), were investigated in conjunction with hyperpolarized 13C metabolites in magnetic resonance spectroscopy (HP 13C-MRSI) studies of tumors in vivo.

Methods: MRI/13C MRSI studies after injection of HP [1-13C] pyruvate were performed on TRAMP mice. Twenty-six mice were sacrificed following their MRI/13C MRSI studies for biochemical and pathological analysis of their prostates/tumors. These TRAMP mice were categorized into three groups in order to determine hyperpolarized biomarkers of androgen dependent (response to castration) and androgen independent (continued tumor growth after castration) prostate cancer. The pre-treated group consisted of 8 TRAMP mice, not castrated, that were sacrificed after a baseline MRI/13C MRSI study; this group consisted of a mix of disease states. The treated groups were castrated following a baseline MRI/13C MRSI scan. Androgen responsiveness was assessed through morphometric analysis of tumors. Six TRAMP mice with less than 20% increase in tumor volume were identified as androgen dependent mice. Twelve TRAMP mice with greater than or equal to 20% increase in tumor volume were identified as AIPC. After final MRSI scan, mice were dissected and tumors analyzed histologically for grade and proliferative and apoptotic index. Immediately adjacent tumor tissue was assayed for LDH activity, using a well described NADH-linked spectrophotometric method. Spectroscopy was acquired with a dual-tuned mouse coil in a GE 3T scanner. The spectral data acquired was aligned with the traced tumor region on anatomic images. The peak area-to-noise ratio of HP lactate, pyruvate, alanine and total hyperpolarized carbon (THC = lactate+pyruvate+alanine) were calculated.

Results: Hyperpolarized (HP) biomarkers showed significantly lower lactate, lactate/pyruvate, and lactate/THC levels in androgen dependent versus AIPC. Specifically, the AIPC phenotype had a significantly higher HP lactate (116±60 vs 53±41, $p<0.02$), HP lactate/pyruvate (1.97±0.94 vs 0.94±0.58, $p<0.01$), and lactate/THC (0.57±0.09 vs 0.38±0.14, $p<0.002$). In addition, the biochemical markers showed a significantly lower LDH activity and Ki67 staining in androgen dependent versus AIPC. The AIPC phenotype had a significantly higher LDH activity (4.81±0.003 vs 2.01±0.0009 nM-NADH/min/ug-protein/ml, $p<0.02$) and Ki67 staining (82%±14.6 vs 33%±29.7, $p<0.0004$) relative to AIPC.

Conclusions: AIPC is defined as continued tumor progression in the face of castrate levels of androgen. In this study we show that in the TRAMP model, biochemical biomarkers of AIPC include significantly elevated LDH activity and Ki67 staining, while HP biomarkers include significantly elevated lactate, lactate/pyruvate, and lactate/THC. Therefore, these biochemical and HP biomarkers could be helpful in delineating disease status for improved therapeutic selection.

Project Title: Accuracy of DW-MRI for Detection of Prostate Cancer after Radiation Therapy

Bellina Chea, Christopher Sotto BS, Galen Reed BS, John Kurhanewicz PhD, Antonio C. Westphalen MD

Purpose: To determine if addition of diffusion-weighted MR imaging **improves the detection** of locally recurrent cancer after definitive external beam therapy when compared to T2-weighted MR imaging alone.

Materials and Methods:
This study was CHR approved and HIPAA compliant. We retrospectively identified 20 men who underwent 3T endorectal MRI after radiation therapy for suspected recurrent prostate cancer. At the time of diagnosis, patients had a mean PSA of 13.0 ng/ml, median Gleason score of 7, and median clinical stage of T2A. Thirteen patients had biochemical failure defined as nadir PSA +2ng/ml. All patients received the full course of radiation therapy (mean dose = 74 Gy). Fifteen patients also received androgen deprivation therapy. One radiologist (ACW) reviewed the T2-weighted images for the presence or absence of cancer within each sextant. On the same T2 images, two authors (BC, ACW) manually outlined each sextant of the prostate. These outlines were saved and used to automatically select the same regions on ADC maps and to determine the corresponding ADC values. The areas under the ROC curves were calculated for T2-weighted MRI alone and combined T2-weighted MRI and diffusion-weighted MRI using generalized estimation equations and biopsy results as standard of reference.

Results:
Recurrent cancer was identified by biopsy in six of twenty patients (30%). The area under the ROC curves of T2-weighted MRI alone was 62%, and for the combined approach, 82% (figure 1A and 1B). The optimal ADC value threshold was determined to be 1.47 mm^2/s. This threshold has a sensitivity and specificity of 83% and 80%, respectively. In other words, the test will miss cancer and falsely suggest the diagnosis in 5% and 14% of patients, respectively. The test will change the initial probability of cancer from 30% to a post-test probability of 8% if DW-MRI is negative (ADC value > 1.47 mm^2/s) or to 64% if DW-MRI is positive (ADC value ≤ 1.47 mm^2/s).

Conclusion: Diffusion-weighted MRI improves the accuracy of MR imaging for detection of recurrent disease after radiation therapy.

Figure 1: ROC curves for detection of locally recurrent prostate cancer after external beam radiation therapy (with or without hormonal therapy) with T2-weighted MRI (solid line) and combined T2-weighted MRI and DW-MRI (dotted line).

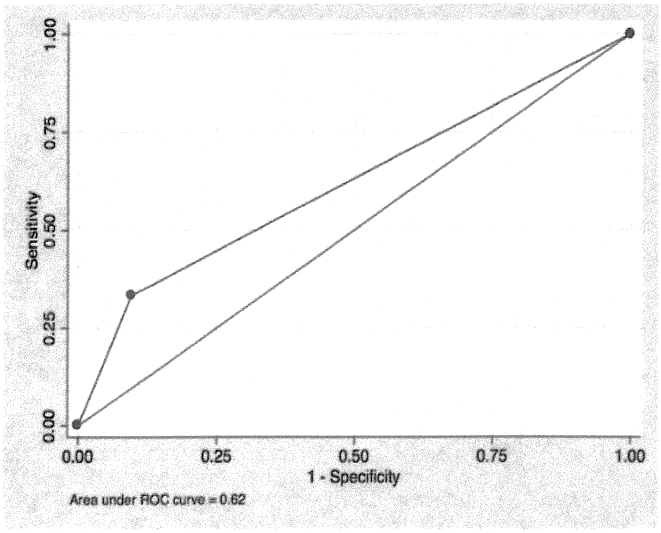

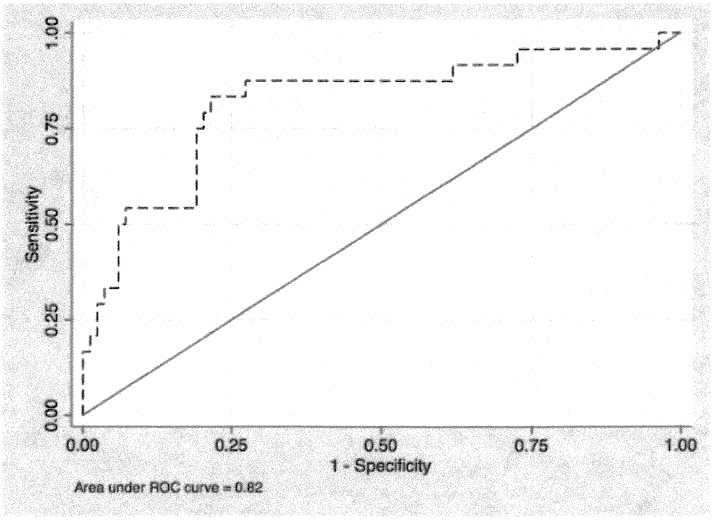

Magnetic resonance spectroscopy metabolic profiling reveals different mechanisms of action of PI3K and MAPK inhibitors in prostate cancer.

Alessia Lodi, Sabrina M. Ronen. University of California San Francisco, San Francisco, CA

The phosphatidylinositol-3-kinase (PI3K) and the mitogen-activated protein kinase (MAPK) pathways contribute to the regulation of several key cell functions including proliferation, differentiation, and oncogenic transformation. Deregulation of these pathways is observed in several human malignancies. Due to the involvement of these signaling pathways in oncogenesis and tumor growth, inhibitors of PI3K and MAPK pathways are under investigation as targeted anticancer treatments. Besides promoting perturbations of these signaling pathways, inhibitors of PI3K and MAPK have been recognized to affect cellular metabolism. Here, we used magnetic resonance spectroscopy (MRS) to investigate the changes induced on the metabolism of PC3 prostate cancer cells following treatment with LY294002, an inhibitor of the PI3K pathway, U0126 an inhibitor of the MAPK pathway and 17AAG which induces the simultaneous inhibition of MAPK and PI3K by targeting the heat-shock protein 90 (HSP90). Proton NMR spectroscopy data acquired on the PC3 intracellular extracts were analyzed using a fully untargeted metabolomics approach. The principal component analysis (PCA) of the full dataset was characterized by tight grouping within each treatment and complete separation between the control and each of the three treatments groups. In particular, the first principal component (PC1), recapitulating about 45% of the variability, separated the control and U0126-treated groups from the LY294002 and the 17AAG treatments. All the treatments also separate along PC2 (about 30% variability) but the control and U0126-treated sample groups remain quite close, indicating limited variation in the metabolic fingerprint following 48 hrs of treatment. The separation along PC1 is largely determined by the intracellular accumulation of higher levels of glucose and most of the amino acids, and the depletion of lactate following the LY294002 and 17AAG treatment. These findings point to the induction of autophagy in PC3 cells following treatment with LY294002 and 17AAG,confirmed by the increased LC3 protein levels, and we hypothesize that this is triggered by the inhibition of mTOR induced by both drug treatments. Moreover, the hindered glycolysis observed following treatment with LY294002 is due, as previously observed also in breast cancer cell lines, by the HIF1alpha-mediated lactate dehydrogenase (LDH) activity decrease. In contrast, although treatment with 17AAG also induced a moderate decrease in intracellular lactate levels in PC3 cells, the modulation of metabolites involved in the TCA cycle and in the amino sugars biosynthesis pathway suggest that 17AAG treatment triggers alternative pathways for glucose consumption in PC3 cells. These results indicate that treatment with both LY294002 and 17AAG, but not U0126, induce autophagic mechanisms likely entailed by their PI3K inhibitory effect and mTOR inhibition. However, additional metabolic effects induced on PC3 prostate cancer cells by these PI3K and/or MAPK inhibitors, in particular as it relates to glucose consumption, are vastly different and likely to affect the outcome of therapy.

Multiband-Excitation and Multi-Echo Pulse Sequence for Hyperpolarized ^{13}C Metabolic Imaging: Application to ^{13}C-Pyruvate and ^{13}C-Lactate Acquisition

P. J. Shin[1,2], S. Hu[2], C. von Morze[2], P. E. Z. Larson[2], and D. B. Vigneron[1,2]

[1]Joint Graduate Group in Bioengineering, University of California at San Francisco & Berkeley, San Francisco, CA, United States,
[2]Department of Radiology and Biomedical Imaging, University of California at San Francisco, San Francisco, CA, United States

Introduction Hyperpolarized ^{13}C technique has emerged as a new powerful tool for monitoring metabolic processes *in vivo*. In this method, ^{13}C labeled pyruvate is used as substrate and its conversion to lactate is measured to assess the metabolic state of the imaging subject. Conventional MRSI sequences used for data acquisition are limited by long TR and thus produce images with low spatial resolution. In this project, we develop a new pulse sequence with much shorter TR for simultaneous acquisition of pyruvate and lactate signal. The sequence is composed of multiband RF excitation with multi-echo readout gradient. A reconstruction method to separate out two metabolic images from acquired data will also be developed. With this technique, we will be able to obtain pyruvate and lactate images with higher spatial resolution and greater SNR.

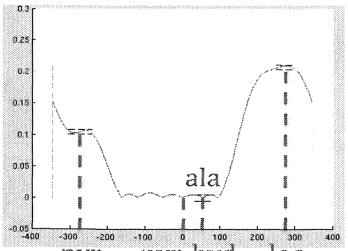

Figure 1. Desired spectral profile

Methods **1)** Multiband excitation RF pulse was designed using MATLAB (MathWorks). Spectral profile (figure 1) was specified so that only pyruvate and lactate are excited within the spectral bandwidth with different flip angles. Other metabolites such as alanin and pyruvate-hydrate are completely suppressed. **2)** Optimal multi-echo readout gradient was designed to have 2.5mm in-plane spatial resolution with data matrix size of 64x64. **3)** Image reconstruction method based on least-squares estimation was implemented to separate out pyruvate, lactate and field-map image from the acquired data.

Results **1)** RF pulse and its simulated profile at field strength of 3T is given in figure 2. Pulse length is 16.8ms with max B1 value of 0.052G. **2)** Minimum time three echo readout gradient that satisfies the desired imaging specification is shown in figure 3. TR of the sequence is approximately 25ms. **3)** Image reconstruction algorithm was implemented in MATLAB and was tested on a single voxel FID data. The same algorithm will be used to produce pyruvate and lactate image once we acquire necessary data.

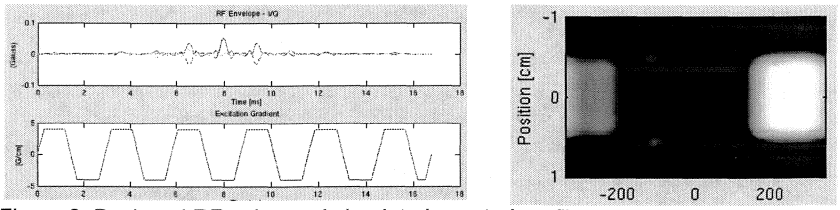

Figure 2. Designed RF pulse and simulated spectral profile

Discussion The new pulse sequence has 10 times shorter TR than the sequence currently used. This advantage makes it possible to collect more data within the time frame limited by the T_1 decay of hyperpolarized signal. Additional improvements are expected from implementing compressed-sensing into the sequence.

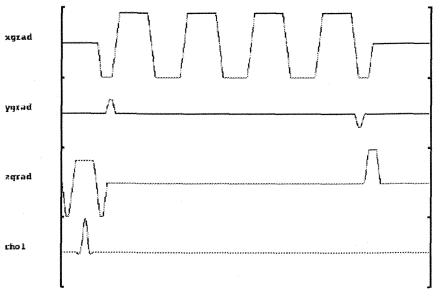

Figure 3. Multi-echo readout

References
[1] P. E. Z. Larson et al., JMR 2008, 194, 121-127
[2] S. B. Reader et al., MRM 2005, 54, 636-644
[3] S. Hu et al., MRM 2010, 63, 312-321

Acknowledgements Funding from NIH EB007588.

SIVIC: An Extensible Open-Source DICOM MR Spectroscopy Software Framework and Application Suite

Authors: Marram P. Olson *UCSF Radiology and Biomedical Imaging;* Jason C. Crane *UCSF Radiology and Biomedical Imaging;* Sarah. J. Nelson *UCSF Radiology and Biomedical Imaging, Department of Bioengineering and Therapeutic Sciences*

Synopsis: SIVIC (Spectroscopic Imaging, VIsualization and Computing), an open-source, cross-platform, DICOM MR spectroscopy software framework is presented. SIVIC provides an extensible platform for reading, processing, and visualizing MRS data from various non-DICOM sources, simplifying MRS workflows in multi-center environments. SIVIC's extensible open-source algorithm interface supports sharing and evaluation of new MRS methodologies. SIVIC enables clinicians and researchers to leverage PACS or other standard DICOM tools for storage, communication and discovery of spectroscopic data.

Introduction: Despite the existence of the DICOM MR Spectroscopy standard [1], it is currently not widely adopted and there is a lot of variability in the way MR spectroscopy data sets are encoded. This results in a lack of interoperability between imaging devices, PACS and MRS processing and visualization software packages. This is particularly problematic for multi-center collaborations, which often require complicated workflows and file format conversions to analyze spectroscopic data from multiple vendors. SIVIC [https://sivic.sourceforge.net] is designed to streamline the integration of MRS data with MRI studies. It provides tools for reading DICOM and non-DICOM MRS data, an extensible algorithm layer to support development of reconstruction, post-processing and quantification methodologies, and display tools for visualizing MRS data.

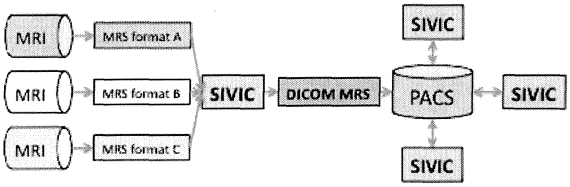

Figure 1. SIVIC converts MRS data acquired in a heterogeneous multi-center environment to the DICOM MRS standard for transmission with other imaging data to PACS. PACS clients that support SIVIC, e.g. OsiriX, can retrieve DICOM MRS data for analysis and visualization with other DICOM data using a single software package.

Discussion: The SIVIC MRS software framework and applications are designed to streamline MRS workflows, by supporting conversion of non-DICOM MRS data to the DICOM MRS standard. Once MRS data is encoded to the DICOM standard, it can be integrated with other DICOM imaging data and DICOM infrastructures (PACS) can be utilized for communicating, discovering and storing data (Fig 1). Figure 2 shows the visualization interface from the standalone SIVIC application. Display of acquisition grid, sat bands, volume localization and overlays are supported in 2D and 3D modes. Processing tabs (not shown) provide interactive access and graphical feedback for application of reconstruction, post-processing and quantification pipelines. SIVIC's implementation of the DICOM MRS standard together with the standalone SIVIC display applications enable the free flow and interoperability of MRS data DICOM applications with a common tool set, permitting scientists to focus on the underlying MRS science rather than the logistics of handling MRS data.

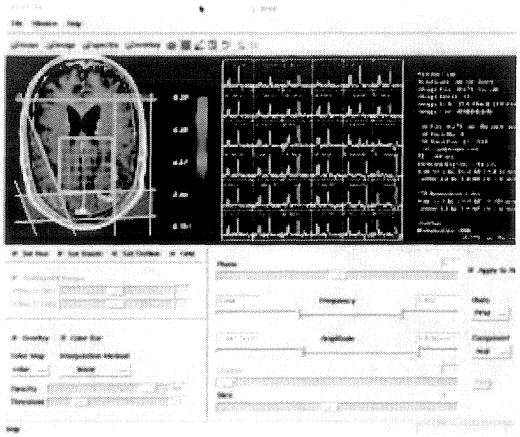

Figure 2. The SIVIC standalone application showing the visualization panel that supports the rendering of the acquisition grid, sat bands, volume selection, and color metabolite overlays, for multi-coil and time point data, all referenced spatially to anatomical data. Interactive data reconstruction, processing and quantification is supported through the processing panel (not shown).

References:

1. ftp://medical.nema.org/medical/dicom/2008/08_03pu.pdf

Effect of the Monocarboxylate Transporter Inhibitor α-cyano-4-hydroxy-cinnamate on *In Vivo* Hyperpolarized ^{13}C Spectroscopic Imaging

Simon Hu[1], Robert Bok[1], Asha Balakrishnan[2], Andrei Goga[2], John Kurhanewicz[1], Daniel B. Vigneron[1]

[1] Department of Radiology and Biomedical Imaging, University of California, San Francisco, CA
[2] Department of Medicine, Division of Hematology/Oncology, University of California, San Francisco, CA

Introduction: Development of hyperpolarized technology utilizing dynamic nuclear polarization has enabled the measurement of ^{13}C metabolism *in vivo* at very high SNR [1]. Thus far, the most researched agent for *in vivo* applications has been [1-^{13}C]pyruvate. In this work, the role of cell membrane transport on the conversion of [1-^{13}C]pyruvate to [1-^{13}C]lactate and to [1-^{13}C]alanine *in vivo* was investigated by utilizing the monocarboxylate transporter (MCT) inhibitor α-cyano-4-hydroxy-cinnamate [2]. Reduced hyperpolarized lactate ($P = 0.055$), alanine ($P = 0.032$), and total carbon ($P = 0.023$) were detected after α-cyano-4-hydroxy-cinnamate administration, which is in agreement with recent *in vitro* work where decreased hyperpolarized lactate was detected after breast cancer cells were given an MCT inhibitor [3].

Methods: All studies were performed on a GE 3T scanner with a custom $^{1}H/^{13}C$ mouse coil. ^{13}C 3D-MRSI data (TE/TR = 140ms/215ms, 0.034 cm^3 voxel size, 16 second acquisition time) were acquired with a double spin-echo compressed sensing pulse sequence [4] after injection of 0.35 mL of 80mM hyperpolarized $^{13}C_1$-pyruvate. Metabolite areas were derived from the spectral arrays over regions of interest identified from the co-registered anatomical images. For each animal studied, a baseline hyperpolarized acquisition was first acquired. Then the acquisition was repeated 30 minutes after an intraperitoneal injection of 90 mg/kg of 4-CIN (Sigma Aldrich) dissolved in a pH 7.5 phosphate buffer. Liver cancer mice (Tet-o-MYC/LAP-tTA double-transgenic mice in which the human MYC proto-oncogene is selectively overexpressed in the liver [5]) were used.

Results and Discussion: Figure 1 shows a comparison of hyperpolarized spectra from liver tumor regions from two separate mice before and after 4-CIN administration. The representative voxels in Figure 1 show lowered lactate and alanine. Figure 2 shows data from all mice studied ($n = 6$). The percentage change values in Figure 2 were computed over all liver tumor voxels. These results show that MCT inhibition had a significant impact on conversion of [1-^{13}C]pyruvate *in vivo*, which is in agreement with previous studies performed *in vitro* [3]. As shown by the data, lactate and alanine dropped after 4-CIN administration, suggesting that hyperpolarized conversion occurs intracellularly, i.e. after uptake of pyruvate. In conclusion, these initial data show that this MCT inhibitor approach can be used to investigate the role of cell membrane transport of pyruvate on the resulting hyperpolarized spectra *in vivo*.

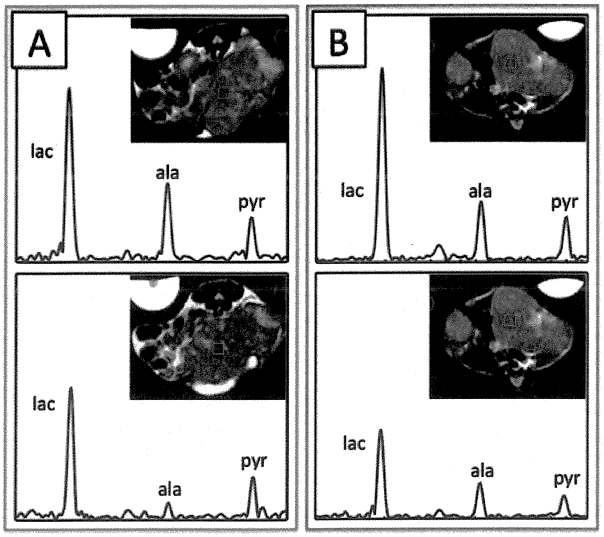

Figure 1: A) Representative spectrum (voxel highlighted by box on anatomical image) in which hyperpolarized lactate and alanine decreased 30 minutes after administration of 4-CIN. In this example, alanine decreased dramatically. B) Spectrum from a different tumor in which, once again, hyperpolarized lactate and alanine decreased post 4-CIN. This time, lactate decreased more than alanine.

References: [1] Ardenkjaer-Larsen et al. PNAS (2003) 100:10158 [2] Schurr et al. Brain Research (2001) 895:268. [3] Harris et al. PNAS (2009) 106:18131. [4] Hu et al. 3D Compressed Sensing for Highly Accelerated Hyperpolarized ^{13}C MRSI with *In Vivo* Applications to Transgenic Mouse Models of Cancer. MRM (2010) 63:312 [5] Shachaf et al. Nature (2004) 431:1112.

Acknowledgments: Funding from NIH EB007588 & CA137298.

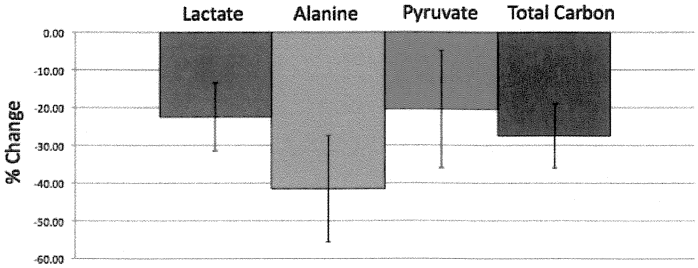

Figure 2: Summary of hyperpolarized lactate, alanine, pyruvate, and total carbon changes in tumor tissue over all animals studied ($n = 6$) with standard error bars shown. There was a net decrease, on average, for all the hyperpolarized metabolites.

Single shot chemical shift specific imaging methods for hyperpolarized 13C studies at 14T

Subramaniam Sukumar, Kayvan R. Keshari, Peder E.Z. Larson, Robert Bok, Daniel B. Vigneron and John Kurhanewicz
University of California, Department of Radiology and Biomedical Imaging, Surbeck Laboratory for Advanced Imaging, San Francisco, CA.

Magnetic resonance spectroscopic imaging (MRSI) methods using, hyperpolarized, ^{13}C labeled biomarkers can provide novel in vivo metabolic information for biomedical research. During hyperpolarized ^{13}C experiments, the magnetization is irreversibly lost due to RF saturation, metabolism and T1 relaxation. Therefore, the general approach when designing pulse sequences for such studies is to sample the magnetization quickly and to utilize the available magnetization very efficiently. At 14T hyperpolarized studies, the large chemical shift dispersion imposes further challenges - 1) The RF pulses must be capable of covering a large bandwidth, 2) Chemical shift artifacts and errors in the slice and readout gradients are linearly increased as compared to lower fields, and 3) Sequences using EPSI readout schemes require large gradients to be switched rapidly to satisfy the minimum spectral width and resolution requirements. In this project, we have developed and applied specialized pulse sequences incorporating frequency specific excitation methods to overcome the problems related to wide chemical shift spread at high fields. Also, in order to utilize the magnetization efficiently, we have applied single shot, EPI and spiral readout acquisition schemes. The single shot methods, with acquisition times on the order of 50-200msec, can provide high temporal resolution for time course studies. Phantom experiments were done to demonstrate the feasibility of the experiments at 14T. In addition, we have successfully applied a novel 3D imaging method for observing ^{13}C labelled biomarkers in a TRAMP mouse with prostate tumor as shown in Figure 1. The pulse sequence, $\{ 90_f - [180_f - (\quad EPI_{Nx} \quad)_{Ny}] \}_f$, is based on GRASE imaging, where f refers to frequency selection and N the two phase encode dimensions. The frequency specific RF pulses overcome the limitations related to wide spectral dispersion at high field strengths (14T). The inter-dispersed 180deg pulses help to minimize T2* related signal losses and artifacts. Because of the short acquisition time (153msec), the sequence is both frequency and time specific so each component can be detected at a specific time during an experiment. Figure 1 shows Carbon-13 images obtained at 44s after a mixture of hyperpolarized [1-^{13}C]-Pyruvate and -Urea was injected into a TRAMP mouse. Lactate is mainly generated as a result of metabolism of Pyruvate in the tumor and Urea is used to monitor perfusion in tissue.

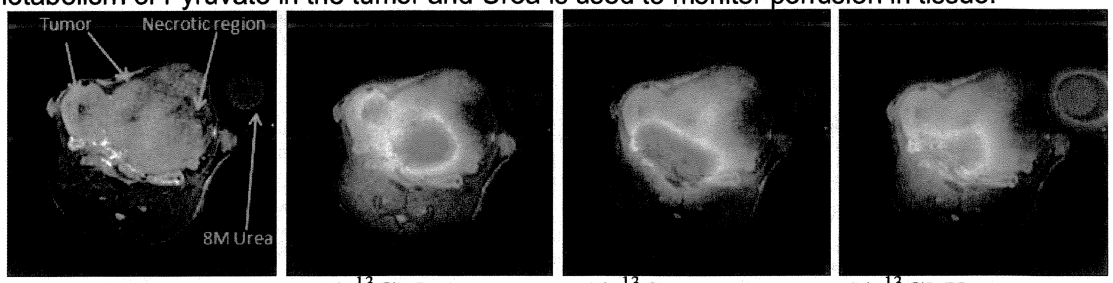

SE image **[1-^{13}C]-Lactate** **[1-^{13}C]-Pyruvate** **[1-^{13}C]-Urea**

Figure 1: Axial spinecho image of a TRAMP mouse with a large prostate tumor is shown on the left. ^{13}C images were obtained using a frequency specific 3D GRASE imaging method and selected slices (in color) are shown superimposed on the anatomical image. Data collection was started 44s after injection of a mixture of [1-^{13}C]-Pyruvate and –Urea. Each component was imaged in 153msec with a resolution of 2.5x3.3x3.3mm^3 (interpolated to 1.25mm^3, 0.002cc).